Research on a Novel Aqueous Semi-Solid Redox Flow Battery Based on Iron and Manganese Semi-Solid Electrode Suspensions

J. W. Vink

To obtain the degree of Master of Science Sustainable Energy Technology

at Delft University of Technology,

to be defended publicly on Friday December 18, 2020.

Student number:	4174801
Thesis committee:	Dr. E. M. Kelder Prof. Dr. F. M. Mulder Dr. Ir. M. Rohde

Preface

Over the last 8 years of studying at the Technical University of Delft I have grown into a person capable of understanding what is at the very core of myself and how this is closely intertwined with a sustainable future, my friends and a loving family. By graduating my Master's Degree this chapter comes to an end and a new, exciting one begins. It was a journey with many side roads, ranging from a variety of academic fields such as civil, mechanical and electrochemical engineering, to a variety of working environments, doing cold sales on the streets to the ongoing development of large-scale solar and battery projects, to wandering the world in many places in Europe, Asia, Australia and Africa. Sometimes alone, but always with family and friends close to me. I look back on this chapter of my life with pride, love and most of all – gratitude.

Gratitude to my family, my girlfriend and my friends for always being there unconditionally, for the many great moments and for much laughter. I want to especially thank my parents, as without them this amazing time I had would not have been possible. I want to thank my dad for always standing ready and for the many helpful conversations we had (ranging from this thesis to the washing machine that broke again) and my mom for the hundreds of times that we just called about nothing in particular (Boris), always welcoming and always with a smile.

With respect to this thesis I would like to thank in particular Erik Kelder and Frans Ooms for helping making it possible. With corona measures in full force while being relatively unexperienced in electrochemistry, this practical thesis was extra challenging. However, Erik always knew how to bring my focus back on track and has the gift of making things sound easy when actually they are very complicated. Frans helped incredibly with the practical arrangements and guidance in the lab and did this with an ever-lasting smile.

Finally, I would like to thank the members of the thesis committee for reviewing this work and their critical engagement.

Hans Vink
December 7, 2020
Delft

Abstract

In the search for new large-scale battery technologies that are cheap, safe and durable, in this research it is found that the state of the art semi-solid redox flow battery ("SSRFB") technology shows perspective. Therefore, a novel, cheap and safe aqueous SSRFB design is introduced based on iron- and manganese hydroxide materials. This design was subsequently tested in the lab through which it was concluded that it is not possible to effectively make a SSRFB based on FeOOH and $Mn(OH)_2$ semi-solid electrode ("SSE") suspensions. Systematic proof is provided on how this can be attributed to the specific combination of the active materials in the highly alkaline environment, but that in itself, both the tested SSRFB configuration and SSE suspensions are functional. On the one hand, a complex chemical system of the active species consisting of multiple thermodynamic equilibria had the consequence that the open circuit voltage ("OCV") had a very low value of 0.2 V instead of the expected 0.63 V. On the other hand, it was shown that both the FeOOH and the $Mn(OH)_2$ SSE suspension could be separately cycled versus respectively a solid zinc and copper electrode and that a cheap microfiltration membrane suffices in the design of a SSRFB (on the condition that ionic active species are not apparent in the system). In sum, this research demonstrates that the SSRFB by its very nature is a suitable battery technology in which cheap and safe materials can be used for large-scale energy storage. However, that the combination and optimization of the right active materials in the right environment proves to be fundamental for proper operation and is in fact a complex balance between electric and ionic conductivity, colloidal stability, viscosity and (electro)chemical stability.

Table of Contents

List of Figures

List of Tables

Acronyms

DoD	Depth of discharge
SoC	State of charge
LCOS	Levelized cost of storage
RFB	Redox flow battery
SSRFB	Semi-solid redox flow battery
SSE	Semi-solid electrode
EIS	Electrochemical impedance spectroscopy
Autolab	MetrOhm Autolab PGSTAT30
OCV	Open circuit voltage
Eq.	Equation
MW	Molar weight
TSO	Transmission system operator
DSO	Distribution system operator
VRFB	Vanadium redox flow battery
ICRFB	Iron chromium redox flow battery
PHRFB	Polysulphide-halide redox flow battery
Li-ion	Lithium Ion
LFP	$LiFePO_4$
LTO	$LiTiO_{12}$
CB	Carbon black
KB	Ketjenblack EC 600-JD
KOH	Potassium hydroxide
NaOH	Sodium hydroxide
$Fe(OH)_3$	Iron(III)hydroxide
$Fe(OH)_2$	Iron(II)hydroxide
FeOOH	Iron(III)oxyhydroxide
$Mn(OH)_3$	Manganese(III)hydroxide
$Mn(OH)_2$	Manganese(II)hydroxide
PAA	Poly acrylic acid MW_v 450.000
ALG	Alginic acid 500
PVP	Polyvinylpyrrolidone
wt%	Weight percentage
rpm	rotations per minute

List of Symbols

σ_e	Electronic conductivity	[S m^{-1}]
σ_i	Ionic conductivity	[S m^{-1}]
C_{dl}	Double layer capacitance	[F]
R_{ion}	Electric resistance of ions	[Ω]
R_{kb}	Electric resistance of carbon black	[Ω]
$R_{0\text{-}low}$	Electric resistance at low frequency intersect of real Z axis	[Ω]
$R_{0\text{-}high}$	Electric resistance at high frequency intersect of real Z axis	[Ω]
Z	Impedance	[Ω]
Φ	Phase shift	[°]
V_{rms}	Average electrical potential	[V]
U	Electric potential	[V]
I	Electric current	[A]
d_{el}	Distance between electrodes	[m]
A_{el}	Area of electrode	[m^{2}]
T	Temperature	[-]
a_x	Activity of component x	[mol L^{-1}]
Q_r	Reaction Quotient	[-]
E_{cell}	Electrochemical cell potential	[V]
E^0_{cell}	Electrochemical cell potential at standard conditions	[V]
E^0_{cat}	Cathodic cell potential at standard conditions	[V]
E^0_{an}	Anodic cell potential at standard conditions	[V]
K	Debye-Hückel parameter	[-]
ε_r	Relative permittivity	[F m^{-1}]
e	Elementary electric charge	[C]
n^{∞}	Ionic bulk concentration	[mol L^{-1}]
z	Valency of ion	[-]
α	Shape factor	[-]
E	Electric field strength	[V m^{-1}]
μ	Mobility	[m V^{-1} s^{-1}]
v	Velocity	[m s^{-1}]
ζ	Zeta potential	[V]
η	Viscosity	[N s m^{-2}]
ρ	Density	[kg m^{-1}]
a	Diameter of solid particle	[m]
v_{sed}	Rate of sedimentation	[m s^{-1}]
Q	Charge	[C]
N	Amount of mol	[mol]
F	Faradays constant	[C mol^{-1}]
n	Number of electrons transferred per mol of product	[n]
K	Equilibrium constant	[-]

R	Gas constant	8.314	[J K^{-1} mol^{-1}]
K_b	Boltzmanns constant:	1.381×10^{-23}	[m^{2}kgs^{-2}K^{-1}]
F	Faradays constant	9.65×10^{4}	[C mol^{-1}]
ε_0	Permittivity of a vacuum	8.854×10^{-12}	[F m^{-1}]
g	Gravitational acceleration	9.81	[m s^{-2}]

1. Introduction

The increasing penetration of uncontrollable solar and wind energy production in the global energy mix results in a fundamental problem: The energy grid of many countries is not prepared for the transition from central, controllable electricity generation to decentralised, uncontrollable electricity generation. This problem makes the integration of additional solar and wind energy assets into the grid increasingly difficult due to grid congestion (Figure 1). For the Netherlands alone, the consequential costs for grid reinforcements of the TSO are predicted to be €16 billion for the period 2020-2029 (Tennet, 2020). The additional delays caused by these reinforcements seriously challenge the ability of the Netherlands to achieve the goals of The Paris Agreement. This global problem, exemplified here by the Netherlands, points to the great need for large-scale energy storage that can offer flexibility to the energy grid. Energy storage in batteries offers a part of the solution, but important steps are yet to be made in developing battery systems that are safe, economical and durable.

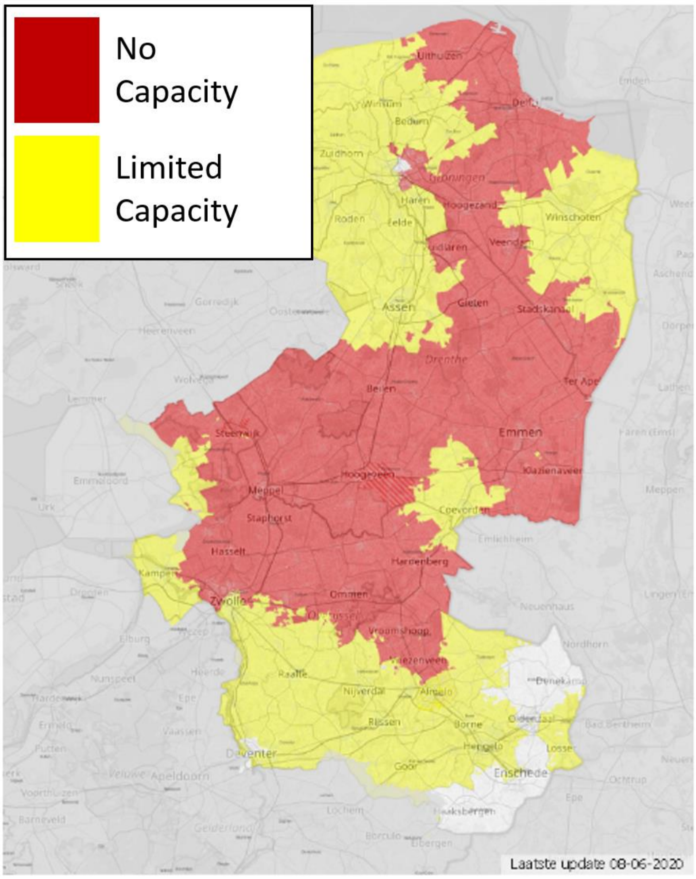

Figure 1: Enexis (DSO) transport capacity for feeding in energy into the grid for the North-Eastern part of the Netherlands (Enexis Netbeheer, 2020).

1.1. Background and Motivation

The battery industry is looking for large-scale energy storage technologies that show better potential than the current established technologies, such as Li-ion batteries. Criteria for the key characteristics of an idealised large-scale stationary battery are that it has to be safe, economical and durable. Although the majority of research still goes into the development of

Li-ion battery technology (and by the year 2025 Li-ion battery technology is still expected to be the most cost-effective battery storage technology (Mongird et al., 2019)), it does not seem like the preferable choice for globally applied large-scale stationary energy storage. The widely applied Li-ion battery may have superior traits when considering mobile applications and energy efficiency, but they lack safety, often use rare and expensive materials (lithium is only the 33rd most abundant element in the earth's upper crust (Yaroshevsky, 2006)) and their energy capacity degrades substantially when operating at deep cycles, resulting in relatively short cycle lifetimes. Recent studies have shown that commercial Li-ion batteries have a modest cycle lifetime of around 5000 cycles when operating at room temperature and cycling at a low DoD of 50% (Xu, Oudalov, Ulbig, Andersson, & Kirschen, 2018). Regarding safety of Li-ion technology, 206 cases of Li-ion related fires/explosions from March 1991 to January 2018 have been reported by the United States Federal Aviation Administration alone (Kong, Li, Jiang, & Pecht, 2018).

Redox flow batteries ("RFB") in contrary, have shown intrinsic characteristics that exhibit great potential for large-scale battery storage. For example, the recently commercialised all-vanadium RFB shows low toxicity to humans and low fire hazard risk because of the aqueous vanadium electrolyte. It also has an exceptionally high cycle lifetime, with up to 270.000 full cycles on stack components claimed by manufacturers (Chen et al., 2017). These intrinsic traits result in significantly lower LCOS compared to Li-ion batteries, whilst also being safer. Although large-scale all-VRFBs are slowly and increasingly being developed due to these attractive characteristics, the cost of the ion-exchanging membranes and pumps and scarcity of the vanadium electrolyte make development a highly capital intensive exercise (Zeng et al., 2015). This constitutes a significant barrier for this technology to commercially penetrate the energy storage market. These factors suggest that research into new, safe, durable and, importantly, cheaper RFB configurations can contribute to enabling more cost-effective large-scale battery storage than is currently the case.

As a result of the preliminary literature study on state of the art RFB technologies (Chapter 2.1), it was found that an aqueous SSRFB based on the cheap and insoluble $Fe(OH)_2$, $Fe(OH)_3$, $Mn(OH)_2$ and $Mn(OH)_3$ electroactive materials shows potential regarding safety, costs and durability. At first sight, this combination of electroactive material can offer a cell potential of 0.71 V (Lide, 2010), well outside the range of electrolysis of water. Iron is the fourth most abundant element in the earth's upper continental crust and manganese is the twelfth most abundant (Yaroshevsky, 2006). Moreover, these materials pose no threat to humans or the environment and the aqueous electrolyte offers low fire hazard risks. When translated into an idealised system without losses and full utilization of the active material, this could provide energy storage < €6 per kWh (based on active material only) (Appendix A). The proposed insolubility of the hydroxide complexes enables the use of cheap microfiltration membranes, since cross-over contamination can be easily prevented (which is often the reason for degradation of all-liquid RFBs) (Chapters 2.1.1 and 2.1.2). Such membranes cost less than €2 per m^2, more than 100 times cheaper than ion-exchanging membranes (Zheng Li et al., 2013). Note that this shows significant perspective as the active material and ion exchanging membranes make up more than 70% of the costs for an 8 hour all-vanadium RFB (Zeng et al., 2015). The potential for long cycle lifetimes is further reinforced by the absence of dendrite formation in SSRFBs, as this has never been marked as a problem in literature. Lastly, the insoluble character of active species enables the potential for higher energy densities as one is not limited by the solubility of the active species, as is often the case in the all-liquid, single flow and liquid-gas RFB technologies (Chapter 2.1).

1.2. Objective

In the previous section, the background and motivation for this research has been substantiated. It shows that the preliminary aim of the research is to explore and find a new RFB configuration that meets the above mentioned three fundamental requirements for large-scale energy storage – it has to be safe, durable and economical. First, the safety of the applied electrolyte has to be such, that society can accept having large quantities of it in the vicinity of residential and industrial areas. Second, the battery must be durable and have high cycle lifetime potential, positively affecting the LCOS. Finally, the materials and configuration used in the battery must result in intrinsically low system costs.

It was found that a SSRFB based on the cheap and insoluble $Fe(OH)_2$, $Fe(OH)_3$, $Mn(OH)_2$ and $Mn(OH)_3$ in combination with cheap microporous membranes abides to these conditions at first sight, following from the preliminary literature study in Chapter 2.1. Very little practical research has been executed on SSRFBs (generally based on Li-based materials (Appendix B)). Nonetheless, the existing literature research makes it clear that proper development of SSE suspensions holds the key to an effective SSRFB system (J. Cheng et al., 2007; Zheng Li et al., 2013). Moreover, never before has the combination of iron hydroxides versus manganese hydroxides been demonstrated as SSE suspensions in an aqueous SSRFB setup. Providing the proof that the proposed combination of SSE suspensions work as a battery, allows for a framework for future research. The main objective of this thesis is thus to provide proof through practical experiments on whether a SSRFB can be created using iron hydroxide versus manganese hydroxide in aqueous SSE suspensions. This main objective is additionally supported through the sub-research questions below.

Main research question:

- Can a SSRFB be created using iron hydroxide versus manganese hydroxide using aqueous SSE suspensions?

Sub-research questions:

- Can both of the proposed SSE suspensions be separately charged and discharged, versus a known solid electrode?
- What is the influence of SSE composition on its electronic conductivity?
- What is the influence of SSE composition on their ionic conductivity?
- How are colloidally stable SSE suspensions created?
- How does the choice of type of membrane affect the system performance?
- What is the effectivity of the chosen active materials?

1.3. Methodology

The methodology of this research can be best summarised through two phases: the research initiation phase and the experimental phase.

Research Initiation Phase

Based on the problem description, initial background and motivation, a preliminary literature study was executed with the aim of identifying which state of the art RFB technique has most cohesion with the three suggested fundamental requirements for large-scale energy storage. This results in a novel design choice that has been never shown before – the iron-manganese SSRFB. It is additionally established that a good design of the SSE suspensions is the most critical component of a SSRFB. The combination of these two were subsequentially translated into the description of the main research question and the sub-research questions. The initiation phase of the research was finalised through a second literature study, that provides the background and theory required for effectively doing the experiments through which the main and sub-research questions can be answered.

Experimental Phase

The data used for answering the main and sub-research questions was obtained by executing practical experiments in the lab. During the start of the experimental phase, the chemicals and the cell equipment were acquired, the methodologies for the preparation of suspensions and synthesises were decided upon, the measurement and preparation equipment were obtained and four different experimental setups were made, all of which are further elaborated in Chapter 3. The experiments had the main focus on breaking down the system into the core components and finding trends that led towards suitable SSE suspensions. These SSE suspensions were subsequently used for experiments with respect to the main research question. Quantitative measurements were executed for conductivity and cycling procedures of SSE suspensions, as well as for membrane testing. This data was primarily obtained by use of the Autolab and execution of chrono-galvanostatic, chrono-potentiostatic, OCV and electrochemical impedance spectroscopy ("EIS") measurements. Analysis of the data was subsequentially done using Nova software and MATLAB. The data with respect to colloidal stability and viscosity was primarily obtained qualitatively. The visual influence of varying the composition of SSE suspensions was enough to determine the trends towards suitable SSE suspensions for static testing.

1.4. Readers Guide

The structure of this MSc thesis is as follows. In Chapter 2, a two-part literature study is presented. A preliminary part in which the background on state of the art RFB technologies is explained and a rationale is provided for the main research question of this MSc thesis. The second part of the literature study provides the specific theoretical background required for answering the main and sub-research questions as preparation for the experimental work. Followed by this comprehensive literature study, Chapter 3 provides the experimental methods and details. It shows which chemicals, cell equipment, preparational equipment and measurement tools were used. Next to this, it shows the methodology and procedures that were followed for realising the experimental setups. After this, Chapter 4 presents both the qualitative as well as the quantitative results of the respective experiments from Chapter 3. Moreover, it discusses how this relates to the main and sub-research questions and the performed literature study. This serves as a setup for Chapter 5, in which the research is concluded and recommendations are provided regarding future research.

2. Literature Study

In this chapter a two-part literature study is presented. First, the preliminary part in which is elaborated on state of the art RFB technologies. This provides the background that is required for understanding why the SSRFB was chosen as theme in the remainder of this thesis, as well as the justification for the specific system choice. The second part of the literature study provides the specific theoretical background required for answering the main and sub-research questions, as it relates the research question to the electrochemistry, ionic conductivity, electronic conductivity, colloidal stability and (electro)chemical stability of the system.

2.1. Redox Flow Batteries

This preliminary literature study aims to provide a background on the state of the art type of RFB techniques with respect to safety, costs and durability. This will function as a backbone through which a substantiated choice is made for a novel type configuration: the iron-manganese SSRFB. Zooming in on this choice provides the basis for the research question of this MSc Thesis.

RFBs can be subdivided in all-liquid, semi-solid, single flow and liquid-gas RFBs (Figure 2). In the remainder of this chapter a global outline of the different type of RFBs is presented, followed by some in depth examples, expanding on the safety of various redox flow batteries and electrolyte compositions, as well as the reliability and the economic aspects of different type of configurations. In the final section the novel iron-manganese SSRFB is presented and justified.

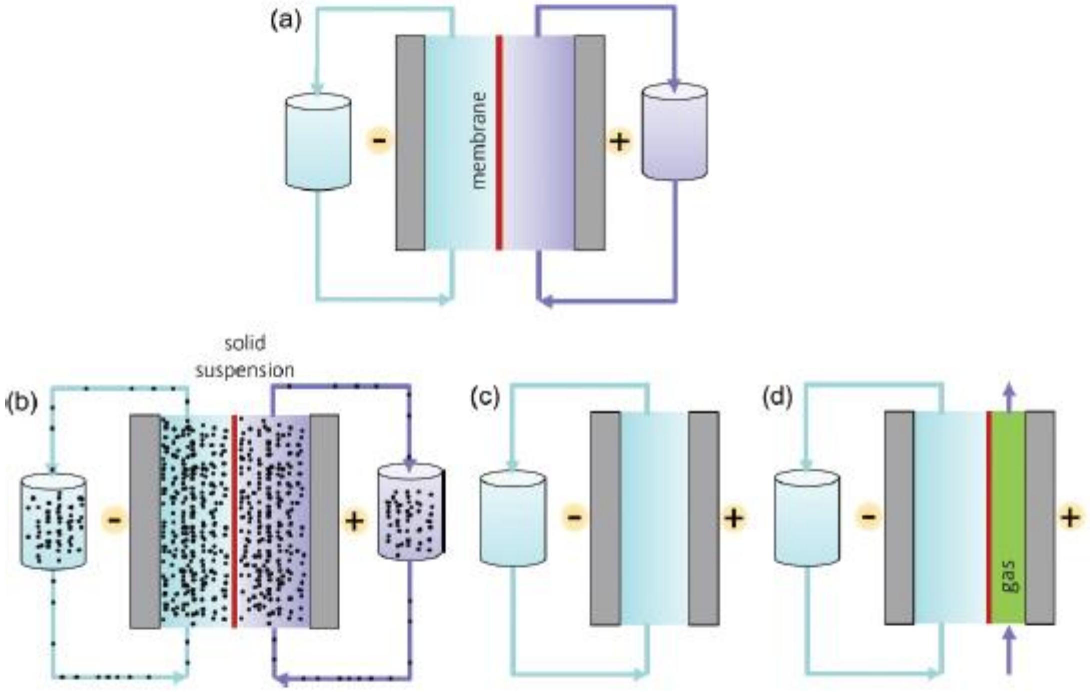

Figure 2: The high-level configuration of (a) an all-liquid RFB, (b) a SSRFB, (c) a single flow RFB (also known as membranelles RFB) and (d) a liquid-gas RFB (Chen et al., 2017).

2.1.1. All-Liquid RFBs

In all-liquid RFBs the electroactive species are dissolved in the electrolyte, resulting in an anolyte and a catholyte. The anolyte and catholyte are stored in separate reservoirs. When charging or discharging, the electrolytes are pumped through a cell stack. Within this stack the electrochemical reactions take place at inert electrodes (simultaneously functioning as current collectors). This happens through electrochemical interaction between the anolyte and catholyte, which are being separated by a ion-exchanging membrane. This system supports independent scaling of power and capacity. Power is scaled through the configuration of the stacks and capacity is scaled through the configuration of the electrolytes (volumes, molarity and type of electroactive species). This system is limited by the solubility of the electroactive species in the electrolyte, resulting in a low ion concentrations (typically 1-2M) and thus a low energy density between 10-40 Wh/L for the liquid electrolytes alone. The remainder of this chapter first explains the established all-liquid iron chromium and all-vanadium RFBs, and follows up with the more recently demonstrated polysulphide-halide all-liquid aqueous RFB.

All-liquid Iron Chromium RFB ("ICRFB")

The ICRFB was the first ever system that was named an all-liquid RFB system and was developed by NASA in de 1970s. The use of iron and chromium as active redox couples show potential due to the abundance of iron and chromium, having an estimated cost of $17/kWh (Zeng et al., 2016). The Fe^{2+}/Fe^{3+} couple is used as the cathode and the Cr^{2+}/Cr^{3+} couple is used as the anode. Furthermore, they make use of aqueous hydrochloric acid as solvent, ion exchange membranes as separators and carbon felt electrodes (Weber et al., 2011). Although the Fe^{2+}/Fe^{3+} redox couple shows fast reaction kinetics, catalysts such as Bi or Au-Ti are placed on the electrode surfaces at the negative side to both speed up the reaction kinetics of the Cr^{2+}/Cr^{3+} redox couple and simultaneously minimise hydrogen evolution at this electrode (Zeng et al., 2015).

The electrolyte is an aqueous solution of hydrochloric acid. When considering safety, the safety datasheet of hydrochloric acid shows that direct contact can result in serious health hazards and must be prevented. Furthermore it shows that this substance has mild corrosiveness behaviour, that can potentially lead to degradation of the battery. Nonetheless, an important upside is that due to the aqueous origin fire hazards are reduced to a minimum. The traditional ICRFB system has system costs reported to be as low as $194 / kWh for a 1MW - 8 hour system, whereas a recent study has shown it is possible to achieve levels as low as $138 / kWh for a 1MW – 8 hour system (Zeng et al., 2015). This is achieved by using a flow field-cell structure instead of a flow-through cell structure with porous carbon felt electrodes as shown in Figure 3. The traditional flow-through cell structures with porous electrodes are straightforward and easy to produce, but have the intrinsic downside that it increases pumping losses due to mass transport of the electrolyte through the tight pores. Although it is shown that a decrease in electrode sizing decreases the ohmic resistivity, it also significantly increases flow resistance. This latter effect is so drastic that traditional graphite felt electrodes have been designed to be relatively thick (3.0 to 6.0 mm)(Zeng et al., 2016). The conventional ICRFB therefore has a relatively low current density of 40 mA/cm^2 and low efficiency of 70%. As a consequence, sizeable cells are needed and inherently a relatively large quantity of ion exchanging membrane material is needed, making the cell stacks expensive of $114 - $116 / kWh, contributing to 60% of the ICRFB capital costs (Zeng et al., 2016). Figure 4 shows the cost build-up of a traditional ICRFB, using the flow-through cell structure.

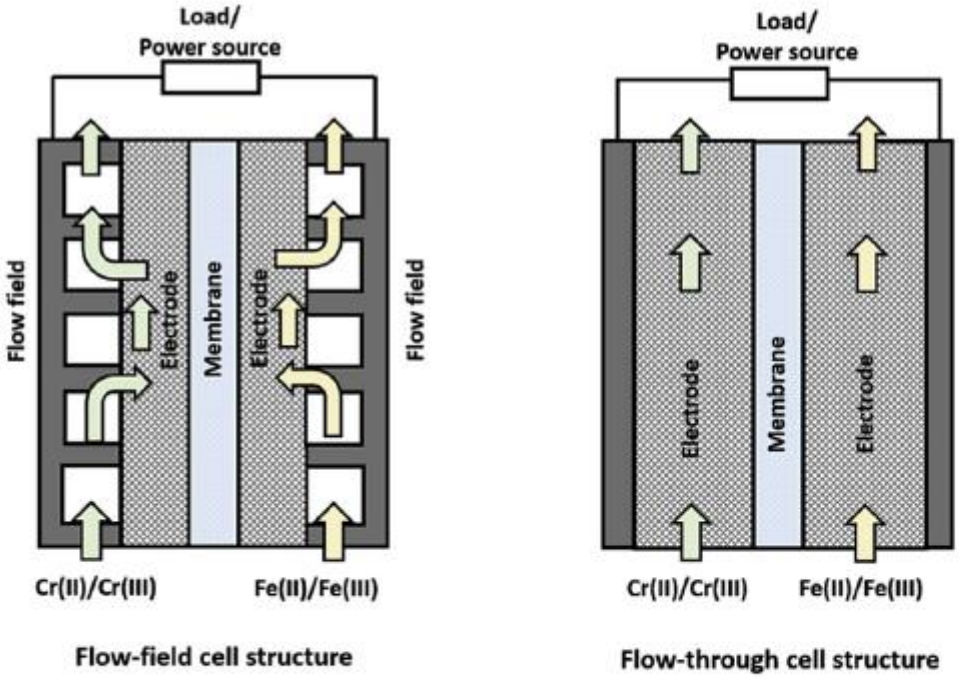

Figure 3: Conceptual image of flow-field and flow-through cell structure (Zeng et al., 2016).

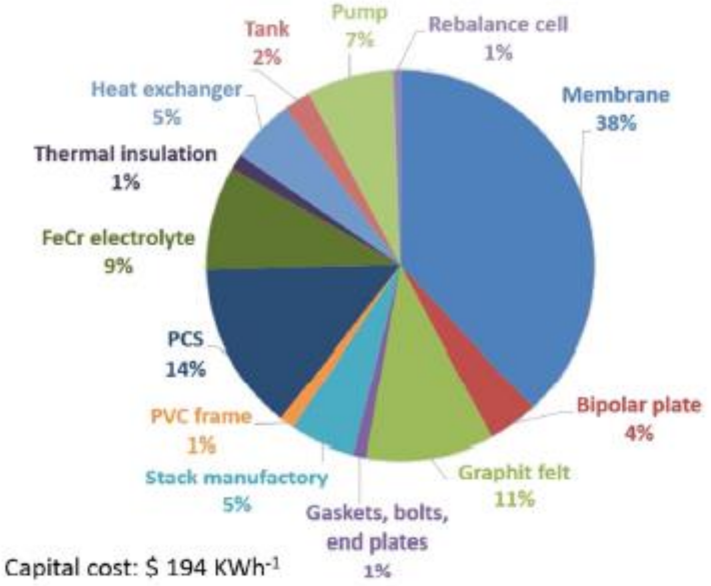

Figure 4: Capital cost breakdown of a traditional 1 MW – 8 hour ICRFB system – 100% being $194/kWh (Zeng et al., 2015).

Considering stability however, the system shows weakness to capacity degradation. Degradation in this system occurs due to cross-over contamination of the Fe and Cr ions, as well as due to hydrogen evolution at the negative electrode. The ICRFB shows capacity decay in the range of 0.6-1.2% per cycle, which could be reduced to 0.3% per cycle by adding a rebalancing cell to the system (Zeng et al., 2015, 2016). The rebalancing cell eliminates the adverse impacts of hydrogen evolution by reducing the excessive Fe^{3+} ions in the positive electrolyte by using the hydrogen evolved from the negative electrolyte (Zeng, Zhao, Zhou, Zou, & Ren, 2017).

Furthermore, this battery has 1) the advantage of independent scalability of power and capacity, 2) energy efficiencies in the range of 70%-80%, dependent on current density and operating temperatures (Zeng et al., 2015, 2016), 3) a relatively low standard cell potential of 1.18V (with required charging values high enough to induce hydrogen evolution), 4) a very low energy density being less than 10 Wh/kg (Leung et al., 2012) and 5) an operating range between 15°C and 65°C, with 65°C resulting in the highest current density and energy efficiency. Note however, that although high operating temperatures increase the energy efficiency, it also increases capacity decay through enhanced cross-over contamination.

All-liquid All-Vanadium RFB (all-VRFB)

The all liquid all-VRFB is currently the most advanced, most mature type of redox flow battery and was invented at the university of New South Wales by Skylass-Kazacos in 1986 (Soloveichik, 2015). This battery uses vanadium both in the catholyte and anolyte and the redox couples are respectively V^{4+}/V^{5+} and V^{2+}/V^{3+}. These components used to be dissolved in hydrochloric acid, but it was found that the V^{4+}/V^{5+} ions were more stable in sulphuric acid (Cunha, Martins, Rodrigues, & Brito, 2014). The kinetics of the V^{2+}/V^{3+} electrochemical reaction are very fast whereas the reaction of the V^{4+}/V^{5+} couple is slower due to the complexity of the reaction. Similar to the ICRFB an ion exchanging membrane is used that only allows the exchange of protons, while not allowing passage of vanadium ions. Furthermore, porous carbon felt electrodes are mostly used in the all-VRFB and different type flow field combinations have been researched, such as the interdigitated, serpentine or conventional flow field, as shown in Figure 5 (Kumar & Jayanti, 2016). This type of research shows that dependent on the viscosity and kinetics of the reactions, different type of flow fields are more suitable.

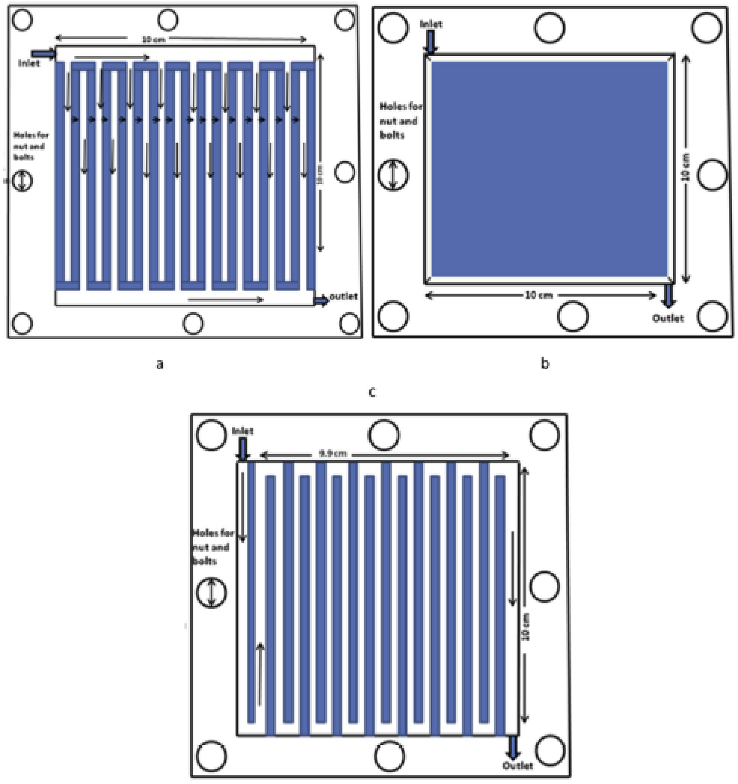

a

b

c

Figure 5: possible flow fields: a) interdigitated, b) conventional and c) serpentine (Kumar & Jayanti, 2016).

The safety of this battery is high when considering fire hazards due to the aqueous sulphuric acid electrolyte. Although the safety datasheet of sulphuric acid does not raise concerns for using this type of battery for large-scale energy storage, according to the safety datasheet this substance still has substantial corrosive properties, both to metals and skin, and can cause serious injuries when direct physical contact is made. Moreover, vanadium is very toxic to aquatic life. One does not have to fear poisonous gasses, as only hydrogen evolution may occur in very small quantities as a side reaction.

The largest downside of the all-VRFB are the high costs of the vanadium electrolyte, making up 53% of the capital costs of an 1 MW – 8 hour system. Figure 6 shows the cost breakdown of an 8 hour all-VRFB. The total capital costs are $229/kWh and considerably higher than that of the ICRFB (Zeng et al., 2015).

Crossover contamination is inevitable, even though advanced ion exchanging membranes are used. Nonetheless, a large advantage of the all-VRFB is that because of the use of vanadium in both the anolyte as well as catholyte, cross-over contamination will never irreversibly degrade the capacity of the battery. In the worst case, after a certain amount of cycles, one must rebalance the electrolytes. This is relatively easy for the all-VRFB in contrast to systems with different metals in the catholyte and anolyte (Cunha et al., 2014). Scientific articles show a lifetime and cycle lifetime of the all-VRFB of respectively 10-20 years and 5000-7000 full charge-discharge cycles, where cycle lifetimes as high as 270.000 cycles even get claimed by manufacturers. The cycle lifetime of the all-VRFB depends inherently on the durability of its components, of which the membrane is a major cost driver and thus an important one. An accelerated stress test showed that the membrane lifetime is in the range of ~4000 hours, mostly due to the highly oxidizing nature of V^{5+} (Oldenburg, Ouarga, Schmidt, & Gubler, 2019).

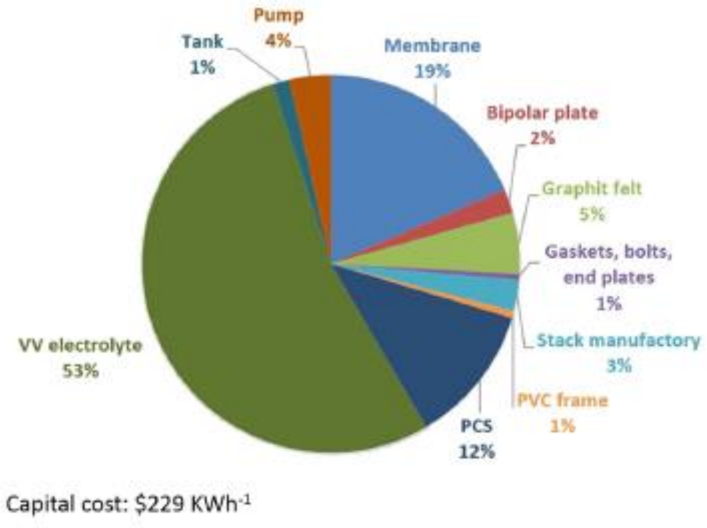

Figure 6: Capital cost breakdown of a traditional 1 MW – 8 hour all-*VRFB system – 100% being $229/kWh (Zeng et al., 2015).*

The all-VRFB has a slightly higher energy efficiency than the ICRFB, in the range of 75-85% and an energy density of around 20-33 Wh/L (Skyllas-Kazacos, Kazacos, Poon, & Verseema, 2010). The energy density is limited due to the instability of the vanadium at concentrations above 2M (e.g. precipitation occurs >2M). Vanadium stability is influenced by solution temperature, the concentration of supporting electrolyte, additives and state of charge (Leung et al., 2012).

All-liquid Polysulphide-Halide RFB (PHRFB)

In order to tackle the high material cost and low energy density of the currently commercialised conventional all-VRFB, the all-liquid Polysulphide-Halide RFB was introduced by Remick et al. in the 1983. Polysulphides have a high solubility, which translates into a high energy density possibilities. Moreover, they are inexpensive and the electrochemistry of the S^{2-}/S_2^{2-} redox couple is highly reversible (S. Zhang et al., 2019). They can replace the anodic V^{2+}/V^{3+} redox couple of the conventional VRFB and can be combined with a cathodic halide redox couple, such as demonstrated for Br^-/Br_3^- and I^-/I_3^- (Zhejun Li, Weng, Zou, Cong, & Lu, 2016; S. Zhang et al., 2019). The Polysulphide-Bromide RFB was successfully demonstrated, but for safety reasons, it is unwishful to use bromide for large-scale energy storage due to its toxicity for both humans and the aquatic environment. However, iodide is much safer and additionally shows much higher reaction kinetics, enabling high power applications (Zhejun Li et al., 2016). Therefore, the focus within the all-liquid PHRFBs is the Polysulfide-Iodide RFB, with a theoretic energy density of 80 Wh/L. This battery has been demonstrated in 2016, where (i) carbon plates were used as current collectors, (ii) Viton gaskets were used for sealing purposes, (iii) a PTFE frame acted as flow channel, (iv) graphite felt that was pre-treated in sulphuric acid was used as positive electrode, (v) nickel foam that was pre-treated in K_2S_2 was used as negative electrode, (vi) a K^+ conducting Nafion membrane was used as separator, (vii) a peristaltic pump transports the electrolyte, (viii) the catholyte was KI dissolved in ultrapure water and finally the anolyte was K_2S_2 dissolved in aqueous potassium hydroxide (Zhejun Li et al., 2016).

When considering safety, the aqueous background of both the catholyte and anolyte reduce fire hazards to a minimum. After consulting the safety datasheet of potassium hydroxide, it is concluded that one must use this substance with care, but no serious considerable threats towards environment or personal safety appear with respect to large-scale energy storage. The safety datasheet of iodine shows that this is a considerably dangerous substance that is harmful when inhaled, causes severe skin burn, eye damage and is very toxic to aquatic life. However, in contrast to the bromide battery variant, the iodide battery variant does not have a side reaction that releases toxic iodine vapour (Figure 7). Even though the Polysulfide-Iodide RFB does not show immediate large-scale danger to human life, it is at the very least debatable whether it is responsible to use these compounds for large-scale storage.

Based on the used materials the chance of economic penetration of this battery is considered to be high. With sulphur being the 11th richest element in the earth's upper crust, this element is inexpensive as was shown by a reported chemical cost of \$1/kWh for a lab scale hybrid aqueous polysulfide-air RFB (S. Zhang et al., 2019). Recall that the vanadium electrolyte makes up for more than 50% of the material cost for an 8 hour VRFB system, and being able to bypass this obstacle greatly enhances chance of economic penetration. However, Iodine is only the 63rd most abundant element in the earth's crust which drives the cost per kWh of the active material up to \$85.4/kWh (Zhejun Li et al., 2016). When then considering that the remaining setup is similar to the traditional all VRFB, the cost breakdown of Figure 6 can be used to estimate the cost of the remaining components to be \$107.6/kWh (membrane, pump, tanks, electrodes, etc.). The total cost for estimation of the Polysulfide-Iodide RFB is then \$193/kWh for a 1MW – 8h system. This is 15.7% cheaper than the traditional VRFB and equal to the costs of a ICRFB.

Considering stability, experiments show that the Polysulfide-Iodide RFB shows marginal capacity retention, namely >98% over 50 cycles (Zhejun Li et al., 2016). When extrapolating this to 1000 cycles, 67% of the capacity would be left. This indicates that this battery might only be viable for multi-hour configurations, unless further research is done into increasing capacity retention by preventing cross-over contamination and prevention of side reactions. Recent research records a stable energy efficiency retention of 96% after approximately 1000 hours when applying nanostructured CoS_2/CoS heterojunction electrocatalyst on graphite electrodes (Ma et al., 2019). The corresponding energy efficiency at 10mAh is 84.5%. For 20mAh this went down to <80%, with even lower energy efficiencies at higher current densities (Ma et al., 2019).

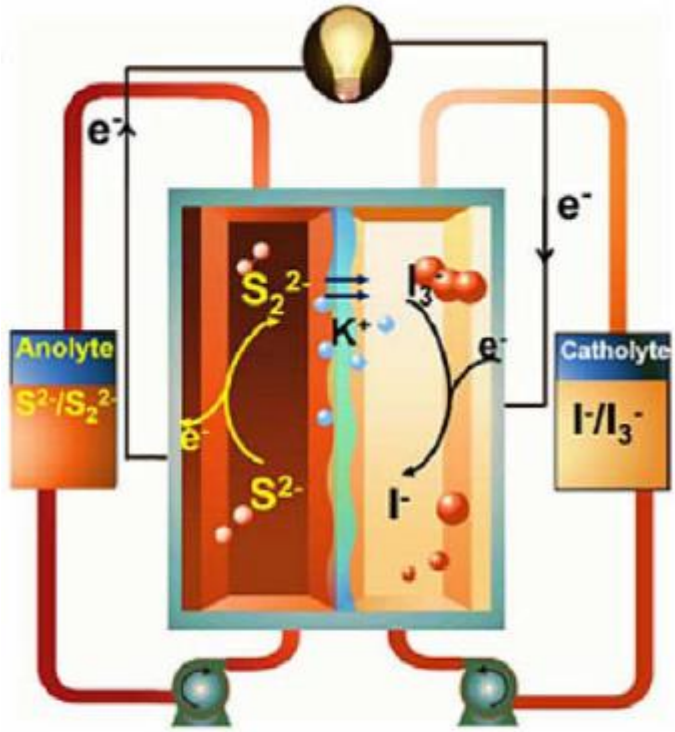

Figure 7: Schematic design of Polysulfide-Iodide RFB (Zhejun Li et al., 2016).

2.1.2. Semi-Solid RFBs

In the search for redox flow batteries that have a higher energy density and potentially lower costs than the traditional all-liquid RFBs, the semi-solid redox flow battery (“SSRFB”) was demonstrated for the first time in 2011 using organic electrolyte (Duduta et al., 2011). The semi-solid RFB is similar to the all-liquid RFB (Figure 8). The main difference is that instead of dissolving the electro-active species in the electrolyte, a semi-solid suspension of high energy electro-active materials is used. This can increase the potential energy density up to tenfold with respect to traditional all-liquid RFBs, as a result of the much greater energy density that solid storage particles intrinsically have and the fact that you are no longer restricted by the solubility (Duduta et al., 2011). An immediate downside to this it that the introduction of solid particles in the electrolyte inherently increases its viscosity, resulting in higher pumping losses and an overall decrease of system efficiency. A second difference with respect to the all-liquid RFB is that a conductive nanoparticle suspension is used to give the flowing electrodes electronic conductivity, opposed to the traditional case where conductivity only takes place at the solid electrodes within the stack where the redox reactions occur. A third difference is that, instead of using an expensive ion-exchanging membrane with a pore size in order of magnitude of nanometres, it may suffice to use a significantly (up to 100 times) cheaper separator with pore sizes in order of magnitude of micrometres (Zheng Li et al., 2013). After all, cross-over contamination is easier to prevent when the electrolyte inhabits relatively large solid particles instead of dissolved ones. Furthermore, the semi-solid RFB maintains the advantages of the all-liquid RFB regarding independent scalability of power and capacity, and increased safety with respect to other battery types such as Li-ion (when regarding aqueous electrolytes). Demonstration of this type of battery is only being conducted for less than 10 years and no demonstrations have been done using cheap and abundant active species. The following paragraphs will shed a light on the aqueous $LiTi_2(PO_4)_3$–$LiFePO_4$ SSRFB (Zheng Li et al., 2013) and the non-aqueous (organic) $LiFePO_4$ ("LFP") and the Li_4TiO_{12} ("LTO") SSRFB (Wei et al., 2015).

Figure 8: Semi solid redox flow battery (Duduta et al., 2011).

Aqueous Semi-Solid $LiTi_2(PO_4)_3$–$LiFePO_4$ RFB

The first ever aqueous SSRFB demonstrated is the $LiTi_2(PO_4)_3$–$LiFePO_4$ SSRFB in 2013 (Zheng Li et al., 2013). It is worth mentioning that the paper by Zheng Li et al. emphasises that a $\$2\ \mathrm{m}^{-2}$ microfiltration membrane suffices instead of having to use a $\$500\ \mathrm{m}^{-2}$ Nafion ion exchanging membrane, like with the previous all-liquid RFB examples. When comparing this particular system to the all-liquid RFBs, it becomes clear that the semi-solid approach increases the energy density of the system as values of 100-300 WhL^{-1} are reported for this aqueous system, based on the solid reactants alone (Zheng Li et al., 2013). This has further economic benefits as it reduces balance of system and system overhead costs.

Although this particular system scores great regarding safety and has the potential to have lower capital costs than the all-liquid RFBs, it is still based on the relatively scarce element lithium (Hurd, Kelley, Eggert, & Lee, 2012). Furthermore, the demonstration has made it clear that this system is dominated by degrading side reactions such as anode-mediated hydrolysis, resulting in H_2 formation, and precipitation in the cathode suspension due to excessive $Fe(OH)_3$ formation, as $LiFePO_4$ is unstable in alkaline environments (Zheng Li et al., 2013).

Nonetheless, as a pioneering experiment, important lessons have been extracted from this demonstration with possible relevance to future research into SSRFB. The experiment was setup in a way in which the chemical inefficiencies could be separated from the flow-induced inefficiencies. This way the operating conditions that maximise flow cell efficiency could be identified. The demonstrated suspensions exhibited shear-thinning behaviour and the demonstration showed that for this type of suspension maximum efficiency could be retained through plug flow, during wall slip conditions, and with slow flow rates. Regarding the pumping volumes, the demonstration has shown that the efficiency declined as soon as the pumped volume exceeded the flow cell volume (Zheng Li et al., 2013). Note that a prerequisite for using these observations for future experiments is that the rheological features of a suspension have to be similar, at the very least being shear-thinning.

Organic Semi-Solid LFP LTO RFB

Whereas the previous paragraph gave insight in the rheological and economical aspects of the SSRFB, current paragraph goes into depth on how to create a stable suspension. Optimization of biphasic electrode suspensions for use in SSRFBs is complicated, yet important. This can be understood by for example the following opposing relationship: When considering the suspensions, both their ability to charge/discharge efficiently and flow readily through the flow cell are influenced by the carbon black network. However, an increase of carbon black concentration both increases conductivity (which aids charge transfer) and viscosity (which increases the required pumping energy) (Wei et al., 2015).

Therefore, in a 2015, a SSRFB was presented and optimised based on biphasic organic suspensions, created by addition of polyvinylpyrrolidone (“PVP”) (Wei et al., 2015). Although organic suspensions are not the focus of this thesis, this paper teaches a lot on how stable semi-solid suspensions in polar biphasic solvents, such as water, are acquired.

The SSRFB in this paper was demonstrated for electrolyte suspensions holding $LiFePO_4$ (“LFP”) and Li_4TiO_{12} (“LTO”) as active species. Ketjenblack EC-600JD (“KB”) particles were added to the suspension to form a conductive network at low percolation threshold. The fact that KB has a low percolation threshold means that a relatively low concentration of KB is needed in order to form an electrical pathway for electron transfer throughout the suspension. At 2 wt% KB the conductivity had a value of 25 mS/cm (Wei et al., 2015). The biphasic mixture was acquired by tailoring the interactions between the active particles LFP and LTO to be repulsive and the interactions between the conducting KB particles to be attractive, and cross-interactions between LFP-kb to also be repulsive, by addition of PVP. This biphasic approach maintains the intrinsic advantage of a high active material content (hence high energy density), yet simultaneously shows improved flow behaviour and electronic conductivity (Wei et al., 2015). By addition of the right amount of PVP, fast aggregation of colloidal LFP due to Van der Waals interactions was prevented, while maintaining the attractive forces between the KB particles (Wei et al., 2015). All in all, it is shown that stabilization of colloidal particles in both aqueous and non-aqueous media through addition of KB and PVP led to well dispersed conductive systems, which is important for charge transfer and adequate flow behaviour.

2.1.3. Single Flow RFBs

The single flow RFB, also known as membranelles RFBs, consists out of solid and stationary cathode and anode electrodes, very similar to the traditional Li-ion technology. However, instead of using a stationary liquid, gel or solid-state electrolyte, the single flow RFB circulates the electrolyte using a pump (Figure 9). While the electrolyte is pumped through the cell the electrochemical reactions take place at the inert electrodes. This can be through the deposition and dissolution mechanism, as demonstrated in aqueous single flow RFBs using the elements copper and zinc (Y. Cheng et al., 2013; Pan et al., 2008), or through the (de)intercalation mechanism, as demonstrated in an organic single flow RFB using the element magnesium (Tian et al., 2017). Through charge and discharge cycles the active species change from a solid state at the electrodes to a dissolved state in the electrolyte that is being circulated.

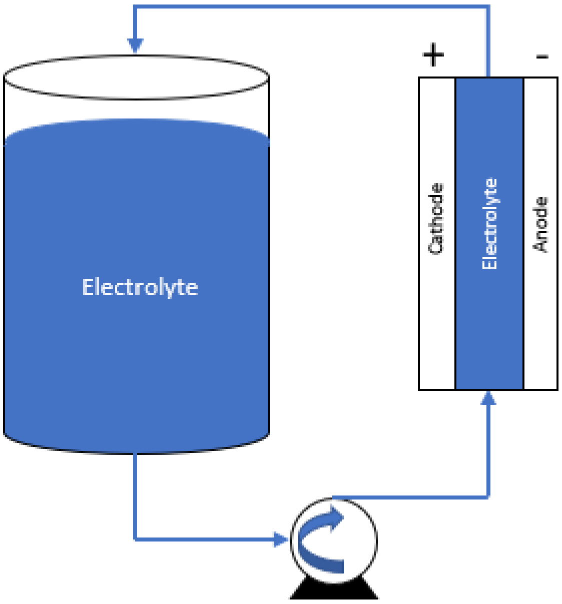

Figure 9: Schematic design of a single flow RFB.

Compared to other RFB technologies, single flow RFBs have gained attention through the possibility to decrease costs regarding the amount of electrolyte, the redundancy of ion-exchanging membranes and the smaller required balance of system (e.g. less pumps). Besides the latter, this system does not suffer from the intrinsic cross-over contamination like the all-liquid RFBs, which has shown to lead to low cycle lifetimes (Zeng et al., 2016) (with the exception of all-VRFB due to the sole use of vanadium as active species). Another advantage of this type of battery is that dendrite formation at the electrodes, a familiar problem within the Li-ion technology, may be avoided because of the circulating electrolyte (Pan et al., 2008). An important downside of this battery is that the unique property of independent scaling of power and capacity is not maintained, unlike the all-liquid and semi-solid RFB. Intuitively, this type of battery seems much like the traditional lead-acid battery, but with increased cycle lifetime and decreased efficiency due to the circulation of the electrolyte. Till this day, no single flow RFB using an aqueous electrolyte as well as using cheap and abundant active materials has been demonstrated. In the next paragraphs more detail is given to the aqueous single flow Cu-PbO_2 RFB and the aqueous single flow Zn-Ce RFB.

Aqueous single flow Cu-PbO_2 RFB

The aqueous single flow Cu-PbO_2 RFB was demonstrated in 2008. While charging, Cu(s) is deposited on the negative electrode and while discharging, Cu^{2+} is dissolved into the H_2SO_4-$CuSO_4$ electrolyte which is pumped through the system (Pan et al., 2008). Use was made of a positive solid state electrode that consists for 98% out of $PbO_2/PbSO_4$ (charged/discharged), intermixed with 1.2% carbon fibre due to its outstanding mechanical and electrical properties (Mohammadzadeh Kakhki, 2019).

The results show a good energy efficiency of 83% and high reaction reversibility. Regarding stability, over a period of 450 cycles a capacity was retained between 2000 mAh and 1941 mAh. While at the first sight this shows potential, note that these results correspond to operation at a low DoD of around 15% (Pan et al., 2008). Future research would have to show how this type of battery would perform under deep cycles, however one can expect the energy efficiency and cycle lifetime to drop. Furthermore, the energy density is restricted by the solubility of the active compounds in the electrolyte, as the experiment showed small particles sedimentation during operation, resulting in loss of capacity (Pan et al., 2008).

Regarding the economic and sustainable choices of the battery in question, it seems suboptimal to use lead and copper as active species for large-scale battery storage, as these are even less abundant in the earth's upper crust than vanadium (although costs are relatively low due to extensive use in industry (Hurd et al., 2012)). This suboptimality is especially true if one would only operate on a DoD of 15%, effectively increasing costs by a factor 5 with respect to a technology that can be cycled at a DoD of 75%.

Although this composition shows no immediate fire hazards due to the aqueous electrolyte, the acidic environment advices for caution (similar to the all-VRFB) and the safety datasheets of copper and lead state that these particles are very toxic to the aquatic environment.

Aqueous single flow Zn-NiOOH RFB

While the previous example gives insight into basic characteristics of an single flow RFB based on metal deposition and dissolution subject to a very low DoD. it fails to give a deeper understanding on failure mechanisms, as the battery is simply not cycled deep enough. Therefore, the aqueous single flow Zn-NiOOH RFB is outlined.

Based on the safety datasheets of zinc and nickel, an aqueous single flow Zn-NiOOH RFB is considered to be safe for both human and environment and is to that regard suitable for large-scale energy storage. Simultaneously, zinc and nickel are both available at the same order of magnitude of abundance as vanadium (Hurd et al., 2012), indicating that these elements are relatively scarce and an economical advantage must primarily be achieved through the cheaper design compared to an all-liquid RFB (membranes irrelevant, only one pump needed, etc.), while operating at sufficiently deep cycles.

A stability discussion on the aqueous single flow Zn-NiOOH RFB mentions that cycling experiments have shown that the energy efficiency stays stable at 86% over 1000 cycles, but that residual zinc remains on the negative substrate, resulting in dendrite formation at the Zn electrode during redeposition (J. Cheng et al., 2007). This instability enhances aging and can cause short-circuit. It is interesting however, that recent research predicts that dendrite formation can be totally eliminated when the electrolyte flow is normal to the electrode on which the dendrite forms, if the electrolyte flow surpasses, a practically low, critical electrolyte velocity (Parekh, Rahn, & Archer, 2020).

2.1.4. Liquid-Gas RFBs

With the aim to achieve lower material costs and higher energy efficiency, the liquid-gas RFB has been introduced. On a high level this type of RFB is most comparable to the all-liquid RFB, with an exception being that one electrode utilises a gas phase as reactant instead of a liquid phase, usually being hydrogen gas. A second difference is that a catalyst is likely to be needed for adequate reaction kinetics. On the other hand, the electrolyte at the other electrode is similar to the all-liquid RFB, in which an active species is dissolved. Another similarity is that these are being separated by ion exchanging membrane. As an illustration, Figure 10 gives the schematic of the hydrogen-bromine liquid-gas RFB.

An advantage of this configuration is that the liquid and gas phase are easily separated, so that the negative effects due to cross-over contamination can be significantly mitigated (Rubio-Garcia et al., 2018). Besides, working with hydrogen gas as feedstock is very economical due to its abundance, especially since the coming decades the hydrogen economy will keep on developing, allowing easy access. At the same time a downside of this configuration is that this type of battery is intrinsically less safe when considering large-scale battery storage. Circulating large volumes of H_2 gas presents significant fire hazards. Second, as previously mentioned, working with ion exchanging membranes is expensive – recall that it made up 38% of the costs of the all-liquid Iron-Chromium RFB (Zeng et al., 2015). Therefore, a smart choice of liquid electrolyte composition is required to be able to financially compete with cheap designs of the semi-solid RFB and the single flow RFB, that don’t require these advanced membranes, while also aiming for compositions with cheap earth-abundant materials. In the next two paragraphs the aqueous hydrogen-bromine and the hydrogen-manganese liquid-gas RFB are discussed in more detail.

Aqueous H_2Br_2 liquid-gas RFB

While discharging, the hydrogen-bromine liquid-gas RFB pumps dissolved Br_2 through a cell to react with circulating H_2 to become HBr (aq). During charge this process is reversed and HBr (aq) is pumped through the cell, producing H_2 gas and Br_2 gas dissolved in HBr (aq). The cell separates the two streams via an cation exchange membrane. Furthermore, platinum is used as catalyst as studies have shown that both bromine and hydrogen have fast and highly reversible reaction kinetics on platinum (Cho et al., 2012). Integration of this catalyst is done via a platinum coating layer on the membrane. Furthermore, porous carbon layers are used as electrodes.

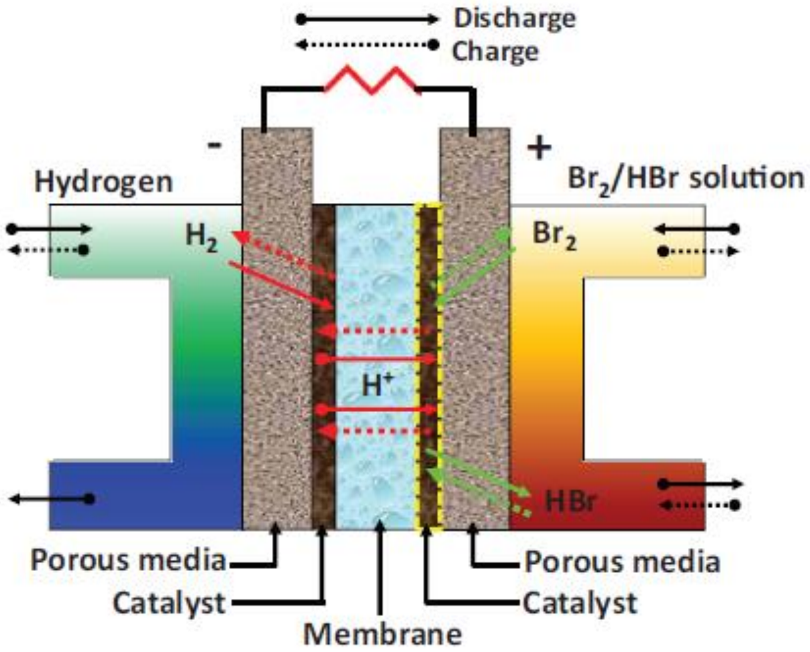

Figure 10: Schematic of the H_2Br_2 liquid-gas RFB (Cho et al., 2012).

The mean degradation phenomenon is when bromine adsorption occurs on the negative platinum catalyst, decreasing its effectivity over time. This is caused by bromide crossover through the membrane that poisons the catalyst that supports the hydrogen evolution and oxidation reactions (Saadi et al., 2019). Recently, successful efforts have been made to solve this problem through the integration of a semi-permeable layer on the platinum catalyst to block out the bromine species. Results have shown that whereas the original design almost shows instant degradation of capacity and power, the new design stays stable for 100 cycles without capacity degradation, having an energy efficiency of 72% when operating at 40°C (Saadi et al., 2019). Future research would need to show for how many cycles the semi-permeable layer would be effective, as X-ray pictures did show a decrease in platinum catalyst particles after 100 cycles.

Regarding the economics of this battery, it is advantageous that use is made of cheap hydrogen that doesn't require heavy pumping. But bromine is two orders of magnitude less abundant than vanadium and significant quantities are required (Yaroshevsky, 2006). Also, even though significant smaller quantities are needed, the required use of platinum that is five orders of magnitude less abundant than vanadium sets an unfavourable starting point (Hurd et al., 2012).

Above this, when considering large-scale energy storage, it seems very unwishful to be dependent on large quantities of bromine. Bromine gas is highly toxic and boils at 59°C (Cho et al., 2012). Although there exist techniques that turn potential bromine gas into unhazardous complexes, the health risks are too high to consider this specific technology.

Aqueous H_2Mn liquid-gas RFB

The previous hydrogen-bromine technique gives insight in how a stable liquid-gas RFB can be realised, but lacks safety and economical perspective. The aqueous hydrogen-manganese liquid-gas RFB however, uses manganese instead of bromide as active species at the cathode side. This tackles both the high toxicity as well as the scarcity problem of bromine, since

manganese is unharmful and the 12th most abundant element in the earth's crust (Yaroshevsky, 2006).
The way in which this specific battery works is almost identical to the aqueous H_2Br liquid-gas RFB. However instead, manganese is dissolved in the sulphuric acid electrolyte and charged/discharged between de second and third oxidation state. Regarding stability, it is common knowledge that Mn^{3+} in an aqueous environment undergoes disproportionation into dissolved Mn^{2+} and solid MnO_2 particles (Rubio-Garcia et al., 2018). Formation of these particles result in capacity and power degradation of the battery. Results from Rubio-Garcia et al. show that addition of Ti^{4+} effectively counters the disproportionation of the Mn^{3+}, thereby maintaining a stable electrolyte with dissolved manganese particles. Furthermore, the research shows that the Pt catalysts are not permanently being poisoned by manganese and titanium crossover during discharge, although X-ray spectroscopy indicates that this phenomenon does occur (Rubio-Garcia et al., 2018). It is assumed that these adsorbed particles are being pushed back during the charge reaction, indicated by a brief overpotential at the start that stabilises after a while (Rubio-Garcia et al., 2018). The energy efficiency is recorded at 82%.

2.1.5. System Choice - the Iron-Manganese SSRFB

In conclusion of this preliminary literature study, an aqueous SSRFB based on cheap, insoluble iron and manganese solid electroactive materials is chosen as a system that shows potential with respect to safety, costs and durability. A SSRFB may have the downside of increased pumping losses due to viscous electrolyte, but using cheap and safe active materials and a cheap microfiltration membrane in combination with the pro of a fully aqueous electrolyte, subject to low cross-over contamination and having resilience against dendrite formation outweighs the cons of the other systems: (i) All-liquid RFBs already have extensively been researched and remain to have crossover contamination and energy density problems (even the expensive all-vanadium RFB will at the very least have to rebalance), while no stable compositions based on cheap materials are found. (ii) Liquid-gas RFBs intrinsically increase safety hazards as they are currently being developed with flammable hydrogen and poisonous bromine gas and no literature is found indicating that cheap materials can be used in stable configurations. (iii) Single flow RFBs lose their decoupled character of power and capacity as well as they are susceptible to dendrite formation when considering deposition/dissolution systems, whereas no real perspective is shown regarding aqueous intercalation systems.

More specifically, the chosen SSRFB system is based on $Fe(OH)_3$, $Fe(OH)_2$, $Mn(OH)_3$ and $Mn(OH)_2$ electroactive materials. Iron is the fourth most abundant and manganese is the twelfth most abundant element in the earth's upper continental crust (Yaroshevsky, 2006). Further research shows that, besides being abundant, these materials are cheap and they are not on the list of energy-critical elements (Hurd et al., 2012)(Appendix A). Based on Eq. 1, in an idealised situation (no losses and full utilization of active material), an amount of 2.9 kg active Fe and 2.9 kg active manganese can provide one kWh of storage, resulting costs of < €6 per kWh (Appendix A).

Although the electrochemical operation of this combination has never been shown before and little is known about the electrochemical behaviour between these specific insoluble iron- and manganese complexes, the relationship in Eq. 1 is introduced as proposed spontaneous reaction and the theoretical cell voltage at standard conditions. Immediately note that this system needs an alkaline environment to function and the cell voltage at standard conditions is way below the value at which electrolysis of water occurs. More depth is given in Chapter 2.2, proceeded by the respective fundamentals of electrochemistry.

$$\mathrm{Mn(OH)_3 + Fe(OH)_2 \rightarrow Mn(OH)_2 + Fe(OH)_3} \quad \mathrm{E^0_{cell} = 0.71\ V} \tag{1}$$

Eq. 1 is based on the following half-cell reactions at standard testing conditions retrieved from the electrochemical series of the handbook of chemistry and physics (Lide, 2010). The cathode and anode notation refers to the setup in which spontaneous discharge occurs.

$$\mathrm{Mn(OH)_3 + e^- \leftrightarrow Mn(OH)_2 + OH^-} \quad \mathrm{E^0_{cat} = 0.15\ V} \tag{2}$$
$$\mathrm{Fe(OH)_3 + e^- \leftrightarrow Fe(OH)_2 + OH^-} \quad \mathrm{E^0_{an} = -0.56\ V} \tag{3}$$

The insolubility of active material has the potential to prevent cross-over contamination and degradation of the battery, setting this technology up for high cycle lifetimes. Moreover, this enables the potential for higher energy densities as one is not limited by the solubility of the active species. Even more, one can now use cheap microporous membranes instead of expensive ion-exchanging membranes as the particles are too large to pass through. According to the handbook of chemistry and physics, the proposed materials are all insoluble except for $Mn(OH)_3$ (for which no information was available)(Lide, 2010). Now, it is known that oxides and hydroxides generally dissolve very badly in aqueous conditions, especially at high pH. When additionally consulting a study on the solubility of manganese and iron in water, it follows that iron and manganese in general have low solubility in an aqueous solution with a pH > 8.5 (Figure 11), it is therefore assumed that the proposed hydroxide complexes of Eq. 1 are insoluble at highly alkaline conditions.

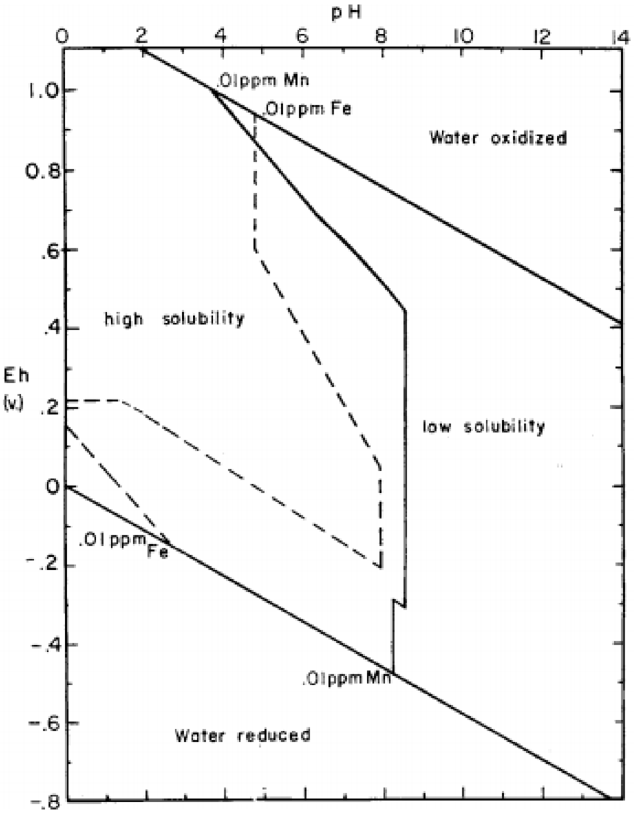

Figure 11: E_h and pH at which manganese and iron can be present in solution at equilibrium at activities greater than 0.01 ppm (Hem, 1963)

Some final advantages of the SSRFB in general are that no mention has been made in previous literature about degradation through dendrite formation and that the SSRFB maintains the decoupled character of power and capacity. However, no demonstrations have been shown in an aqueous environment using earth abundant, non-toxic active species, which is a requirement with respect to the set key characteristics for large-scale energy storage as mentioned in the introduction of this MSc thesis.

2.2. Semi-Solid Iron and Manganese Electrode Suspensions

From multiple demonstrations of SSRFBs follows that proper development of the SSE suspensions is a prerequisite for an effective SSRFB system (J. Cheng et al., 2007; Zheng Li et al., 2013). Therefore this second literature study introduces the design of the iron-manganese SSRFB and aims at describing the most important electrochemical aspects. This is followed by providing the theoretical framework and considerations regarding the key-design parameters for the design of SSE suspensions, so that these can be effectively developed and tested.

Chapter 2.2.1 introduces the design of the iron-manganese SSRFB. In Chapter 2.2.2 the most important fundamentals of electrochemistry are explained and related to this particular system. In Chapter 2.2.3 it is explained that ionic conductivity can be effectively achieved through the use of a 5M KOH solution and from Chapter 2.2.4 follows that electronic conductivity can be successfully realised by creating a percolating carbon black network using KB particles. Then, in Chapter 2.2.5, the respective conductivity measurement techniques are explained and related to this system, setting ourselves up for the practical lab work. After this, Chapter 2.2.6 dives into the theory behind colloidal stability, as this is closely related to stable suspensions. The literature study is finalised by Chapter 2.2.7, in which the chemical stability of the proposed active materials is shortly reviewed for a deeper understanding of the system.

2.2.1. Iron-Manganese SSRFB Design

Whereas Section 2.1.5. introduced the iron-manganese SSRFB design and focussed on its justification, this section introduces the high-level design of the iron-manganese SSRFB and its key-design parameters. In the following sections of Chapter 2.2 these will be further elaborated. The spontaneous electrochemical discharge reaction (Eq. 1) proposed in the iron-manganese SSRFB system involves the reduction of $Mn(OH)_3$ to $Mn(OH)_2$, including the net release of an OH^- ion, and the oxidation of $Fe(OH)_2$ to $Fe(OH)_3$, including the net consumption of an OH^- ion. The discharge reactions are presented in Eqs. 4 and 5 at standard conditions. During spontaneous discharge, the Mn-SSE suspension functions as the cathode and the Fe-SSE suspension as the anode. This process would be opposite during charge. To enable a reversible reaction an alkaline environment is required, such as a KOH or NaOH solution. Figure 12 gives a graphical illustration of the system at SoC = 100%. Furthermore, in the proposed system, the active particles are suspended throughout the catholyte and anolyte. This means that in order to enable proper electrochemical operation, an environment must be provided that offers electronic and ionic conductivity throughout the whole suspension. The earlier literature study has already shown that this can be realised by creating a percolating network of CB. The particles in the system must subsequently remain stably suspended so that the system remains operational over time, which can be done by adding an emulsifier (e.g. it can be easily understood that sedimentation of the heavier solid active materials and flotation of the light weight carbon black particles would result in an ineffective system). A membrane (preferably microfiltration) separates the catholyte and anolyte suspension and enables charge compensation. Finally, current collectors in both the catholyte and anolyte gather the electrons and connect these to an external circuit, thereby closing the electronic circuit.

$$\text{Cathode:}\quad \mathrm{Mn(OH)_3 + e^- \rightarrow Mn(OH)_2 + OH^-} \qquad \mathrm{E^0_{cat} = 0.15\ V} \tag{4}$$

$$\text{Anode:}\quad \mathrm{Fe(OH)_2 + OH^- \rightarrow Fe(OH)_3 + e^-} \qquad \mathrm{E^0_{an} = -0.56\ V} \tag{5}$$

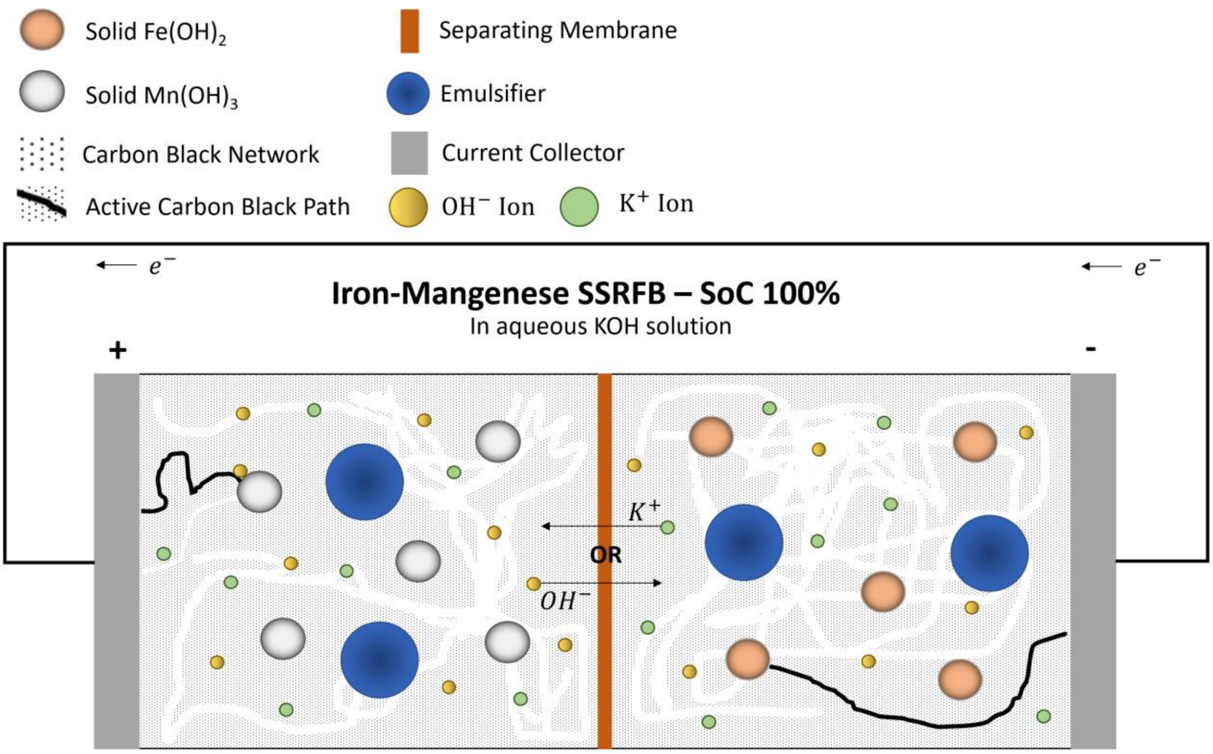

Figure 12: Illustration of the iron-manganese SSRFB at SoC = 100%

2.2.2. Electrochemistry

In this section the relevant electrochemical theoretical background is shared and coupled with the proposed iron-manganese SSRFB system. Amongst others, it presents the Nernst equation, its connection to Gibbs free energy change, Faradays law and the main factors behind the kinetics of an electrochemical system. Throughout the introduction of these, it relates them to the proposed iron-manganese SSRFB.

One of the fundamentals in the field of electrochemistry is the Nernst equation, which can be used to calculate the maximum potential of an electrochemical cell containing a reversible system. This equation holds only for reactions with fast kinetics and only at the surface of the electrode (Ciobanu, Wilburn, Krim, & Cliffel, 2007):

$$\mathrm{E_{cell}} = \mathrm{E^0_{cell}} - \frac{\mathrm{RT}}{\mathrm{nF}} \ln \mathrm{Q_r} \tag{6}$$

Where in the case of the hypothetical reversible reaction:

$$\alpha\mathrm{A} + \beta\mathrm{B} \leftrightarrow \gamma\mathrm{C} + \delta\mathrm{D} \tag{7}$$

Applies:

$$\mathrm{Q_r} = \frac{\mathrm{a_C^\gamma\, a_D^\delta}}{\mathrm{a_A^\alpha\, a_B^\beta}} \tag{8}$$

For solid materials an activity of unity is valid and for solutions it is accurate enough to take the concentration as activity (Ciobanu et al., 2007). It must furthermore be noted that the value for E_{cell} corresponds to the maximum potential at zero current running through the system, which is also known as the OCV. Next this, for an electrochemical cell it is valid that the reaction is spontaneous (exothermic) if $E_{cell} > 0$ V and non-spontaneous if $E_{cell} < 0$ V. The electrochemical cell potential at standard conditions can be related to the cathode and the anode cell potentials at standard conditions via:

$$\mathrm{E}^0_{\mathrm{cell}} = \mathrm{E}^0_{\mathrm{cat}} - \mathrm{E}^0_{\mathrm{an}} \tag{9}$$

In addition, Eq. 6 is connected to the Gibbs free energy change as follows:

$$\Delta\mathrm{G}^0_{\mathrm{cell}} = -\mathrm{nFE}^0_{\mathrm{cell}} \tag{10}$$

The Gibbs free energy change can then directly be related to the equilibrium constant, which can thus effectively be obtained by a single measurement of E^0_{cell}.

$$\Delta\mathrm{G}^0_{\mathrm{cell}} = -\mathrm{RT}\ln\mathrm{K} \tag{11}$$

A second fundamental theory is Faradays law, which connects the total theoretical amount of charge in a cell to the amount of active material (Ciobanu et al., 2007), given by:

$$\mathrm{Q} = \mathrm{nFN} \tag{12}$$

It is powerful that the combination of the above mentioned Eqs. 6-12 provides enough fundamental theoretical basis to answer the research question via the executing of measurements. Now, with this knowledge at hand, it is time to have a closer look at the suggested system.

Using Eq. 9, we can anticipate that the OCV at SoC 100% (maximum potential) and at standard conditions should be E^0_{cell} = 0.15-(-0.56) = 0.71 V. As mentioned in the previous paragraph, a 5M KOH solution will be used in this design (pH 14.7). This deviates the system from standard conditions for which a correction has to be made through the use of the Nernst equation. Appendix C shows how a system in which unity counts as activity for the solid materials and $a_{KOH} = 5$ is taken for the high alkalinity, results in an anticipated E_{cell} = 0.63 V. Although the cell potential of 0.63 V is low to moderate with respect to other systems, the cell potential stays far away from the theoretical 1.23 V where decomposition of water would occur and the half-cell potentials additionally stay within the equilibrium region of water at high alkalinity (Figure 13). Hence, stability and durability of the electrolyte should be maintained with respect to unwishful side reactions following from electrolysis.

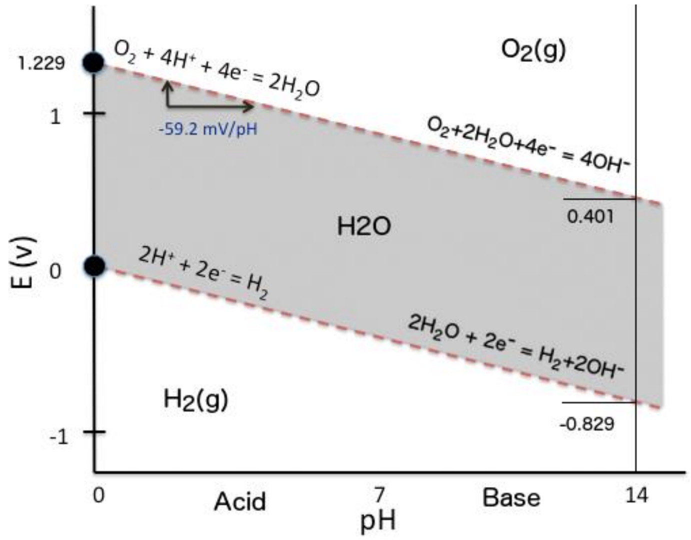

Figure 13: Pourbaix diagram of water, including equilibrium regions for water oxygen and hydrogen during standard conditions (van Loon, Gary; Duffy, 2011).

Little is known about the exact electrochemical process for the two half-cell reactions (Eqs. 2 and 3) during charge and discharge. Literature exists stating proton intercalation and de-intercalation to be the insertion mechanism for MnO_2 in a strong alkaline environment (note Mn^{4+} instead of Mn^{2+} or Mn^{3+}) (Rus, Moon, Bai, Steingart, & Erdonmez, 2016). It is further anticipated that reactions into solid materials with activity unity result into one or more constant voltage plateaus. Similar behaviour is for example found in LFP-LTO technology based on standard solid electrodes, where one clear plateau is found (Léonard & Job, 2019). The existence of more plateaus with would indicate the transition to intermediate forms of iron and manganese, such as iron(II,III) or manganese(II,III) complexes, of which the existence is long known (Pourbaix, Zhang, & Pourbaix, 1997). Figure 14 illustrates possible electrochemical intercalation and de-intercalation for the Fe-Mn SSRFB.

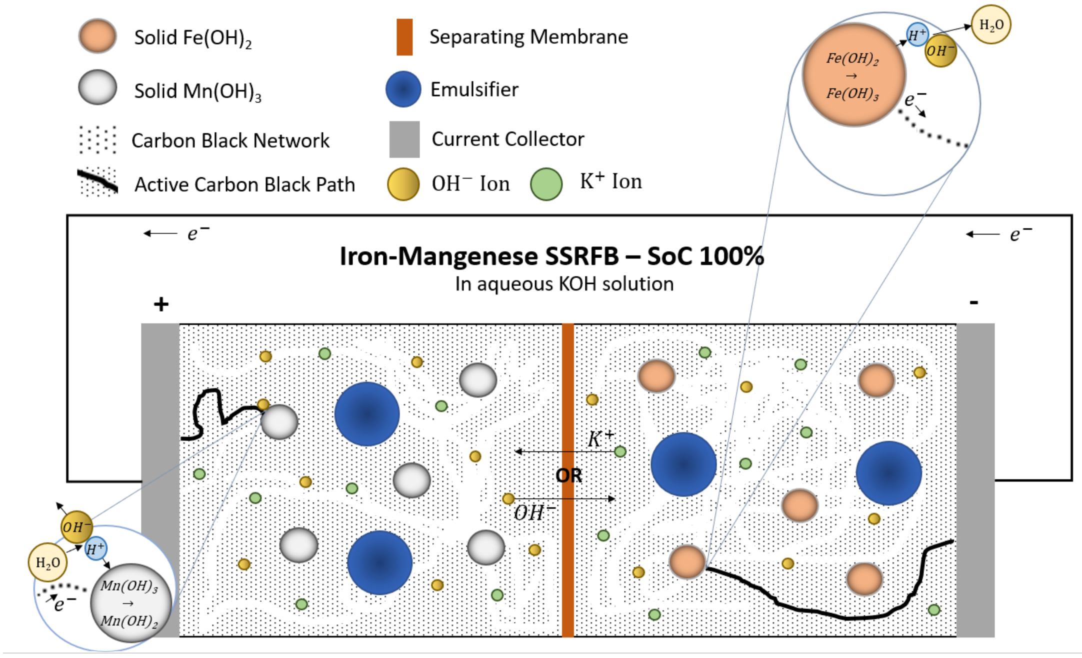

Figure 14: Possible proton intercalation and de-intercalation proposed for the Fe-Mn SSRFB

The kinetics of the system are mainly decided by four major factors: (i) mass transfer to the electrode surface (ionic conduction of suspension), (ii) transfer of electrons by CB through the suspension into the current collector (electronic conduction of suspension), (iii) transfer of electrons from CB into active material and (iv) the intercalation of ions into the active material, also known as the internal resistance. The slowest of which decides the speed at which the reactions can take place (Ciobanu et al., 2007).

2.2.3. Ionic Conductivity

This section explains that a strong alkaline environment of a 5M KOH solution is a good starting point for proper ionic conductivity and thus has a positive effect on the system kinetics with respect to mass transfer to the electrode. Next to this, it expands on why transfer of OH^- ions through the membrane is mainly responsible for charge compensation of the system.

From the electrochemical reactions Eqs. 2 and 3 follows that an alkaline environment is required to make the proposed reactions possible. Additionally, in order to enable a high ionic conductivity, a large amount OH^- charge carriers is required. This means that for the proposed system a strong alkaline environment is wishful, with for example a 5M concentration. Both KOH and NaOH are strong bases and fully ionise in water. However, an important difference between these two is that NaOH is 70% more viscous than KOH at 5M concentrations (Schalenbach, Zeradjanin, Kasian, Cherevko, & Mayrhofer, 2018). Previous research in SSRFBs has shown the significance in maintaining a balance between the opposing design parameters conductivity and viscosity (Qi & Koenig, 2017)(Lead, 2008). It was shown that an increased conductivity comes at the cost of increased viscosity, thus a decreased flowability and increased pumping losses. Therefore, KOH shows preferable characteristics. In an aqueous KOH solution the ionic mobile species are OH^- and K^+ ions. Multiple sources further show a parabolic relationship between the ionic conductivity and the molarity of KOH solutions, peaking at a concentration of 6M KOH (Gilliam, Graydon, Kirk, & Thorpe, 2007; Schalenbach et al., 2018). The difference between conductivity of 5M and 6M shows to be little. Although this gives a starting point, measuring ionic conductivity of SSE suspensions is still critical in being able to investigate the influence of SSE composition on kinetics of mass transfer, especially the influence of the addition of solid particles to the suspensions. Intuitively, one is inclined to say that the addition of solid particles such as carbon black and insoluble electroactive material ($Mn(OH)_2$ and FeOOH) make it more difficult for OH^- ions to manoeuvre through the suspension. However, previous research has shown that this effect is insignificant, following from results based on a system with lithium compounds in organic electrolyte (Biendicho, Flox, Sanz, & Morante, 2016).

Charge compensation of the system can happen via transfer of either K^+ or OH^- ions through the membrane. From these two it is more likely to happen via OH^- ions because of diffusion processes. Take for example the system in Figure 12, as discharge continues OH^- is released during the electrochemical reaction in the cathode suspension and consumed in the anode suspension (Eqs. 4 and 5). The respective charge compensation can happen both via transfer of OH^- from the cathode to the anode, or from K^+ from the anode to the cathode. In the first case a balance in total ion concentration is maintained, while in the second case the cathode suspension will end up having a much greater ion concentration than the anode suspension.

By following this reasoning, as a result of diffusion, the first case is more stable and more likely to happen over larger quantities of charge and mass transfer.

2.2.4. Electronic Conductivity

This section explains that electronic conductivity in SSE suspensions is created via the addition of CB forming a percolating electronic network. Such a network must ensure good transfer of electrons through the suspension to the current collector. Both KB and acetylene black are considered popular choices for CBs in previous designs of suspension electrodes (Ozoemena & Kebede, 2016). Although the conductivity of CB is low with respect to alternatives like carbon onions, carbon nanotubes and graphene, they make up for it in terms of cost, scalability and flowability. An overview of reported suspension electrodes including their electronic conductivity, conductive additive, active materials and electrolyte can be found in Appendix B. This chapter compares KB and acetylene black and discusses their characteristics with respect to electronic conductivity, colloidal stability and viscosity (although viscosity and colloidal stability are touched upon in this chapter, they are dealt with in more depth in Chapter 2.3.6).

A journal paper in which three different type of CBs (acetylene black, KB and Ensaco) are tested with respect to flow applications, reveals an electronic percolation threshold of 3 wt% for acetylene black, 7 wt% for KB and 14 wt% for Ensaco, with a value for $\sigma_e \approx 0.1$ mS/cm (Parant et al., 2017). This was tested in an aqueous solution (pH=7). It was shown that the acetylene black suspension shows a fast and steady increase of σ_e as the wt% CB increases, whereas suspensions with both KB and Ensaco show a very sudden increase of σ_e at the point where they are already viscous (Figure 15). As a result, unlike the others, acetylene black allows conductivity between 0.1 mS/cm till 1 mS/cm, while maintaining fluid-like properties. The difference in behaviour is believed to be related to the way in which the CB particles distribute and agglomerate. By comparison of the clusters morphologies of the CBs, one sees that KB and Ensaco clusters are spherical and very compact, whereas acetylene black shows a more fibre-like network consisting of many small aggregates (Figure 16). These open fractal clusters are believed to induce flexibility, resulting in a low viscosity at percolation threshold. As a result, the research designates acetylene black as the best option for flow applications. Note nonetheless, that values for σ_e are highest for KB between 8%-12% (w_{CB}/w_{water}). If one can justify the use of more paste-like suspensions with higher viscosities, then arguably KB is the better choice. Now, when additionally taking colloidal stability into consideration the playing field between KB and acetylene black levels even more.

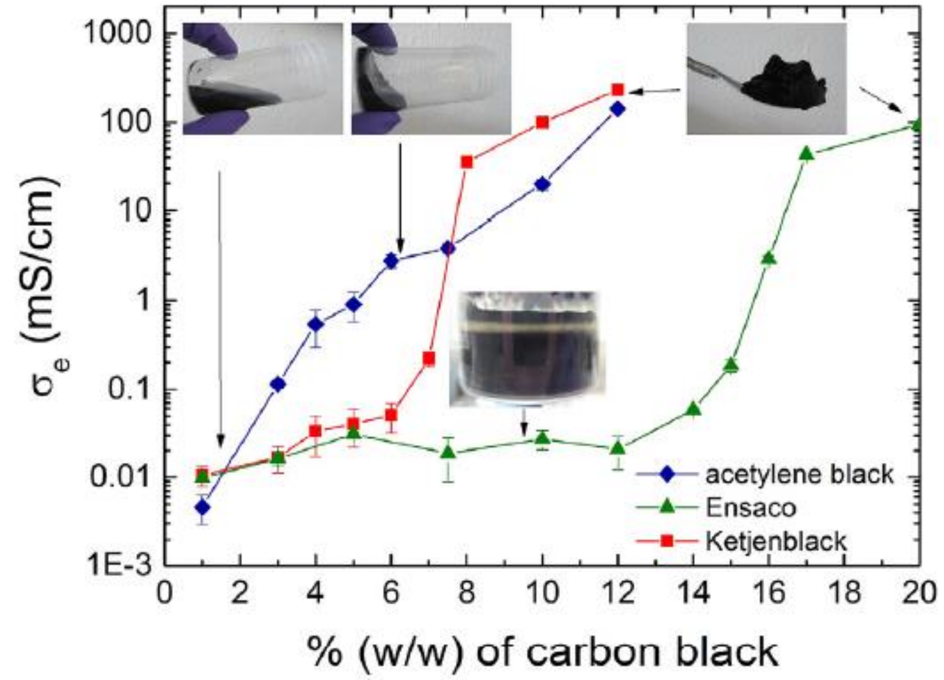

Figure 15: Conductivity of the aqueous suspensions according to percentage w_{CB}/w_{water} of CB particles, including 1.5 wt% arabic gum and 0.5 wt% Alginate to emulsify the suspension. Photos of the corresponding suspensions show how the viscosity increases with increasing CB concentration (Parant et al., 2017).

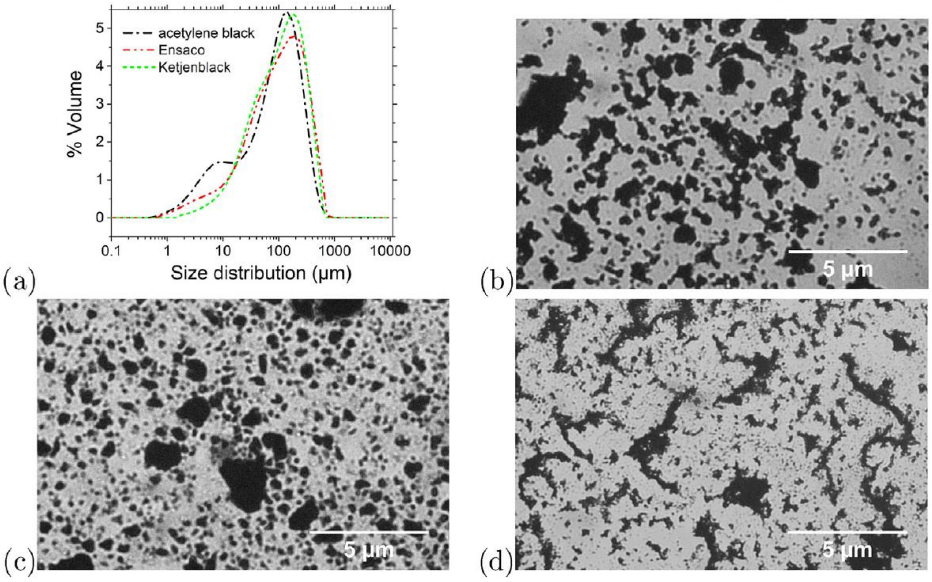

Figure 16: a) Volume size distribution for suspensions containing 0.5 wt% Alginate, 1.5 wt% arabic gum and 1 wt % CB. Optical microscope photographs are included showing the cluster morphology for (b) Ensaco (c) Ketjenblack and (d) Acetylene black (Parant et al., 2017).

A downside of acetylene black is namely that this *must* be combined with an emulsifier in aqueous solutions, as acetylene black is highly hydrophobic (Figure 16d). This colloidal instability is confirmed by the corresponding value for the zeta potential of around 0 mV. For KB this is less of a problem, as the zeta potential of |30 mV| indicates moderate colloidal stability in aqueous solutions (Figure 17a). This stipulates that less emulsifier is required to create a stable colloidal suspension using kb, which results in being able to increase the KB wt%, thus σ_e, with respect to the acetylene black wt% while maintaining a similar viscosity.

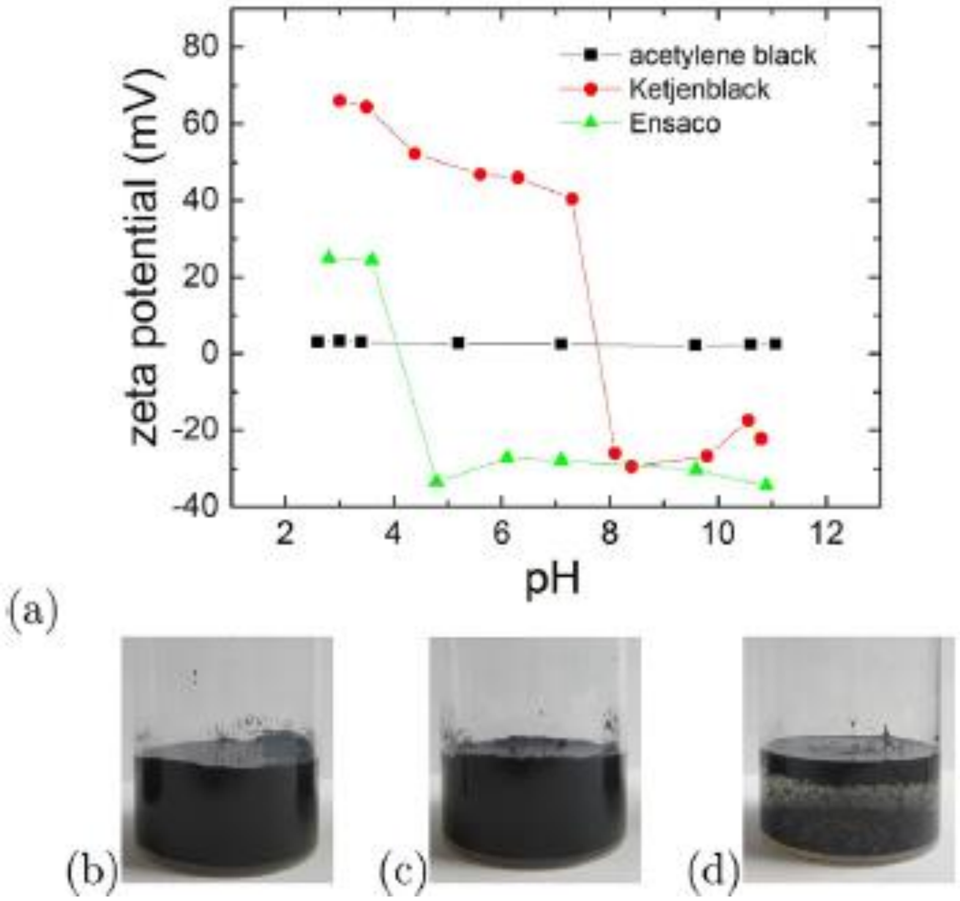

Figure 17: a) Zeta potential over pH diagram for three investigated carbon blacks (1 wt% CB) in aqueous solution without addition of an emulsifier. Photos are included showing the respective suspensions of (b) Ensaco pH=7.5 (c) Ketjenblack pH=9 and (d) acetylene black pH=7.5 (Parant et al., 2017).

2.2.5. Conductivity Measurement Techniques

This chapter functions as a bridge between theory and practise as it relates measuring the electronic and ionic resistance to common measurement techniques used in the lab. Electrochemical impedance spectroscopy ("EIS") is often used for retrieving ionic resistance and electronic resistance, whereas additionally the overall conductivity for simple systems can be measured using a conductivity meter. Besides these two options, electronic resistance is often measured via a galvanostatic conductivity measurement. This chapters tackles these techniques one by one, diving into the theory behind them as well as the respective use cases.

In an EIS measurement the impedance is measured by applying a potential with an excitation amplitude ("V_{rms}") over a variety of frequencies, ranging from MHz to mHz, while measuring the current through the cell. A small excitation amplitude is applied so that the response can be assumed to be pseudo-linear over a small portion of the cell, highly simplifying the impedance analysis ("Basics of electrochemical impedance spectroscopy," 2020). The fundamental theory behind this is the linear system theory, requiring that the response of the system must be linear, stable, casual and finite, which is often the case for excitation values around 10 mV (MacDonald, 2006). The resulting bode plots of the impedance ("Z") and phase shift ("Φ") in the frequency domain are often translated into a Nyquist plot in the complex domain. An analysis of the Nyquist plot gives information on the electrochemical behaviour. This is additionally reinforced by fitting of the impedance data, through which an equivalent circuit consisting of capacitors and resistors in series and parallel can be realised. The advantage of this technique is that it offers not only information on ionic and electronic resistance, but also offers information with respect to charge-transfer resistance, ion transfer limitations and the overall internal resistance (Mei, Munteshari, Lau, Dunn, & Pilon, 2018). The disadvantage is that this technique is time consuming and is often difficult to interpret due to non-ideal behaviour.

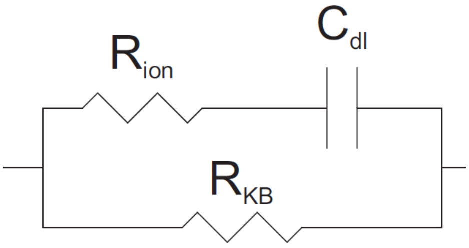

Figure 18: Proposed representation of an equivalent circuit for a semi-solid suspension (Narayanan, 2020).

When applying EIS to a SSE suspension, it is proposed to simplify the system to an equivalent circuit consisting of an ionic resistor ("R_{ion}") and an ionic double layer capacitance ("C_{dl}"), both in parallel to the electronic resistance of the carbon black network ("R_{kb}") (Narayanan, 2020). This is illustrated in Figure 18. The correlation between R_{ion}, R_{KB} and EIS data can then be most effectively retrieved from the intersection of a Nyquist plot with the real impedance axis ("$R_{0\text{-}high}$") in the high frequency domain, often between 10kHz and 1MHz (Dai, Jiang, & Wei, 2018; Mei et al., 2018). At high frequencies the capacitor acts like a conductive wire, meaning that a measured real impedance is the result of two resistors in parallel when considering the proposed equivalent circuit. The relation between $R_{0\text{-}high}$, R_{ion} and R_{kb} can be described as follows:

$$\mathrm{R_{0-high}} = \frac{\mathrm{R_{ion}\,R_{kb}}}{\mathrm{R_{ion} + R_{kb}}} \tag{13}$$

At very low frequencies EIS data can be related to electronic resistance (Ozoemena & Kebede, 2016). At low frequencies the double layer capacitance will result in an infinite resistance. Recalling the equivalent circuit, this means that a real impedance at low frequency is the result of solely the contribution of R_{kb}. In ideal EIS data this would be represented as the intersection of the Nyquist plot with the real impedance axis ("$R_{0\text{-}low}$") in the low frequency domain:

$$\mathrm{R_{0-low}} = \mathrm{R_{kb}} \tag{14}$$

A fast and more simplistic, but limited method, to measure conductivity is by using a conductivity meter. This device has electrodes with a fixed area and a set distance between them. Calibration of such devices with respect to temperature and a potassium chloride ("KCl") solution are required before use. Even though this method is fast and easy, a substantial downside of this method is that it cannot differentiate between ionic and electronic conductivity in a SSE suspension, and thus provides a rough representation and may oversimplify the system.

The electronic resistance of a suspension can finally also be measured using a galvanostatic conductivity measurement. During this test a fixed direct current is applied to the suspension of interest and the potential is measured. It is advised to hold this current for a period of at least 5-10 minutes until a stable potential is obtained (Ozoemena & Kebede, 2016). That potential can then be related to the electronic resistance via Ohm's law:

$$\mathrm{R_{kb}} = \frac{\mathrm{U}}{\mathrm{I}} \tag{15}$$

The advantage of this measurement is that it is faster and easier than EIS. The disadvantage is that it may not always be applied, as Eq. 15 is only valid once the potential has stabilised. If not, the observed behaviour is not that of a pure resistor and Ohm's law does not account.

2.2.6. Colloidal Stability

Creating a stable colloidal suspension is a key principle in acquiring a well-functioning SSE suspension, as it aims to enable and maintain sufficient contact between the electroactive particles and the electronically conductive particles throughout the suspension, while not selling short to ionic conductivity and flowability of the suspension. This section explains the most important forces attributed to colloidal stability of a SSE suspension. First it will explain the DLVO theory (the interaction between the electrostatic forces of repulsion and the attractive van der Waals forces), followed by the gravitational forces. From this it follows that a stable colloidal suspension is most effectively created by increasing the viscosity of the suspension and by minimization of the dispersed particle size. After this, this section dives into the addition of jammed soft particles to enhance colloidal stability. Addition of enough of such material will induce a jamming transition, by which the suspension will behave like a solid until a specific stress (the yield stress) is applied, after which it has liquid properties.

In general colloidal particles encounter each other through sedimentation, Brownian movement (random agitation of molecules due to heat) and convection (Leslie, 1989). Additionally, with respect to a SSRFB, they also encounter each other through flow operation. Note that the forces in conjunction to the first three are orders of magnitudes lower compared to the forces as a result of flow operation. Whether these "collisions" are permanent and result in flocculation, coagulation or coalescence primarily depends on both the attractive and repulsive forces of interaction between the particles. The DLVO theory explains that the most important type of forces between colloidal particles in aqueous medium are the electrostatic forces of repulsion and the attractive van der Waals forces (Leslie, 1989). Figure 19 gives graphical representation of how these interactions are indeed significant at the small distances for which one would expect coagulation or flocculation to occur (Adamczyk, 2013).

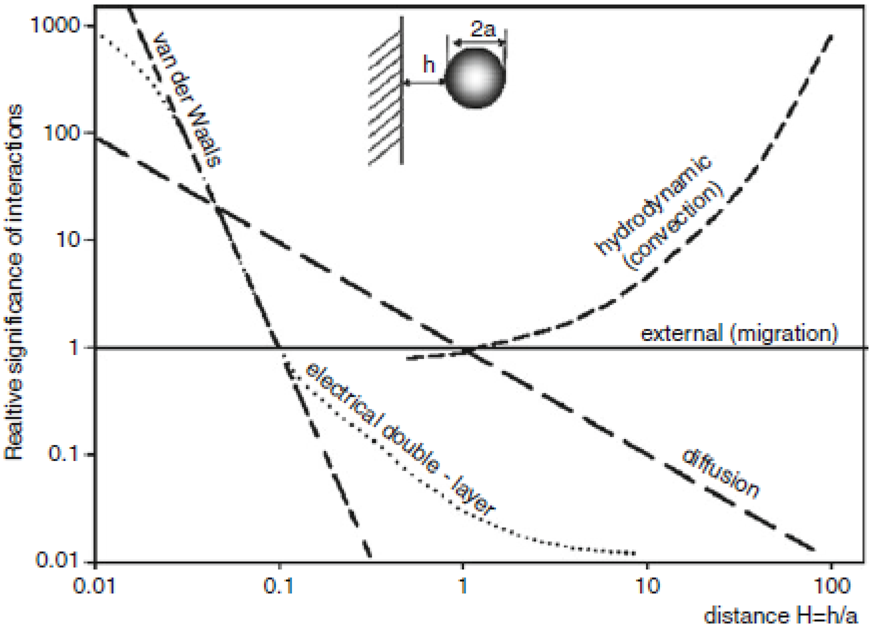

Figure 19: The relative significance of interactions with respect to the distance between particles (Adamczyk, 2013).

Without any repulsive forces, the attractive van der Waals forces would inevitably lead to coagulation and possibly sedimentation. However, in practise, repulsive forces at the electrical double layer overcome this. DLVO theory states that addition of these two forces results in the resulting net force at a certain distance between colloidal particles. This resulting net force is an indicator for colloid stability. Figure 20 shows the interactive energy between colloidal particles. It shows a net primary minimum, indicating strong coagulation if the particles come within this distance from each other. Nevertheless, a net primary repulsive maximum acts as a boundary that prevents the colloidal particles coming within close vicinity (Tadros, 2014). Depending on the type of particles and electrolyte composition there may even exist a net secondary stable minimum that can result in weaker flocculation. Even though two colloidal particles might not have enough kinetic energy to reach the primary minimum, they might have enough to reach a stable secondary minimum. A weaker bond like this is then also easier to break.

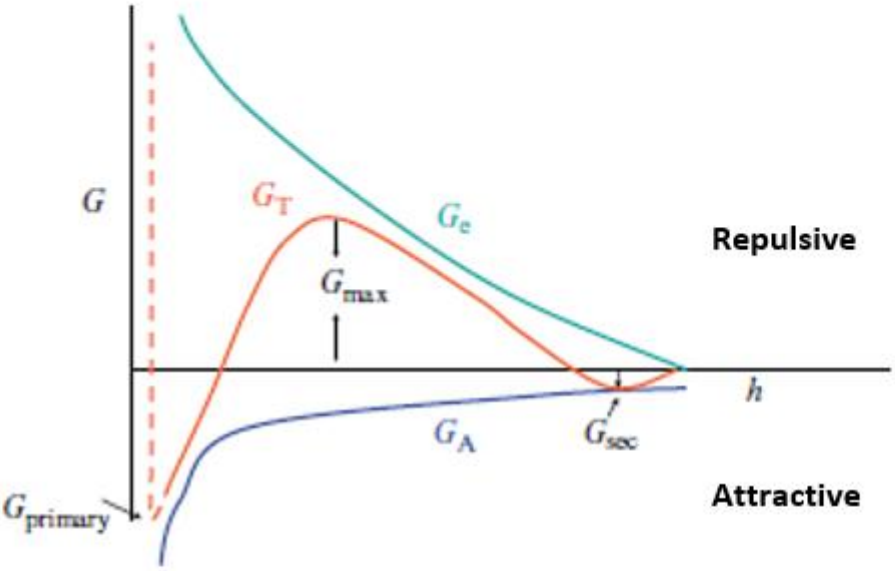

Figure 20: Attractive Van der Waals forces, repulsive electrostatic forces and the net total force as a function of the distance between two particles (Tadros, 2014).

The net electrostatic surface charge thus largely determines the tendency for coagulation and flocculation and while surface charge is difficult to measure, it is generally accepted to use the zeta potential as a measure for colloid stability (Pate & Safier, 2016). The zeta potential is defined as the potential in the electrical double layer at the slipping plane (or shear plane), which is the plane that separates the mobile fluid from the fluid that interacts with the particle surface. Figure 21 gives an general representation of the location of the surface charge and zeta potential with respect to the particle. In general, in aqueous media the shear layer is about one hydrated ion diameter away from the particle surface. Overall, the larger the magnitude of the zeta potential, the greater the repulsive force and the smaller the chance of coagulation and flocculation (Greenwood & Kendall, 1999). Table 1 shows a general overview of the relationship between the zeta potential and colloidal stability, concluding that good colloidal stability is obtained at zeta potentials greater than |40mV|.

Table 1: Colloidal stability ranges for zeta potential (Pate & Safier, 2016).

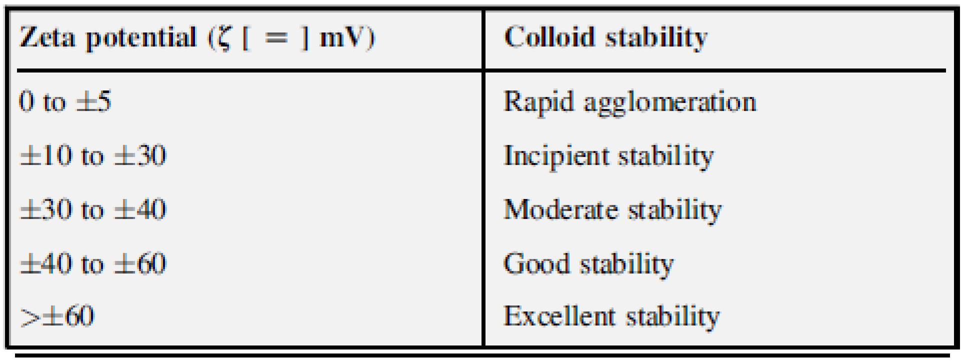

Zeta potential (ζ [=] mV)	Colloid stability
0 to ±5	Rapid agglomeration
±10 to ±30	Incipient stability
±30 to ±40	Moderate stability
±40 to ±60	Good stability
>±60	Excellent stability

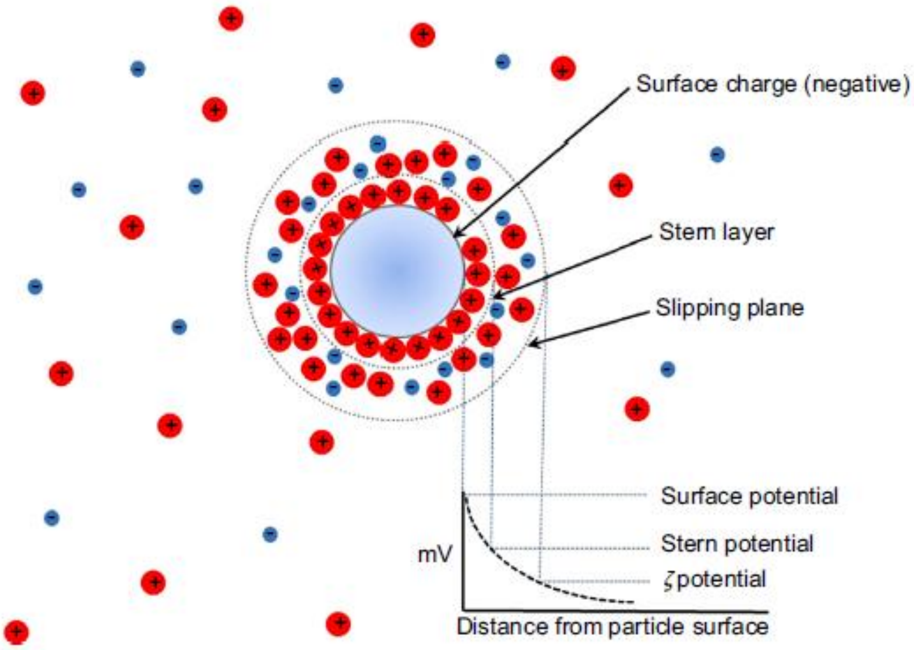

Figure 21: Representation of zeta potential (Pate & Safier, 2016).

Measuring the zeta potential (“ζ”) in suspensions is usually done using electrophoresis or acoustophoresis. The former being a well-established technique and the latter being more applicable for industrial applications and volumes (Greenwood & Kendall, 2000). Electrophoresis uses an alternating electric field (“*E*”) to move particles. The velocity (“*v*”) with which the particles move is then related to the mobility via $\mu = \frac{v}{E}$. Depending on particle sizes and ionic strength of the solution, the mobility can then be related to the zeta potential using the von Smoluchovski (Eq. 17) or Huckel equation (Eq. 18) (Greenwood & Kendall, 2000). Whether to choose the Hücker or the von Smoluchivski equation depends on the Debye-Hückel parameter κ for N ionic mobile species, which is inversely related to the thickness of the double layer and is defined as:

$$\kappa = \sqrt{\frac{1}{\varepsilon_0 \varepsilon_r k_b T} \sum_{i=1}^{N} z_i^2 e^2 n_i^{\infty}} \tag{16}$$

Where ε_0 is permittivity of a vacuum, ε_r is the relative permittivity, k_b is the Boltzmanns constant, T is the absolute temperature, z_i is the valence, e is the elementary electric charge and n_i^{∞} is the bulk concentration (Ohshima, 2013).

As illustrated in Figure 22, when considering a particle with radius a, if a spherical particle has a thin double layer with respect to the particle size ($\kappa a \gg 1$), one uses the Smoluchovski Eq. 17. If the spherical particle has a thick double layer ($\kappa a \ll 1$) the situation is most carefully represented by the Hückel Eq. 18 (Ohshima, 2013). By comparing Eqs. 17 and 18, zeta potential maximization is favoured by a thick double layer. It is thus imperative to abide by $\kappa a \ll 1$. For this reason particle size and Debye-Hückel have to be minimised. The latter is achieved by increasing viscosity, temperature or by decreasing the bulk electrolyte concentration.

$$\mu = \frac{\varepsilon_r \varepsilon_0}{\eta} \zeta \tag{17}$$

$$\mu = \frac{2\varepsilon_r \varepsilon_0}{3\eta} \zeta \tag{18}$$

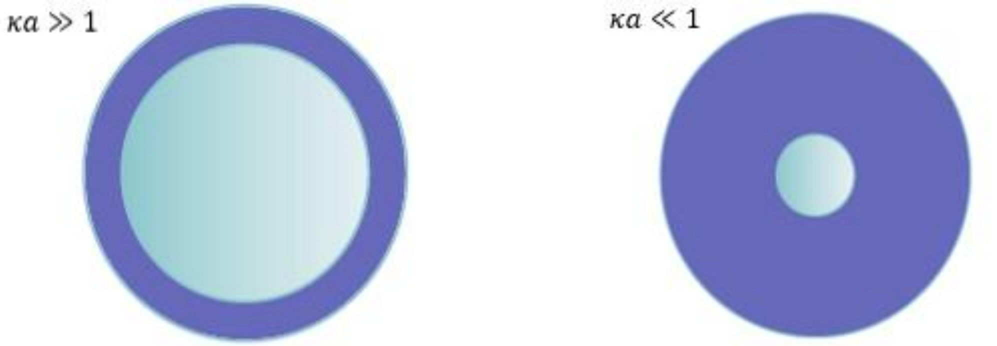

Figure 22: Charged particles with a thin (left) and thick (right) double layer (Ohshima, 2013).

Whereas the attractive van der Waals and repulsive electrostatic forces between molecules relate to the tendency for flocculation and coagulation, gravitational forces are the mechanism that account for sedimentation and flotation. The rate (“v_{sed}”) at which this occurs for a solid spherical particle in a fluid is given by Stokes' law:

$$v_{sed} = \frac{2}{9} * \frac{ga^2(\rho_1 - \rho_2)}{\eta} \tag{19}$$

Where g is the force of gravity, a is the respective particle diameter, ρ_1 is the density of the solid particles, ρ_2 is the density of the dispersion medium and η is the viscosity of the fluid. Depending on the difference in density of the dispersed solid particles and the dispersion medium the direction of movement is either downwards (sedimentation) or upwards (flotation). From Eq. 19 follows that the rate of sedimentation is reduced by decreasing the dispersed particle size, increasing the viscosity of the dispersion medium or by decreasing the difference in density between the dispersed phase and dispersion medium.

Stokes’ law (Eq. 19) also shows that minimization of coagulation and flocculation effectively helps minimizing the particle size and thereby reducing rate of sedimentation. This suggests a self-reinforcing correlation between coagulation/flocculation and sedimentation/flotation: The more stable a suspension is, the more stable it remains. It must furthermore be noted that when considering electrochemical behaviour, flocculation, and even worse, coalescence, reduces the overall effective surface area and contact points available for the electron and ion transfer into the material and increases the internal resistance as charged particles have to travel deeper into the material.

Now that it has been made clear that an increase in viscosity leads to an increase in colloidal stability of a SSE suspension, the addition of jammed soft particles it touched upon. Addition of such a material to a liquid will change the behaviour from liquid-like to solid-like once a critical concentration is surpassed (Dinkgreve, 2019). This critical point is often referred to as the point where jamming transition occurs. At this point the soft particles are compressed against each other such that the viscosity has changed (Figure 23).

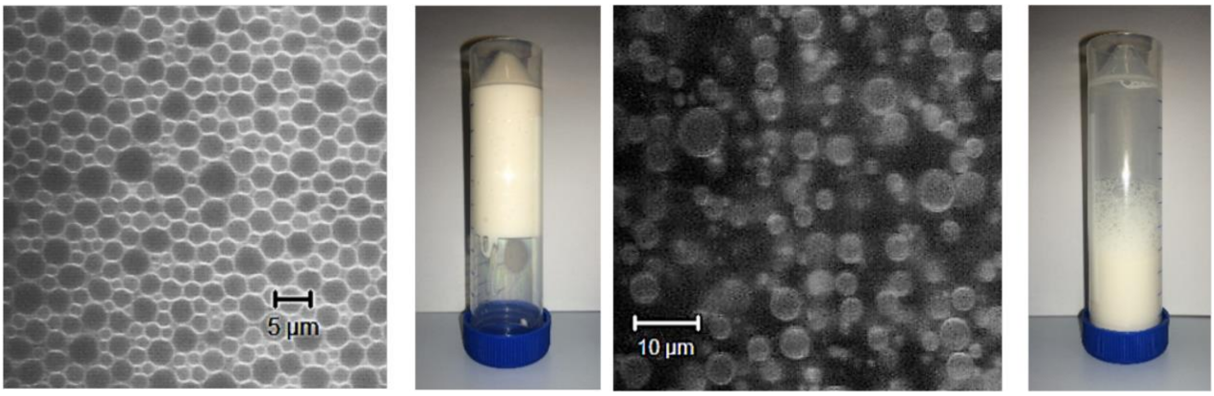

Figure 23: Pictures of emulsion droplets (silicone oil-in-water) – after exceeding the jamming transition (left), before exceeding the jamming transition (right) (Dinkgreve, 2019).

If the appliance of a high enough stress (equal to the yield stress) lowers the viscosity, such a fluid is also known as a yield-stress fluid, with non-Newtonian behaviour known as shear-thinning (Dinkgreve, 2019) (Figure 24). This is advantageous for flow application, as a SSE suspension shows starts showing more liquid behaviour when pumping force is applied to it. Alginates and polyacrylic acids are often used as such materials (Dinkgreve, 2019; Narayanan, 2020; Parant et al., 2017).

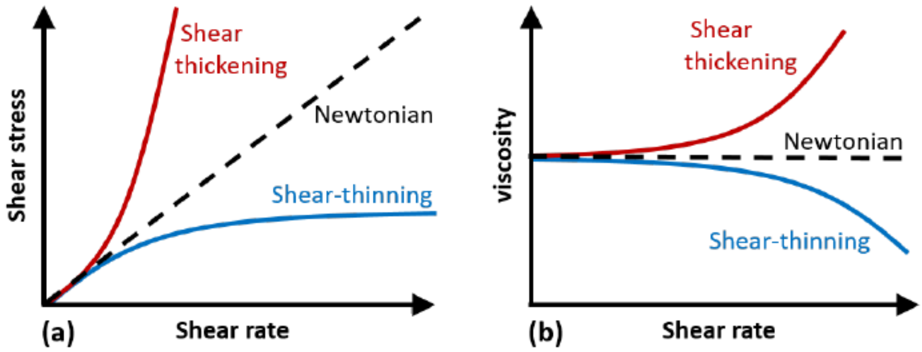

Figure 24: Characteristics of a Newtonian, shear-thinning and shear-thickening fluid (Dinkgreve, 2019).

In conclusion, the main focus for creating a stable colloidal suspension over a longer period of time is by maximizing the zeta potential and by minimizing the rate of sedimentation. This is most effectively realised by increasing the viscosity and using small particles (<1 µm). The increase in viscosity is often realised through the addition of jammed soft particles. Furthermore, minimization of the electrolyte concentration and having low valency of the electrolyte contribute too, although in smaller significance (Tadros, 2014).

2.2.7. Chemical Stability

In this final chapter of the literature study the chemical stability of the active iron and manganese hydroxide species are considered in a strong alkaline environment ($14 < pH < 15$) and a potential window of $-0.56\ V < E < +0.15\ V$, as proposed by Eqs. 2 and 3.

When considering the Pourbaix diagram of iron in water (Appendix D) it is noted that both $Fe(OH)_2$ and $Fe(OH)_3$ exist in an alkaline environment of $14 < pH < 15$ at the proposed potential vs SHE with a stability domain of respectively $-0.56\ V > E^0_{cell} > -0.62\ V$ (Pourbaix et al., 1997). It must furthermore be noted that in this area of pH and potential an ionic species is mentioned, namely the $HFeO_2^-$ ion. When considering ferrous hydroxide $Fe(OH)_2$ in the alkaline environment, literature also mentions the existence of anionic complexes such as $Fe(OH)_3^-(aq)$ and $Fe(OH)_4^{2-}(aq)$ (Beverskog, 1996).

Next to this, research by Beverskog states that in alkaline conditions $Fe(OH)_2$ is unstable at high temperature. For example, decomposition into elementary iron and magnetite (Fe_3O_4) occurs from T > 85°C, with ± 20°C uncertainty in the temperature (Eq. 20) (Beverskog, 1996). This is further reinforced by practical research from Linnenbom that suggests that $Fe(OH)_2$ does not exist at T = 60°C in alkaline conditions (Linnenbom, 1958).

$$4\mathrm{Fe(OH)_2(s)} \rightarrow \mathrm{Fe_3O_4(s)} + \mathrm{Fe(s)} + 4\mathrm{H_2O(l)} \qquad (20)$$

Schikorr proposes that even at room temperature slowly but surely a reaction mechanism takes place, known as the “Schikorr reaction” (Eq. 21). This is an electrochemically reaction where $Fe(OH)_2$ is oxidised into magnetite, water and hydrogen gas, whereby the reaction speed increases with increasing temperature (Beverskog, 1996; Linnenbom, 1958).

$$3\mathrm{Fe(OH)_2(s)} \rightarrow \mathrm{Fe_3O_4(s)} + \mathrm{H_2(g)} + 2\mathrm{H_2O(l)} \qquad (21)$$

The above suggests that $Fe(OH)_2$ is a chemically sensitive compound. Yet, at the same time, experiments executed by Linnenbom together with earlier studies executed by Evans and Wanklyn and Shipko and Douglas, conclude that there is no concrete evidence that the Schikorr reaction spontaneously takes place at room temperature without the presence of specific catalysts (Linnenbom, 1958).

Manganese can form oxides or hydroxides in the +2, +3 and +4 oxidation state that all have low solubility (Hem, 1963). Moreover, the higher the pH, the less soluble the manganese (Hem, 1963). Besides the influence of pH on solubility, Hem notes that in aerated water $Mn(OH)_2$ oxidises fast to become Mn_2O_3, and that anaerobic environments are needed to prevent oxidation of $Mn(OH)_2$ with air. This is further reinforced by the proposed method for the synthesis of $Mn(OH)_2$, which was prepared in an argon gas atmosphere (Anandan, Gnana Sundara Raj, Lee, & Wu, 2013). After consulting the Pourbaix diagram of manganese in water (Appendix D), it was observed that besides the existence of $Mn(OH)_2$ and $Mn(OH)_3$ at strong alkaline conditions ($14 < pH < 15$), an ionic species of $HMnO_2^-$ is suggested.

The mentioning of more species than simply the $Fe(OH)_2$, $Fe(OH)_3$, $Mn(OH)_2$ and $Mn(OH)_3$, as well as their instabilities are a signal of a more complex electrochemical system than proposed by Eq. 1 and suggest that their stability (especially in aerated environments) might be low.

3. Experimental

This chapter presents the methodology for obtaining the required data needed to validate whether it is possible to make a battery out of the proposed iron- and manganese hydroxide active materials using SSE suspensions and a cheap microfiltration membrane. Following from the literature study, the prominent design parameters for the composition of SSE suspensions are the electronic conductivity, ionic conductivity, colloidal stability and viscosity. Because of the high amount of design choices and the novelty of the design, the strategy applied during the experimental section of this thesis is one of divergence-convergence. During the divergence phase, many rough experiments were done by using basic measurements techniques and obtaining information qualitatively in order to effectively find trends and limitations (e.g. by doing simple measurements using a conductivity meter and by making observations with respect to colloidal stability and viscosity). After a framework was found of which it was believed to be promising, the strategy was to then to converge to more specific setups and measurement techniques that were more time consuming and complicated, such as EIS, charge/discharge testing and galvanostatic conductivity testing. These were designed such that they answer the main and sub-research questions of this thesis. The main quantitative measurement techniques used were galvanostatic (dis)charging, potentiostatic (dis)charging, EIS and OCV measurements. Information regarding colloidal stability and viscosity were obtained qualitatively.

The build-up of this chapter is as follows. First, in Chapter 3.1 the chemicals and cell equipment are outlined, giving a high-level impression of the used consumables and the materials for the experimental setups. Second, in Chapter 3.2 details are shared about the tools used for doing measurements, doing synthesises and for the preparation of the suspensions. Third, as $Mn(OH)_2$ could not be acquired in time externally, Chapter 3.3 explains the methodology of the synthesis of $Mn(OH)_2$ in the lab. Fourth, in Chapter 3.4 the methodology for the preparation of suspensions is explained, together with the nomenclature to differentiate between suspensions. Fifth, in Chapter 3.5 the procedure for the preparation of salt bridges is shared, which were used to isolate and analyse individual SSE suspensions. Finally, Chapter 3.6 finalises this chapter by describing experimental setups and procedures that have been used.

3.1. Chemicals and Cell Equipment

In this chapter the used chemicals and cell equipment are shared. The first paragraph below explains which consumables were used, specifying some of their main properties and origin. In the second paragraph the relevant cell equipment and their key characteristics are outlined.

In all suspensions, KOH solutions were used to create ionic conductivity and Ketjenblack EC600JD (“kb”) from Akzonobel was used to bring electronic conductivity. The literature research in Chapter 2.2.3, 2.2.4 and 2.2.6 had already justified that KB is a popular choice in aqueous environments due to its high conductivity, moderately low percolation threshold and moderate colloidal stability and that KOH is attractive because it is a strong base with a valency of one and with a lower viscosity than NaOH. Different molarities KOH solutions were made by dissolving >85% pure KOH pellets, acquired from Sigma-Aldrich, in demi-water. Alginic acid 500 (“ALG”), polyvinylpyrrolidone (“PVP”) and polyacrylic acid (average Mv 450,000) (“PAA”), all obtained from Alfa Aesar, were separately used to test how they enhanced the colloidal stability of the suspensions. The SSE suspensions containing iron(III)oxyhydroxide (“FeOOH”) were prepared by making use of >99% pure α-FeOOH powder, acquired from Alfa Aesar. FeOOH was used as similar alternative to $Fe(OH)_3$. Next to this, the active material in the other SSE suspension was $Mn(OH)_2$, which was synthesised in the lab. For this synthesis, KOH solutions and >99% pure manganese acetate (“$Mn(CH_2CO_2)_2$”) from Sigma-Aldrich were used (further elaborated in Chapter 3.4). Furthermore, in order to analyse the SSE suspensions separately, two more electrodes in electrolyte and a salt bridge were prepared. On the one hand this was a zinc electrode in 1M zinc nitrate solution (“$Zn(NO_3)_2$”), where the >97% pure $Zn(NO_3)_2$ was acquired from Sigma-Aldrich. On the other hand this was a copper electrode in 1.25M copper nitrate solution (“$Cu(NO_3)_2$”), by which the >99% pure $Cu(NO_3)_2$ also came from Sigma-Aldrich. Ionic contact of these electrodes and the electrode suspensions were brought upon by making use of a salt bridge. The chemicals used for this salt bridge were 99.5% pure sodium chloride (“NaCl”) and >98% pure ammonium nitrate (“NH_4NO_3”), both acquired from Sigma-Aldrich. Additionally, ultrapure Agar provided by USB corporation (USA) was used as hardener.

The relevant cell equipment consisted of the electrode suspension and electrolyte housing, the current collectors, the membranes, the membrane housing, the hinge clamps and the salt bridge housing. For the electrode suspension and electrolyte housing, glass elbow tubes (17 mm inner diameter) were used for the electrode suspensions that were separated by membrane(s) (Chapter 3.6.1 until 3.6.3) and 50 ml plastic jars were used for electrodes separated by a salt bridge (Chapter 3.6.4). Initially, 100 µm thin platinum current collectors from Vos Instrumenten were used for electron transport from the suspensions (area of 0.5 cm^2), however these were too fragile considering the relatively high viscosity of the suspensions. Therefore, all results in this thesis originate from tests done using stiff glassy carbon current collectors obtained from HTW Hochtemperatur-Werkstoffe GmbH. The conductive area of the glassy carbon current collectors was designed to be 0.2 cm^2. With respect to membranes three types were analysed: The Whatman GFA, filter paper and Cellgard 2400 membrane. The pore sizes were respectively microporous, microporous and nano-porous. The membrane housing consisted of a main plastic O-ring (17 mm outer diameter) surrounded by a rubber gasket, that fit exactly between two glass elbow tubes. Inside this plastic O-ring, the membrane was clamped between two smaller plastic O-rings that had an outer diameter equal to the inner diameter of the main O-ring. This was done in such a way that the membrane area was constant at 1 cm^2 (Figure 25). The two glass elbows and the membrane housing were then tightly held in place using a hinge clamp. In the cell setup where a salt bridge was used, a 20 ml U-shaped glass tube was used as salt bridge housing in between two 50 ml plastic jars containing the electrodes and electrolyte. Last, in order to find the half-cell potential of the $Mn(OH)_2$ SSE suspension and the FeOOH SSE suspension, a silver/silver chloride (“Ag/AgCl”) reference electrode was introduced to the cell setup as an additional tool. The electrolyte inside this reference electrode was 3M KCl and was brought in contact with the SSE suspensions of interest (both the $Mn(OH)_2$ as well as the FeOOH SSE suspension).

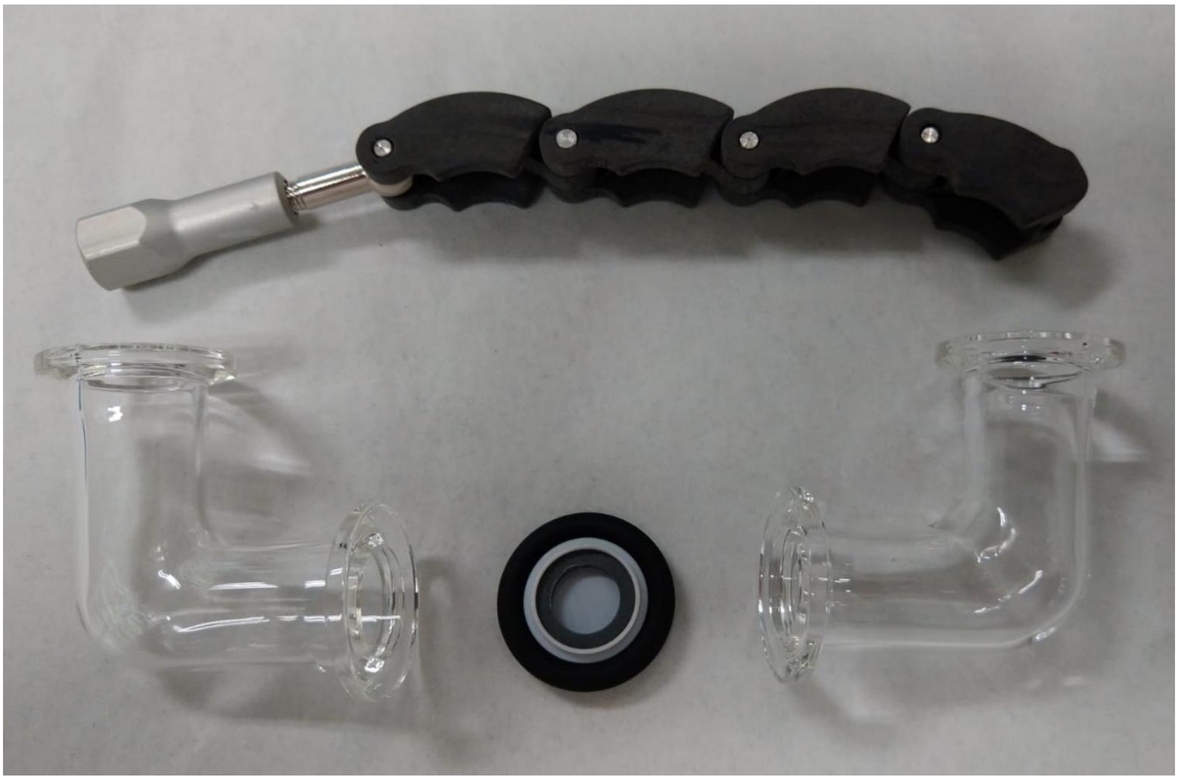

Figure 25: Overview of materials for setup 3 (Chapter 3.6.3) – glass elbow tubes, full membrane housing, a Cellgard membrane and a hinge clamp.

3.2. Measuring and Preparation Equipment

In this chapter the various equipment that was used for the preparation of suspensions, synthesis of chemical compounds and the execution of measurements are discussed. In the first paragraph the most important measurement equipment is shared. The second paragraph provides the tools used for preparation and synthesis of materials and suspensions. An overview the most important tools is found in Figure 26.

All charge/discharge and impedance spectroscopy procedures were executed using the MetrOhm Autolab PGSTAT30 ("Autolab") combined with Nova software. The results from both galvanostatic and potentiostatic charge/discharge test procedures were used to investigate the electrochemical operation of the SSE suspensions in the experimental setups as well as to investigate electronic conductivity of suspensions. Details about the usage of the Autolab with respect to the four different setups are described in Chapter 3.6. Next to the Autolab, the Greisinger GMH 3400 series conductivity meter was used for simpler measurements, such as electrical conductivity measurements of KB in water in order to find the respective percolation threshold in that environment. Before use it was calibrated in ice water for allignment of temperature and in a 1M KCl solution for allignment of conductivity. An advantage of this meter over the Autolab was that it measured conductivity fast and over a fixed distance. However, an important limitation was that it only measured conductivity up to 200 mS/cm and could not distinguish between ionic and electronic conductivity. Since a suspension including KB and KOH can be seen as a parallel circuit, any suspension holding a KOH solution with a molarity >0.5 M surpassed this value, rendering the conductivity meter useless in such environments (Gilliam et al., 2007). This explains amongst others why the slower Autolab was used for conductivity measurements of the SSE suspensions. For weighing purposes, measurements were done using a 100 µg accurate Sartorius lab weighing scale. Finally, the Mettler Toledo FG2 FiveGo pH meter was used for pH measurements after dual-step calibration in a pH-7 and pH-10 solution. A limitation of this meter was that it measured until pH-14, after which it went out of bounds (theoretically the case in a > 1M KOH solution). However, the knowledge that a suspension had a pH > 14 gave adequate insight with respect to for example Pourbaix diagrams.

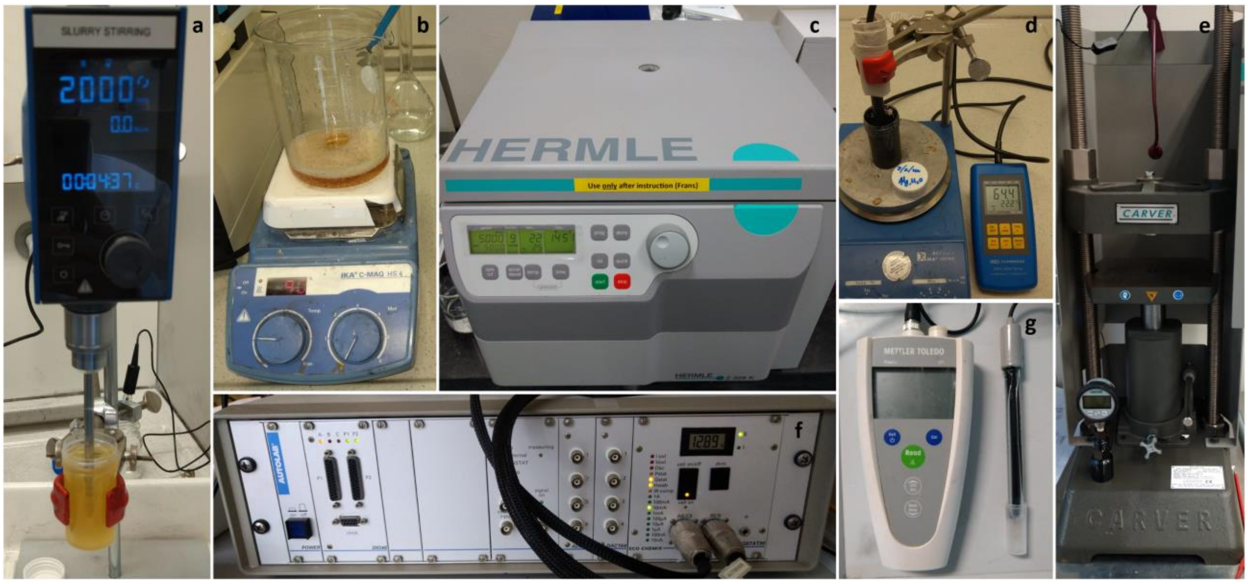

Figure 26: Overview of measuring and preparation equipment – a) ultraturrax mixer, b) hotplate stirrer, c) centrifuge, d) conductivity meter, e) lab press , f) Autolab and g) pH meter.

For the homogenous preparation of the suspensions an IKA Microstar 7.5 overhead ultraturrax mixer was used. The maximum stirring rate this machine had was 2000 rpm. Next, homogenous heating and mixing was done using an IKA C-MAG HS-4 hotplate stirrer, which was able to heat a solution from 0 °C up to 450 °C using 5 degrees interval steps (maximum temperatures of 95°C were used). In addition, the Hermle Z326K centrifuge was used to accelerate sedimentation during the synthesis of $Mn(OH)_2$. The maximum centrifugal rate was 5000 rpm. Moreover, an argon gas blanket was applied as much as possible during the synthesis of $Mn(OH)_2$ and measurements using $Mn(OH)_2$ to minimize exposure to oxygen. Finally, any pressing of solid electrodes for comparison to SSE electrodes was done using a Carver lab press (Appendix E).

3.3. Methodology for the Synthesis of $Mn(OH)_2$

In this chapter the synthesis of $Mn(OH)_2$ is explained, because as opposed to the FeOOH powder, it was not available commercially within reasonable time. During this process it became very clear how sensitive $Mn(OH)_2$ was to oxidation by the quick darkening of the wet white $Mn(OH)_2$ samples when brought in contact with air. Without the use of an anaerobic environment it was impossible to synthesize dry $Mn(OH)_2$ without oxidation prevailing. For this reason $Mn(OH)_2$ was synthesized and stored in its saturated form and also mixed into the respective suspension while being saturated.

For the synthesis of a batch of $Mn(OH)_2$, 20 grams of $Mn(CH_2CO_2)_2$ was dissolved in 50 ml of demi-water and slowly heated to 90°C to minimize oxygen content in the solution. Next, a surplus of 30 grams of KOH pellets was dissolved in 50 ml demi-water and also slowly heated to 90°C for oxygen minimization. Subsequently, the entire KOH solution was transferred into the $Mn(CH_2CO_2)_2$ solution and properly stirred with a magnetic stirrer. The mixture immediately turned cloudy white, indicating the existence of $Mn(OH)_2$. During this process argon was slowly blown into the beaker onto the mixture to function as a blanket for protection against oxidation. The surplus of KOH was enough to fully react with double the amount of $Mn(CH_2CO_2)_2$ and ensured that all Mn^{2+} reacted into $Mn(OH)_2$. The white mixture was then gently, but quickly, divided over four special 50 ml twist cap containers and put in a Hermle Z326K centrifuge and centrifuged at 5000 rpm for 5 minutes. The result was a white, dense, $Mn(OH)_2$ precipitate at the bottom of the containers covered by a transparent layer of supernatant solution (Figure 27c). These containers were subsequently stored at room temperature. Once the $Mn(OH)_2$ was required, the supernatant solution in the container was decanted and 90°C demi-water was added. Everything was then properly stirred to wash off any residual acetate and potassium ions. It was then centrifuged at 5000 rpm for 5 minutes again. After the supernatant was decanted this process was repeated once more but then while using a 5M KOH solution for washing. The supernatant was then decanted for a final time, after which the predominantly white residual $Mn(OH)_2$ was considered ready for use. Note that the $Mn(OH)_2$ was still wet with 5M KOH solution and that integration into the suspension had to happen quickly to minimize exposure to oxygen. Note furthermore, that for the weight conversion of wet to dry weight $Mn(OH)_2$ a conversion factor of 1.5 was used, based on an experiment that examined the weight difference of dry and wet FeOOH powder. A wet sample of $Mn(OH)_2$ of 1.5 grams, was thus approximated to consist of 1.0 grams of dry $Mn(OH)_2$ and 0.5 grams 5M KOH solution.

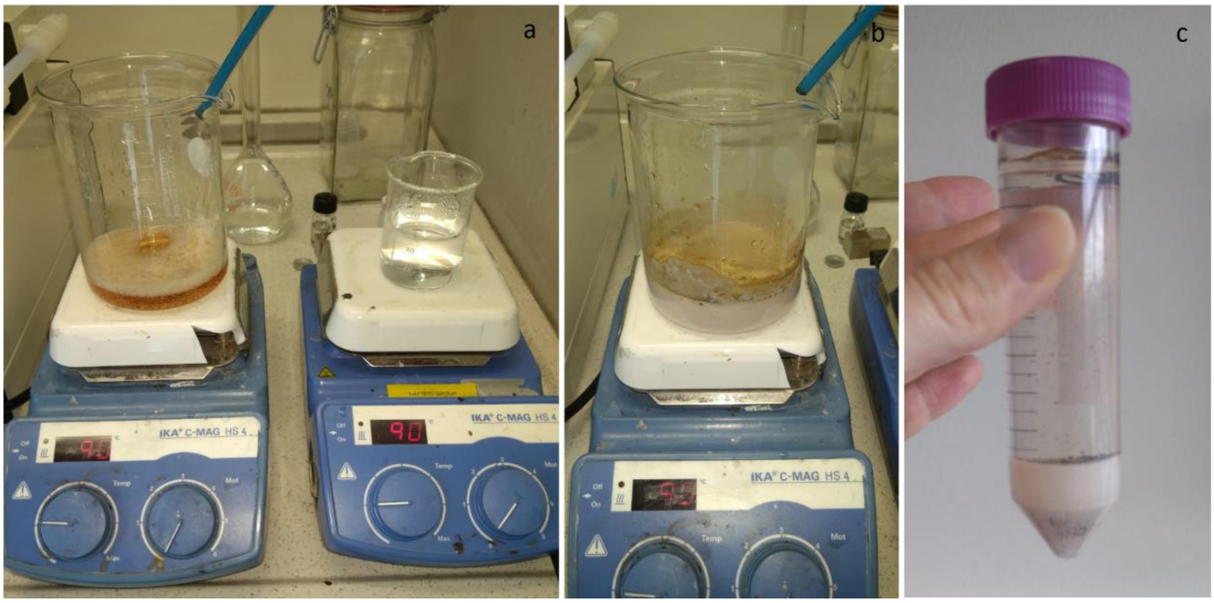

Figure 27: Synthesis of $Mn(OH)_2$ – a) $Mn(CH_2CO_2)_2$ and KOH solution at 90°C, b) white cloudy mixture of $Mn(OH)_2$ after synthesis (slow darkening on the surface happening despite Argon feed), c) storage of white $Mn(OH)_2$ under wet conditions.

3.4. Preparation and Identification of SSE Suspensions

Dozens of suspensions were prepared to gain information on colloidal stability, viscosity, ionic conductivity, electronic conductivity and their electrochemical behaviour, in order to effectively answer the main and sub-research questions of this thesis. This chapter first explains the nomenclature for the suspensions. After this, the method for the preparation of a FeOOH SSE suspension is described, followed by the method for the preparation of a $Mn(OH)_2$ SSE suspension, as this deviates slightly from the FeOOH suspension.

3.4.1. SSE Suspension Nomenclature

In order to succinctly differentiate between the dozens of suspensions with different compositions a uniform nomenclature was maintained. Besides some initial suspensions, all samples were prepared to have a total weight of 20 grams. Within these 20 grams, the prepared suspensions ranged from having different wt% kb, different wt% ALG or PAA, different molarities and amounts of KOH solution and different amounts of either FeOOH or $Mn(OH)_2$ as electroactive material. With respect to the active material, either 50 mmol active material (22.2 wt%), 10 mmol (4.4 wt%) or no no active material was used. An example of a suspension and its nomenclature is the 8/2-ALG/22.2-Fe/67.8-5M SSE suspension. The nomenclature for this suspension is explained hereunder and can be applied to every suspension in this thesis:

- The 8 stands for 8 wt% kb, thus a total of 1.6 grams in the sample.
- The 2-ALG stands for 2 wt% Alginate, thus a total of 0.4 grams in the sample. In case PAA was used, the PAA notation is given.
- The 22.2-Fe stands for 22.2 wt% FeOOH powder. This means a total of 4.44 grams FeOOH was added to the sample, which equal 50 mmol FeOOH (dry MW: 88.85 grams). Note that this corresponds to *dry* weight and a conversion factor of 1.5 was taken into account when considering the wet $Mn(OH)_2$ as explained in Chapter 3.3 (dry MW: 88.95 grams). In case $Mn(OH)_2$ was used, the Mn notation is given. If no active material was used '-' was given.
- The remainder with respect to the 20 grams was the weight of 5M KOH solution added, in this case 13.56 grams, which was abbreviated with respect to its wt% and molarity as 67.8-5M.

3.4.2. Methodology for the Preparation of SSE Suspensions

The preparation of the FeOOH SSE suspensions were done consistently for the different samples and will now be explained with respect to the 8/2-ALG/22.2-Fe/68-5M SSE suspension. After deciding on the composition and the recipe, first 13.6 grams of prepared 5M KOH solution was added to a little plastic closable jar (50 ml content). Next, 0.4 grams of ALG was added and mixed using an Ultra Turrax mixer for 10 minutes at 2000 rpm. The mixture now turned from transparent to homogenously light yellow. After this, 4.44 grams of dry FeOOH powder was added to the mixture and once again mixed using the Ultra Turrax mixer for 10 minutes at 2000 rpm, after which the colour of the mixture turned homogeneously dark brown. Finally, 1.6 grams of KB was added very slowly while mixing at 500 rpm. This is when the suspension turned viscous. Once all KB was added, the mixture was mixed for another 15 minutes at 2000 rpm to break any agglomerates as much as possible. After mixing, the slightly heated suspension was cooled until it reached room temperature before use. Note that qualitative data with respect to viscosity was always obtained by observing the suspension while mixing it with the Ultra Turrax mixer.

The preparation of $Mn(OH)_2$ SSE suspensions was done using a similar methodology as used for the preparation of the FeOOH suspensions. First the recipe was decided upon in a similar way, while taking into consideration the correction factor of 1.5 to compensate for the $Mn(OH)_2$ being wet. After this, the required amount of KOH solution was added to a 50 ml plastic closable jar (note how somewhat less KOH solution than the recipe showed was added as this stage, since the remainder of the KOH solution incorporated in the wet $Mn(OH)_2$ would be added later). Then the KOH solution and ALG or PAA in accordance with the recipe were mixed for 10 minutes using an Ultra Turrax mixer at 2000 rpm. At the next stage, instead of adding the dry α-FeOOH powder, the corrected amount of ready-to-use, wet $Mn(OH)_2$ was added. This mixture was then mixed again for 10 minutes at 2000 rpm using the Ultra Turrax mixer. The KOH, ALG/PAA and $Mn(OH)_2$ mixture had a light beige colour at this point, indicating the predominant existence of $Mn(OH)_2$. Finally, the required amount of KB was added very slowly while mixing at 500 rpm. Once all KB was added, the mixture was mixed for another 15 minutes at 2000 rpm to break any agglomerates as much as possible. After mixing, the suspension was cooled until it reached room temperature, resulting in a homogeneously light grey to black suspension (depending on the wt% KB and amount of $Mn(OH)_2$).

3.5. Methodology for Salt Bridge Preparation

The procedure used for the preparation of salt bridges is explained in this chapter. Although not highly complicated, the use of a salt bridge did enable to individually analyse SSE suspensions, without the influence of ions from the opposite electrode poisoning the SSE suspensions.

A batch of two salt bridges was prepared by putting 50 ml of demi-water in a beaker and dissolving 12 grams of NH_4NO_3 and 8.8 grams of NaCl in it. This resembled a molarity of 3M NH_4NO_3 and 3M NaCl. This solution was then heated to 50°C, after which ~5 wt% Agar was added as hardener (3 grams). The mixture was then stirred with a magnetic stirrer while slowly heated to 95°C, such that the Agar melted and properly dissolved in the mixture. Finally, the hot mixture was carefully poured into two 20 ml U-shape glass tubes. It was important to ensure that no large air gaps were formed as it would nullify the performance of the ion-conductive salt bridge. Once completely filled, the salt bridges were cooled down in the fridge for half an hour at 8°C (Agar forms a hard gel at around 35°C to 40°C). After cooling the salt bridges, it was observed that the ends had slightly shrunk into the glass tubes. Therefore, as a final iteration, the salt bridges were supplemented using the initial hot mixture so that they were completely filled. This was once more cooled to yield two 20 ml U-shape salt bridges. They were always brought back to room temperature before use.

3.6. Experimental Setups

This chapter gives the methodology and details concerning the executed experiments. The four main experimental system setups are explained in the sections below. First, the full SSRFB system setup was used to test the electrochemistry of the $Mn(OH)_2$ SSE suspension versus the FeOOH SSE suspension, while separated by the filter paper membrane. Second, the half-cell setup was used for conductivity measurements and EIS of individual SSE suspensions. Third, the two-elbow setup was used for the quantitative analysis of the membranes. Finally, the full-system with salt bridge setup was used to isolate the $Mn(OH)_2$ SSE suspension and FeOOH SSE suspension and test these individually versus respectively a solid copper electrode in 1.25M $Cu(NO_3)_2$ solution and a solid zinc electrode in 1M $Zn(NO_3)_2$. The secondary experiments are described in Appendix F. All tested samples were subject to room temperature (20 °C ± 1 °C), atmospheric pressure and prepared conform the methodologies as described in the earlier chapters.

3.6.1. Setup 1: Full SSRFB System Setup

In the full SSRFB system setup the electrochemistry between the FeOOH SSE and the $Mn(OH)_2$ SSE suspensions were tested in a SSRFB setup using a cheap filter paper membrane, which gave a direct answer to the main research question of this thesis. Using this setup the 6/2-ALG/22.2-Mn/69.8-5M SSE suspension (+) was tested versus the 8/2-ALG/22.2-Mn/67.8-5M SSE suspension (-). This system started in the discharged state in accordance to the proposed reaction Eq. 1. Multiple OCV, galvanostatic and potentiostatic cycling tests were executed on this combination, as presented in Chapter 4.4.1.

This setup consisted of three glass elbow compartments, separated by two filter paper membranes. The filter paper membranes were used as these were considered to the best option based on the results of the membrane analysis (Chapter 4.3). The two outer compartments held the SSE suspensions prepared conform the methodology from Chapter 3.4, whereas the middle compartment held a 5M KOH solution (Figure 28). The addition of the middle compartment had the main function of ruling out any possibility of electric short-circuit between the SSE suspensions through the membrane. The system was assembled by first filling two elbow compartments with the prepared $Mn(OH)_2$ and FeOOH SSE suspension samples. Most of the content of the sample (20 grams), was transferred into the glass elbow (note that it does not matter how much it was exactly with respect to the aim of this thesis). Then the membrane in one of the two membrane houses was properly wet using with the $Mn(OH)_2$ SSE suspension on one side and 5M KOH solution on the other side. The same was done for the other membrane in the other membrane house using the FeOOH SSE suspension instead. The third glass elbow was filled with 5M KOH solution and the three glass elbows were then connected using the hinges, while separated by the membranes. The glassy carbon current collectors were then properly brought into contact with the SSE suspensions and connected to the Autolab. Finally, the full-system setup was air sealed with the addition of layer of argon gas to minimize any oxidizing influence from oxygen on the active material. The $Mn(OH)_2$ SSE suspension was connected with the positive glassy carbon current collector, which was connected to the working electrode and the sense of the Autolab. The FeOOH suspension was connected with the negative glassy carbon electrode, which was connected to the counter electrode and the reference electrode of the Autolab.

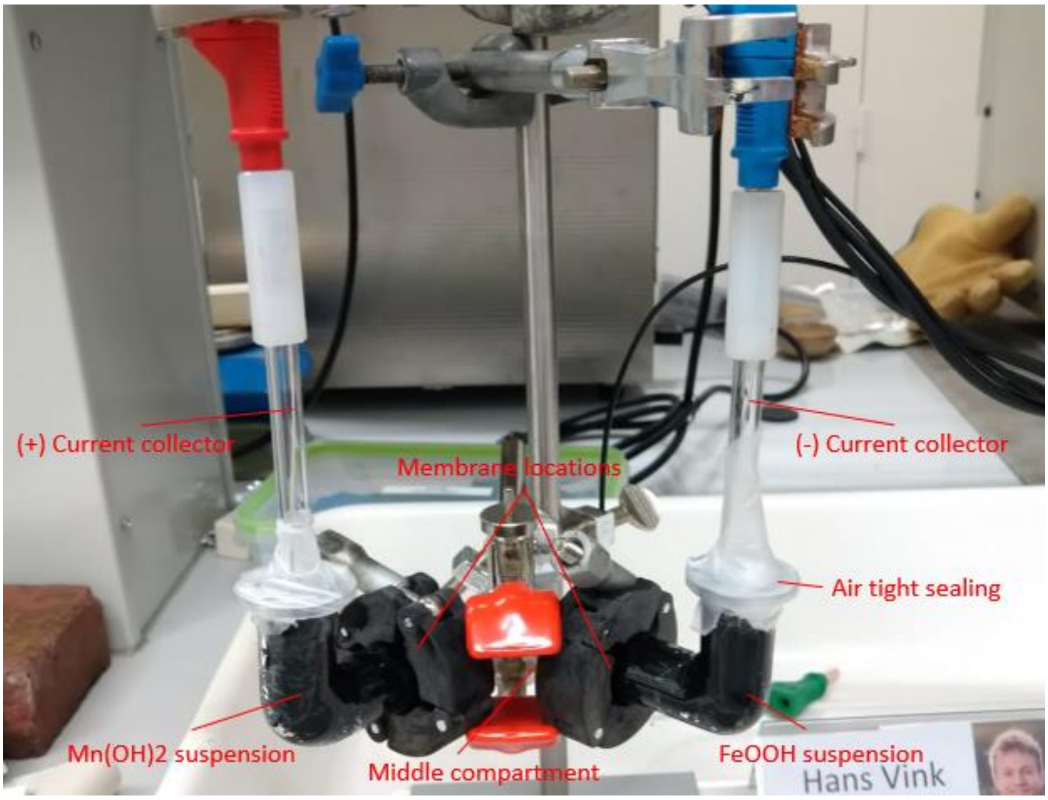

Figure 28: The full system setup (setup 1) – using 3 compartments: two for the suspensions with electroactive components and the middle one with only 5M KOH solution.

3.6.2. Setup 2: Half-Cell Setup

The half-cell setup was a highly simplified setup used to comment on the ionic and electronic conductivity of individual SSE suspensions (Figure 29). Using the Autolab two measurement techniques were executed on this setup. Using a galvanostatic measurement the electric conductivity of a setup was examined and EIS was used to gain information on ionic conductivity. This setup consisted of only one glass elbow compartment filled with a suspension brought into connection with the Autolab using two glassy carbon current collectors on each side of the glass elbow compartment. The distance between the two current collectors was 45 mm ± 5 mm.

The EIS measurements were always executed at 0 V using an amplitude of 100 mV, as various measurements showed that this yielded the most stable Lissajous Figures. This is a small deviation to literature where it is advised to maintain an amplitude of 10 mV for the most accurate results (MacDonald, 2006). Furthermore, the experiments were executed in the range of 1 MHz until 100 mHz, using 5 measurements per decade. Measurements beyond 100 mHz were found to be too time consuming.

Galvanostatic measurements were done in order to directly comment on the electric resistance of a suspension. These experiments were always executed for at least 15 minutes. The applied current was either 1 mA or 5 mA (depending on whether the resulting potential surpassed 1.2 V).

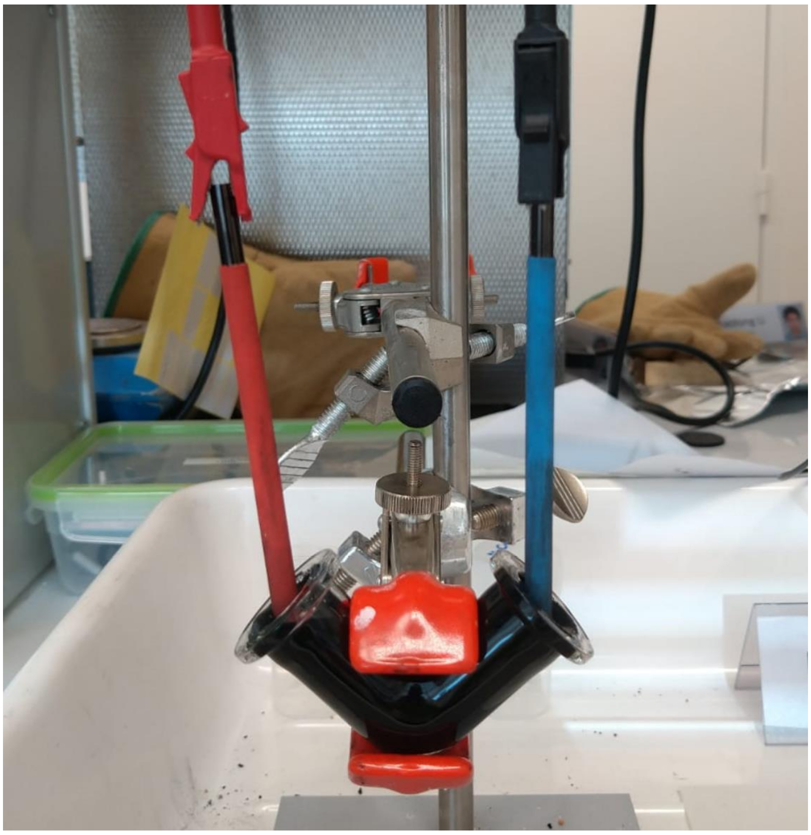

Figure 29: The half-cell setup (setup 2) – Galvanostatic current measurements and EIS applied to a suspension consisting of KB and ALG suspended in a 5M KOH solution.

3.6.3. Setup 3: Two-Elbow Setup

The two-elbow setup is the same as the full SSRFB system setup, with the exception of the middle compartment and an extra membrane house, and was used for conductivity measurements of the membranes (Figure 30). This setup consisted of two glass elbow compartments filled with electrolyte in which on each side a solid electrode was submerged into the electrolyte with a distance of 80 mm ± 5 mm. Using this setup the Whatman GFA, filter paper and Cellgard 2400 membranes were tested. Each membrane had a constant area of 1 cm^2.

For each membrane conductivity test, a different membrane was placed in between the two glass elbows and additionally one time no membrane was used as a reference. First, the membrane housing was clammed between the two glass elbows. The two elbow compartments were then filled with 25cl of 0.1 M $Cu(NO_3)_2$ solution. Next, two small sheets of copper were used as solid electrodes and submerged into the electrolyte. Each copper sheet had a weight of roughly 0.1 grams (the exact details are shared in the results section). Finally, a galvanostatic current of 1 mA for 30 minutes was applied on the setup in order to initiate the following dissolution-deposition reactions:

$$(+)\ Cu(s) \rightarrow\ Cu^{2+} + 2e^{-} \tag{22}$$
$$(-)\ Cu^{2+} + 2e^{-} \rightarrow\ Cu(s) \tag{23}$$

Concretely, at the plus pole Cu will be converted into dissolved Cu^{2+} ions and at the minus pole Cu^{2+} ions will be deposited on the Cu electrode. After the experiment the copper electrodes were properly cleaned, dried and weighted. Any weight difference before and after the experiment was the result of a successful reaction. This would only be possible when charge compensation was apparent, thus providing the prove that the membranes were ionically conductive with respect to Cu^{2+} ions.

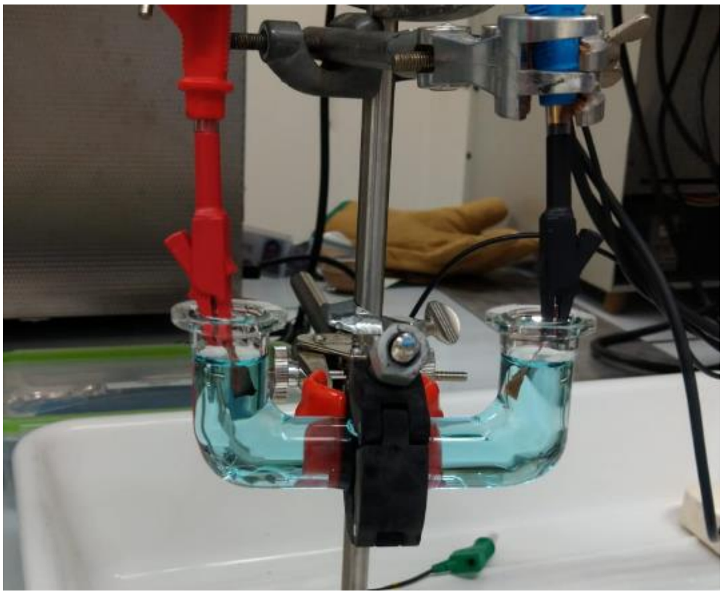

Figure 30: The two-elbow setup (test setup 3) – membrane testing in a symmetric Cu/Cu^{2+} system.

3.6.4. Setup 4: Full-System with Salt Bridge Setup

The full-system with salt bridge setup was used to individually test multiple $Mn(OH)_2$ SSE suspensions and FeOOH SSE suspensions versus respectively a solid copper and solid zinc electrode. (i) The solid copper electrode in 1.25M $Cu(NO_3)_2$ solution (+) was placed against a $Mn(OH)_2$ SSE suspension (-) and (ii) a FeOOH SSE suspension (+) was placed against a solid zinc electrode in 1M $Zn(NO_3)_2$ solution (-). The copper and zinc electrode were chosen for two reasons. First, since these will combine with the suspensions into a positive OCV and thus a spontaneous reaction would be the starting point. Second, because the respective combinations abide to the reactions for $Mn(OH)_2$ and FeOOH as proposed in this thesis (i.e. manganese from second to third oxidation state and iron from third to second oxidation state).

Spontaneous reaction: FeOOH to $Fe(OH)_2$ (cell potentials according to theory) E^0_{cell}= 0.2 V

$$(+)\ 2\,FeOOH + 2\,H_2O + 2e^- \leftrightarrow 2\,Fe(OH)_2 + 2\,OH^- \quad E^0 = -0.56\,V \tag{24}$$

$$(-)\ Zn^{2+} + 2e^- \leftrightarrow Zn \quad E^0 = -0.76\,V \tag{25}$$

Spontaneous reaction: $Mn(OH)_2$ to $Mn(OH)_3$ (cell potentials according to theory) E^0_{cell} = 0.22 V

$$(+)\ Cu^{2+} + 2e^- \leftrightarrow Cu(s) \quad E^0 = +0.37\,V \tag{26}$$

$$(-)\ 2\,Mn(OH)_2 + 2\,OH^- \leftrightarrow 2\,Mn(OH)_3 + 2\,e^- \quad E^0 = +0.15\,V \tag{27}$$

Regarding the assembly, instead of using the glass elbow compartments, 50 ml plastic jars were used as housing (the same as in which the SSE suspensions were prepared). Each side was configured with the respective combinations presented in the previous paragraph and connected to the Autolab. An advantage of not using the glass elbows was that the prepared SSE suspensions could now directly be used without having to transfer them from 50 ml plastic jars to the glass elbows (keeping the content constant at 20 grams). For the SSE suspensions, glassy carbon was used as current collector, whereas the solid zinc and copper electrodes functioned both as electrode and current collector on their side. The circuit was closed by connecting it using the prepared salt bridge (Figure 31). Addition of the salt bridge ensured that no Zn^{2+} or Cu^{2+} ions would cross-over to the SSE suspensions, avoiding any influence on their electrochemical behaviour.

Galvanostatic charge/discharge tests were applied at speeds of 1 mC, 4 mC and 10 mC with a cut-off voltage of 1.4 V to avoid electrolysis of water. The DoD at which this cycling happened was 1%, starting at SoC_0 = 100%. During these charge/discharge tests, multiple OCV measurements were done at the end of every cycle to comment on the stability of the electrode. The amount of Cu, Cu^{2+}, Zn and Zn^{2+} was over-dimensioned heavily so that their concentration difference during the low DoD was minimal (and thus the cell potential of the Zn and Cu half-cells should remain virtually constant). Any variation in OCV could then be assigned to instability of the SSE suspensions.

Additionally, an Ag/AgCl reference electrode was added to this setup to retrieve the $Mn(OH)_2$ and FeOOH SSE cell potentials vs SHE. The electrolyte inside the Ag/AgCl reference electrode was 3M KCl and was brought in contact with the SSE suspensions of interest. The ionic conductivity arose via contact of the respective suspension with the ion-exchanging membrane of the Ag/AgCl reference electrode. The membrane area was miniscule, resulting in a very stable electrode potential as KCl molarity stays approximately constant and contamination is minimized. Before usage the reference electrode was calibrated at 0.21 V vs SHE, which is in line with the theoretical value (“Reference Electrode Potentials,” 2016). During these experiments, the working electrode and the counter electrode of the Autolab were connected to the SSE suspension and the solid zinc or copper electrode, while the sense and the reference electrode of the Autolab were connected to the SSE suspension and the Ag/AgCl reference electrode.

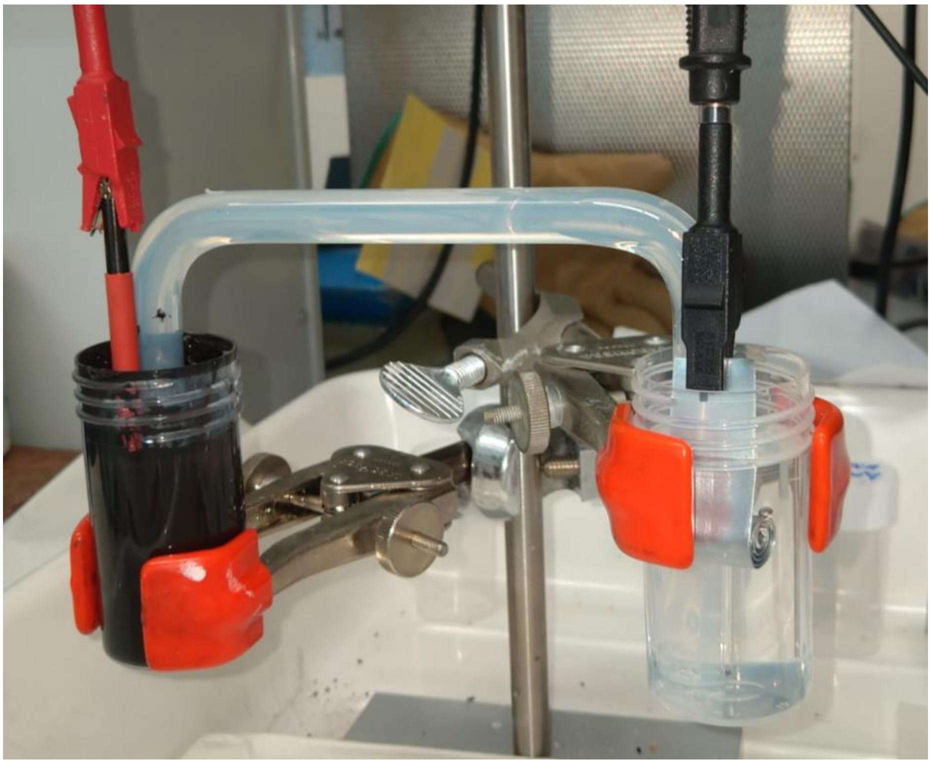

Figure 31: The full-system with salt bridge setup (test setup 4) – FeOOH SSE suspension versus Zn electrode in 1M Zn^{2+} solution (before airtight sealing with parafilm tape).

4. Results and Discussion

In this chapter it is shown how a SSRFB based on a FeOOH SSE suspension versus a $Mn(OH)_2$ SSE suspensions could not be electrochemically charged and discharged because of the specific combination of the active materials in the highly alkaline environment. This follows systematically from both the qualitative and quantitative results of the executed experiments. First, in Chapter 4.1 is shown that colloidally stable SSE suspensions with acceptable viscosities were made. Then, in Chapter 4.2, this is expanded with results showing that the SSE suspensions are additionally both electronically and ionically conductive. This is followed by Chapter 4.3, in which is shown that a high flexibility with respect to membrane choice exists and that a cheap microfiltration membrane suffices for this SSRFB system. Subsequently, in Chapter 4.4, these components are combined into a SSRFB configuration and it is shown that the SSRFB in itself works, but that the problem lays within a complex electrochemical equilibrium system of both FeOOH and $Mn(OH)_2$ in highly alkaline aqueous environments and that, as a result of unforeseen side-reactions, the proposed electrochemical reaction (Eq. 1) does not hold. It is then further substantiated that the SSE suspensions themselves are functional, because both the cheap FeOOH and the cheap $Mn(OH)_2$ SSE suspension can be electrochemically discharged and charged versus respectively a solid zinc and a solid copper electrode, while separated by a salt bridge.

4.1. Colloidal Stability and Viscosity

This chapter presents and discusses the results with respect to the colloidal stability and viscosity of suspensions. To prevent sedimentation of active material or flotation of KB particles, it is important that a SSE suspension is colloidally stable (Parant et al., 2017). From the literature study in Chapter 2.2.6 was concluded that an important contribution to colloidal stability is an increased viscosity as that relates to a higher zeta potential. However, viscosity should be maintained within acceptable limits both for homogenous mixing, as well as for possible flow operation in future research. This contradiction is evidenced by the results in this section and requires optimization of the colloidal stability of SSE suspensions. From the experiments it was observed that addition of PAA as emulsifier most effectively increased the colloidal stability while maintaining a pasty-liquid suspension in a highly alkaline environment ($pH > 14$). Such suspensions showed shear-thinning behaviour, an advantageous characteristic for SSE suspensions for adequate mixing and flow operation. As a final note, mixing with the Ultra Turrax mixer at high rotational speeds showed to be essential to break agglomerates and create homogeneity and proofs to be a fundamental technique in the preparation of SSE suspensions.

An experiment that compared the colloidal stability of suspensions holding ALG or PVP in similar highly alkaline compositions, shows how the use of ALG resulted in temporary colloidal stability (between 4 and 48 hours), whereas the use of PVP did not lead to colloidal stability at all (< 4 hours) (Figure 32).

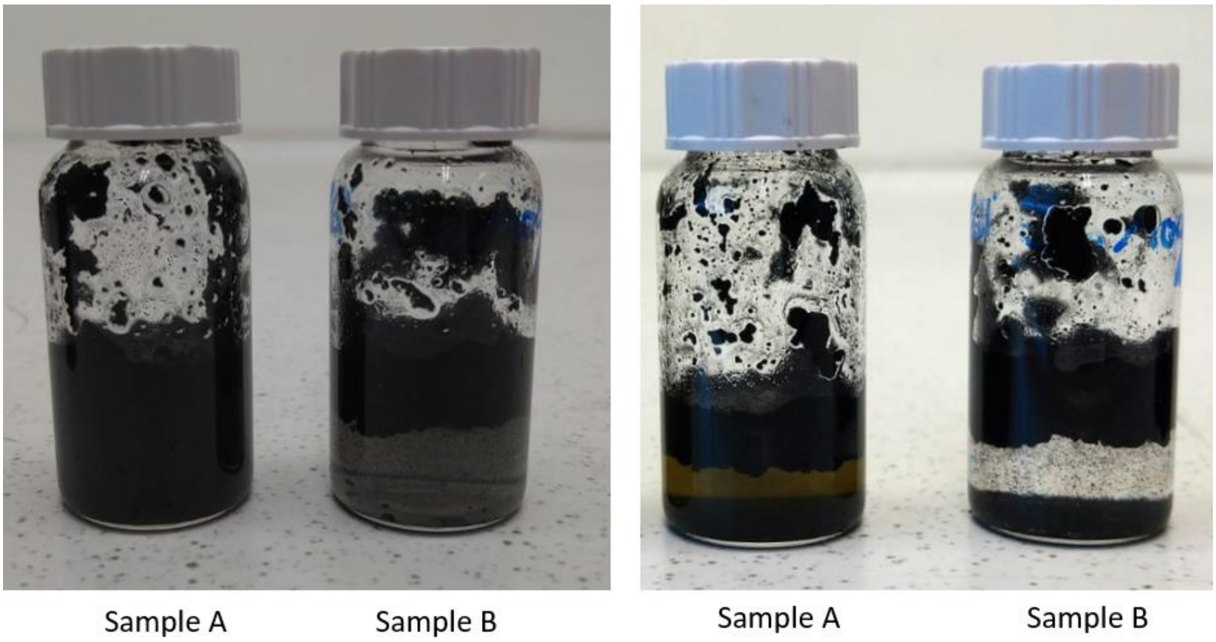

Figure 32: Comparing colloidal stability of sample A (5/1.5-ALG/-/93.5-5M) and sample B (5/1.5-PVP/-/93.5-5M): (left) after 4 hours and (right) after 48 hours.

A later experiment that compared the colloidal stability of suspensions holding no emulsifier, ALG or PAA in similar compositions, shows that the difference in colloidal stability between no emulsifier and ALG is minimal after a period of 48 hours. However, the colloidal stability of the suspension holding PAA was still intact (and stayed intact during this thesis). Therefore, a significant increase in colloidal stability was observed while using PAA (Figure 33).

Figure 33: Comparing colloidal stability of sample A (4/-/-/96-5M), sample B (4/2-ALG/-/94-5M) and sample C (4/1-PAA/-/95-5M) after 48 hours.

These results indicate that the effectivity of ALG decreases with an increase of pH. This is in accordance with literature on this matter which states that, above pH 11, slow depolymerization of ALG occurs, giving a fall in viscosity (Qin, 2018). The decomposition of ALG into monomers thus removes the required structure needed for to create a colloidally stable suspension.

However, suspensions holding ALG proved to also be capable of providing long-term colloidal stability, on the condition that enough of both KB and active material was used in the composition. The term “stable” relates to the fact to no segregation occurred between the KOH solution, KB particles and active material particles over the duration of the thesis. The viscosity at which this occurred was observed to be, however, significantly high. This is substantiated by the 6 samples in Figure 34 which were made using ALG, that all show a paste-like up to almost solid-like structure. These suspensions all showed to be colloidally stable. It is expected that the contribution of ALG to achieving this is rather minimal. This can be related back to the relationship between colloidal stability and viscosity as earlier explained in Chapter 2.2.6. The colloidal stability of these suspensions can thus very well, simply, have been the result of the addition of enough KB and active material, leading to a high enough viscosity increase.

Nonetheless, it was experienced that the use of both ALG or PAA had a positive effect on the homogeneity during the preparation of suspensions, compared to preparation without emulsifier. It is believed that mitigation of the hydrophobic character of KB is at the source of this, following from the (temporary) increase in colloidal stability as a result of addition of an emulsifier (Parant et al., 2017). The use of ALG thus proved to be advantageous to this regard.

In general, the addition of $Mn(OH)_2$ resulted in a dryer, more solid-like suspension than addition of the same amount of FeOOH. As a result a maximum of 6 wt% KB was used in $Mn(OH)_2$ suspensions in order to comply to a viscosity that was workable, instead of a maximum of 8 wt% KB which was used for FeOOH SSE suspensions. A clear difference can be observed in Figure 34, but also in Figure 35.

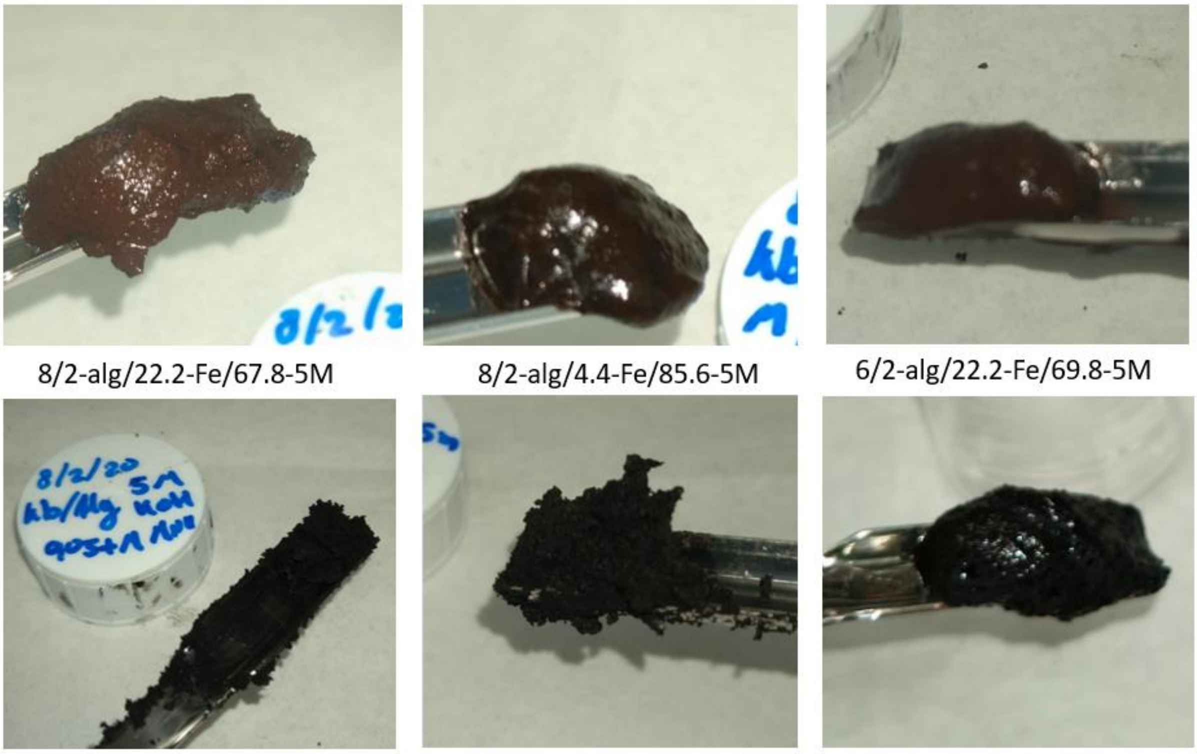

8/2-alg/22.2-Fe/67.8-5M 8/2-alg/4.4-Fe/85.6-5M 6/2-alg/22.2-Fe/69.8-5M

8/2-alg/22.2-Mn/67.8-5M 6/2-alg/22.2-Mn/69.8-5M 4/2-alg/22.2-Mn/71.8-5M

Figure 34: Colloidally stable SSE suspensions consisting of ALG, 5M KOH, KB and active material, showing a high viscosity up to even solid-like characteristics.

Upheld by Figure 35, it can furthermore be clearly seen that the use of PAA instead of ALG resulted in colloidally stable suspensions that were more homogeneous and less viscous. Added to this, more than 10 times less wt% PAA was needed compared to ALG to achieve these better results. Moreover, PAA SSE suspensions showed higher shear-thinning behaviour than the respective SSE suspensions using ALG. This was observed mainly by the ease with which homogeneous mixing happened during their preparation while using the Ultra Turrax mixer.

Preparation and observation of suspensions using PAA also show that addition of 2 wt% PAA surpassed the jamming transition. It was possible to hold the suspension upside down or to gently shake it and the shear rate would be still be nihil, as no movement was observed. By then using the Ultra Turrax mixer again, the shear-thinning behaviour was very much obvious due to transformation of the suspension to a liquid substance. Interestingly, application of a jamming transition was measured to have a highly negative impact on electronic conductivity (further elaborated in the next chapter). However, it was found that 0.2 wt% PAA resulted in an increased viscosity and a stable colloidal suspension, while being far from the jamming transition (indicated by the ease with which movement of the mixture was possible, even under low shear stress). The electric conductivity of these suspensions was also found to be significantly higher compared to ones holding 1 or 2 wt% PAA. This stresses that the application of soft jamming materials can be used to an advantage with respect to achieving colloidal stability, but should also be minimized in order to maintain enough electronic conductivity.

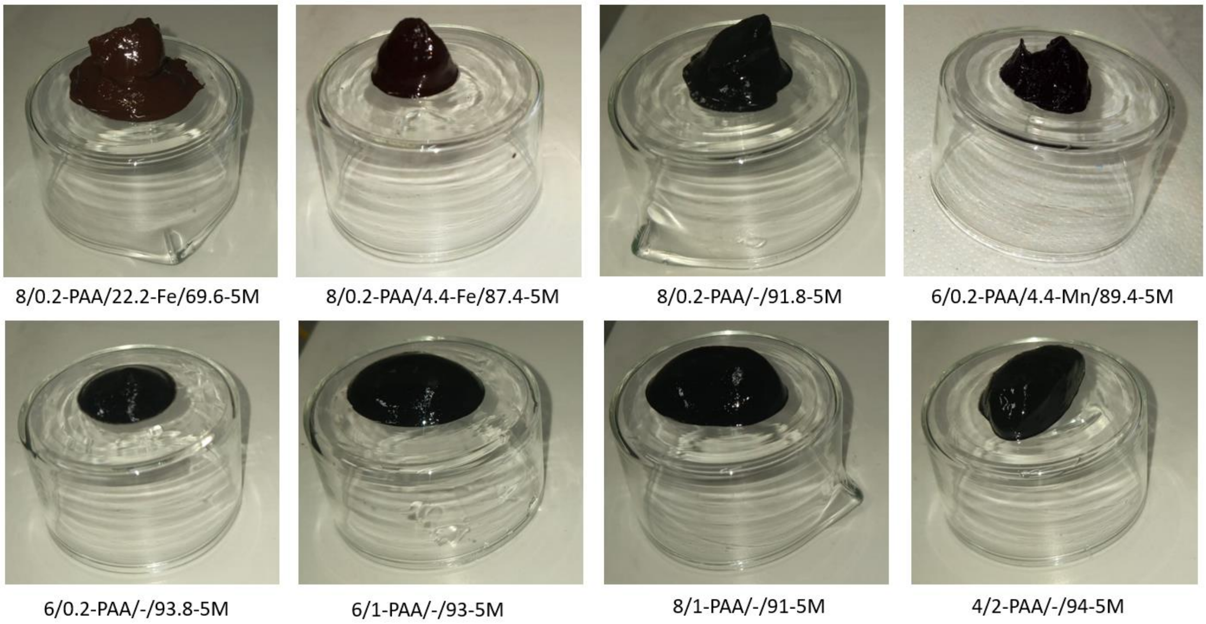

8/0.2-PAA/22.2-Fe/69.6-5M
8/0.2-PAA/4.4-Fe/87.4-5M
8/0.2-PAA/-/91.8-5M
6/0.2-PAA/4.4-Mn/89.4-5M
6/0.2-PAA/-/93.8-5M
6/1-PAA/-/93-5M
8/1-PAA/-/91-5M
4/2-PAA/-/94-5M

Figure 35: Colloidally stable SSE suspensions consisting of PAA, 5M KOH, KB and active material, showing a moderate to high viscosity.

Besides the latter, the colloidal instability of KB in highly alkaline (pH>14) conditions proved to be higher than in pH neutral conditions. This can be related back to an increase in the Debye-Hückel parameter, due to the increase of bulk concentration, n_i^∞, when going from a neutral to a 5M KOH solution. As stated in Chapter 2.2.6, an increase of the Debye-Hückel parameter is inversely related to the thickness of the electric double layer. Effectively, when increasing the pH by a higher molarity KOH, one decreases the thickness of the electric double layer of particles in the suspension. Eqs. 17 and 18 show how a thinner double layer can lead to a lower zeta potential, which is proven to be an indicator of colloidal stability (Parant et al., 2017; Pate & Safier, 2016).

The relationship between colloidal stability, viscosity and conductivity has been briefly touched upon in this chapter. It was found that addition of KB and active material to SSE suspensions is bounded by viscosity constraints and that soft jamming materials such as PAA effectively add to colloidal stability in highly alkaline solutions, but come at the cost of a decline in electric conductivity. Next chapter elaborates on this and dives more deeply in the conductivity of SSE suspensions.

4.2. Conductivity of Suspensions

In this section the results with respect to the conductivity of SSE suspensions are presented and discussed. Table 2 shows a summary of the most important results, which essentially confirm that both ionic and electronic pathways are present in fully designed SSE suspensions. The electronic pathway shows between one and two orders of magnitude higher resistances than the ionic pathway. Further results suggest that the sensitivity of the ionic resistance with respect to the amount of solid KB and active material is low and actually is more sensitive to inconsistencies in the preparation of chemicals and the measurement setup. The contrary is true for the effectivity of the KB network, which shows to be highly sensitive to design choices such as the amount of KB and the type and amount of emulsifier. Finally, analysis of the results show that the relationship between the measured ionic and electronic resistance cannot be related to their conductivities using simple geometrical relationships, but rather suggest that a complex interconnected mechanism between the electronic and ionic conductivity exists.

Table 2: Summary of conductivity data and results.

Suspension	**$R_{0\text{-high}}$ [Ω]**	**R_{KB} [Ω]**	**R_{ion} [Ω]**	**Wt_{KB} / wt_{KOH} [%]**
0/0/-/100-5M *(reference)*	10.3	∞	10.3	-
6/0.2-PAA/-/93.8-5M	7.4	474	7.5	6.4
8/0.2-PAA/-/91.8-5M	8.7	243	9.0	8.7
8/0.2-PAA/4.4-Fe/87.4-5M	7.6	318	7.8	9.2
8/0.2-PAA/22.2-Fe/69.6-5M	-	290	-	11.5

From an experiment regarding the electronic conductivity of suspensions holding KB and ALG or PAA in a pH-neutral aqueous environment, two important observations were made. First, the percolation threshold of KB in an pH-neutral aqueous environment was found to be 6% (wt_{kb}/wt_{water}) (Figure 36). Above 6% KB (wt_{kb}/wt_{water}) a significant increase in σ_e is observed with increasing KB content. At 7 wt% KB (7/2-ALG/-/91-0M) this was between $20 < \sigma_e < 80$ mS/cm and at 8 wt% KB (8/2-ALG/-/90-0M) this increased to values in between $90 < \sigma_e < 130$ mS/cm. For values < 6 wt% KB this was found to be below 1 mS/cm. Second, from a similar experiment investigating the influence of ALG and PAA on the electronic conductivity follows that with an increasing wt% ALG or PAA, the electric conductivity decreases.

These results suggest that for retrieving a high σ_e it is wishful to be above the percolation threshold as the value of σ_e increases with an order of magnitude per wt% KB around that point. At the same time, from a σ_e perspective, the less emulsifier can be used to create a colloidally stable suspension, the better. The values during these experiments were capped at 200 mS/cm as they were done using the conductivity meter (Chapter 3.2). The found percolation threshold is in accordance to that of existing literature (Parant et al., 2017).

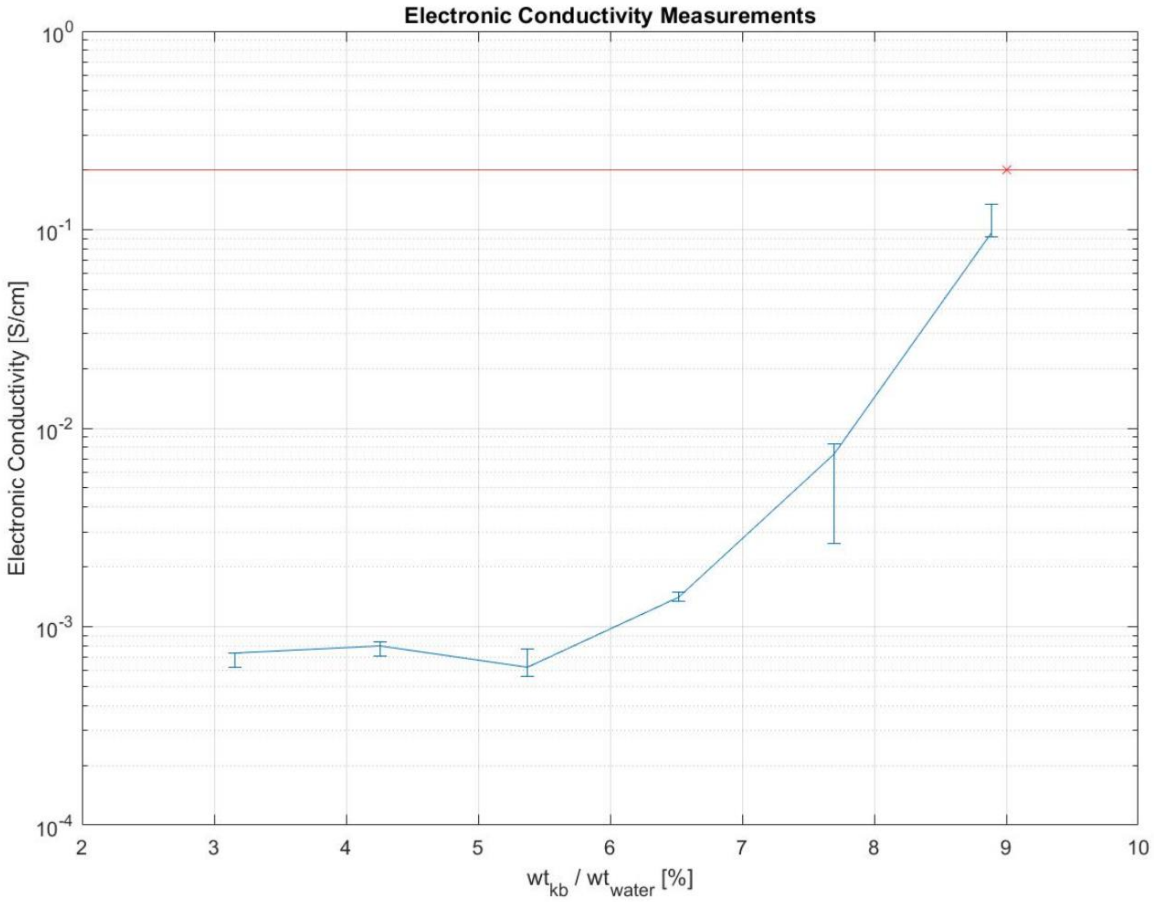

Figure 36: Results of the electronic conductivity measurements at (left to right) 3, 4, 5, 6, 7 and 8 wt% kb, using 2 wt% Alginate and H_2O.

Figure 37 shows the results of EIS measurements of some of the best performing SSE suspensions that show a touchdown with the real-impedance axis of the Nyquist plot (Appendix I for more EIS results). This always occurred in the high frequency spectrum. Over the testing of dozens of suspensions, never have two touchdowns with the real impedance axis been observed. It is furthermore noted that even the best EIS results show non-ideal behaviour as no clear semi-circles can be found. Recall that Eqs. 13 and 14 describe the relationship between the ionic and electronic resistance to the touchdowns of a Nyquist plot with the real axis. The intersections of the samples from Figure 37 with the Z_{real} axis are retrieved from the data and presented in Table 2 (“$R_{0\text{-real}}$”). Note that in order to relate these to R_{ion}, the values for R_{kb} are required (Eq. 13) and since no touchdowns at low frequencies are observed Eq. 14 cannot be used. Therefore, the unknown R_{kb} is retrieved from the galvanostatic conductivity measurements. The exception to this are samples with an extremely high electric resistance (like a pure 5M KOH solution), for which R_{ion} may be assumed equal to $R_{0\text{-}real}$ (Appendix G).

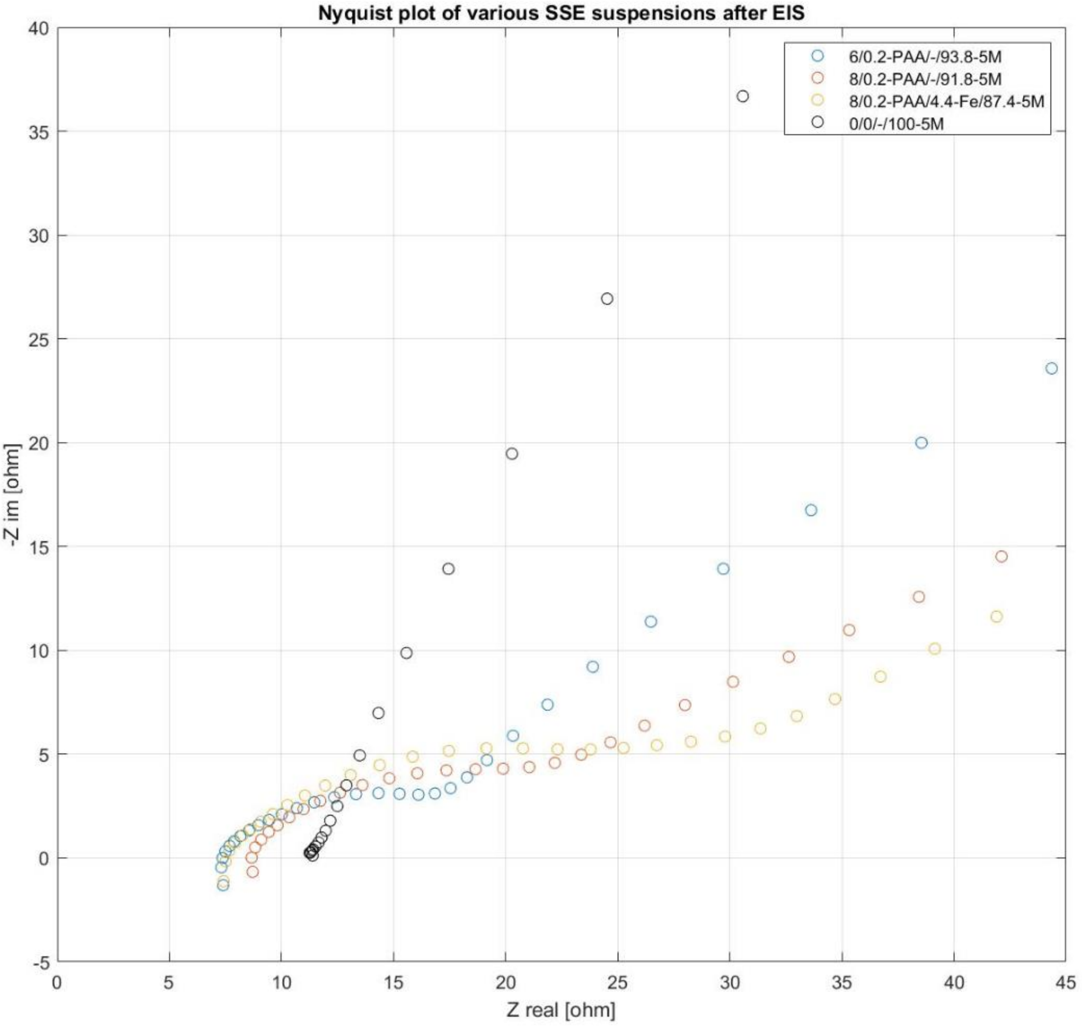

Figure 37: EIS measurement results for some of the best performing suspensions.

Figure 38 shows the results for the galvanostatic conductivity measurements for the considered samples. The results show that for all three measurements the potential can be considered to be constant in between t = 800 s and t = 900 s (the standard deviation of the measured potential is less than 0.1% over this interval). According to Ozoemena & Kebede it is allowed to retrieve the electronic resistance via Ohm's law when the potential and current are both constant in time (Eq. 15) (Ozoemena & Kebede, 2016). Therefore, the mean of the data for above-mentioned interval is taken and translated into the electric resistance of the SSE suspensions. The results are presented in Table 2 ("R_{kb}"). Now, with R_{kb} known, there is enough additional information to retrieve the ionic resistance conform Eq. 13, of which the results are also shown in Table 2 ("R_{ion}").

Relating the ionic resistances to their conductivities, so that they could be compared to literature, proved to be ineffective for two different methods. First, the attempt to connect the measurement setup (setup 2) to a geometrical shape factor ("α") showed inconsistencies.

To this regard the measured ionic resistance of a pure 5M KOH, 1M KOH and 0.1M KOH solution retrieved from EIS measurements were connected to their theoretical values via a shape factor α (Gilliam et al., 2007). However, the found shape factor has respective values of 26, 15.7 and 13.0. Due to its inconsistency it was decided not to use this. Second, attempts to connect R_{ion} to σ_i via the distance between the glassy carbon current collectors and its surface area (Eq. 28) also seemed ineffective, as this resulted in values for the ionic conductivity two orders of magnitude lower than what should be the case.

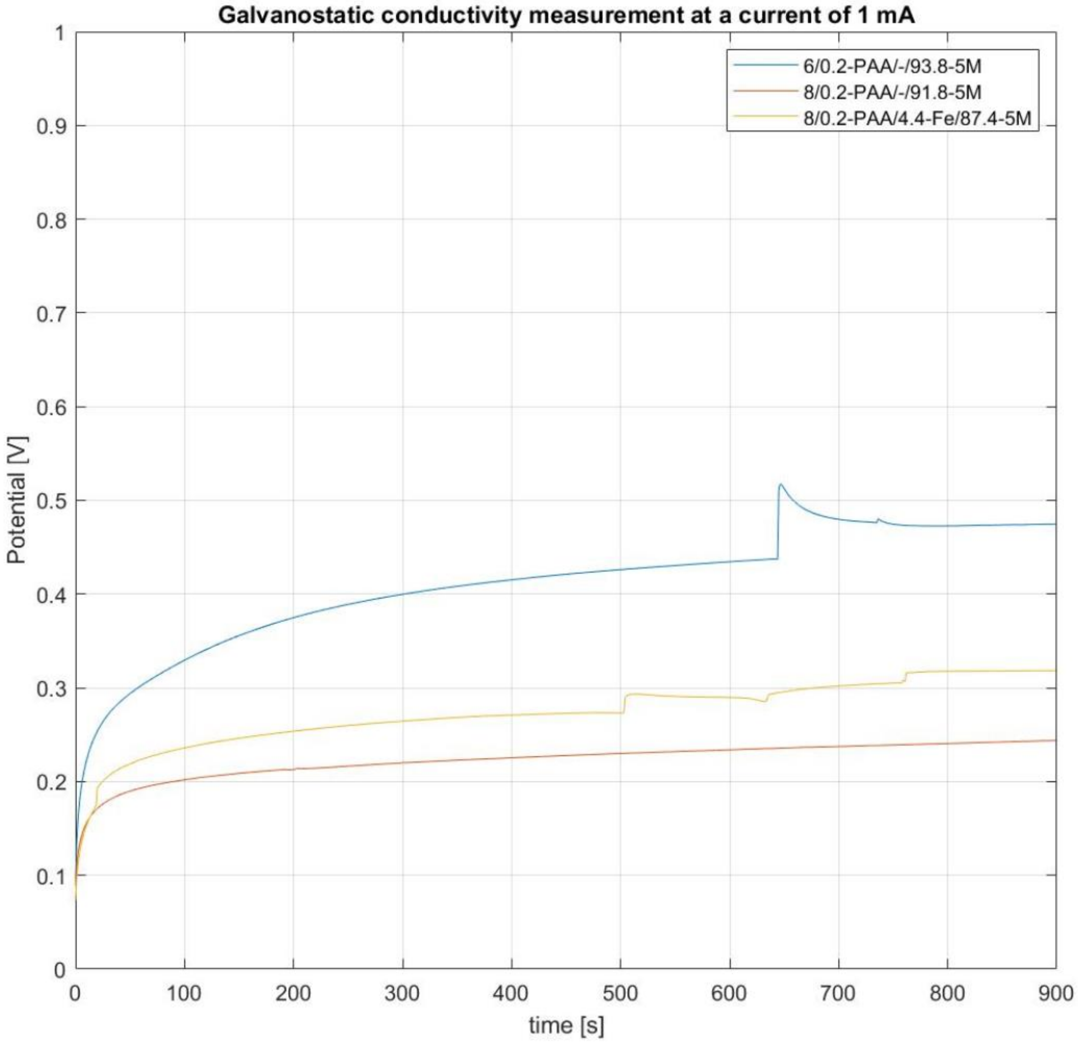

Figure 38: Galvanostatic measurement results for some of the best performing SSE suspensions.

$$\sigma = \frac{d_{el}}{R\,A_{gc}} \tag{28}$$

The relationship between the measured R_{kb} and Eq. 28 was also used with respect to σ_e, the results of which shared in Table 3. Although relatively close for a KB% ($w_{kb}/w_{solution}$) far above percolation threshold and PAA as emulsifier (error margin <50% for 8.7%, 9.2% and 11.5% $w_{KB}/w_{solution}$), for values around and below percolation threshold (6% $w_{kb}/w_{solution}$), Eq. 28 seems to make an overestimation more than two orders of magnitude.

The inability to properly connect the values for σ to values from literature via Eq. 28 or via α suggests a system of higher complexity that includes a co-dependence between the ionic and electronic conductivity. This follows from the fact that they both have their own phase (liquid and solid) and from related matters such as the active surface area, active distance, active volume of both phases. As an example, it is comprehendible that the KB path itself between the electrodes is also active with respect to the calculated R_{ion} during the EIS tests. This instinctively increases the active surface area, which would translate in a higher σ_i than currently calculated using A_{gc} (which following the above methodology is 2 orders of magnitude too low). Although interesting to retrieve ionic and electronic conductivity so that these can be compared to values in literature (good for optimization), knowing that ionic and electronic paths exist with resistances that seem acceptable provides enough evidence that an effective environment is constructed for electrochemical testing of the active materials in the SSE suspensions.

*Table 3: Comparison of σ_e retrieved from this study via R_{kb} and Eq. 28 to values in literature. Note samples indicated with * were made using ALG and are less reliable due to colloidal instability which was observed even during measurement. The others were made using PAA.*

$w_{kb}/w_{solution}$ of sample [%]	**σ_e [mS/cm] (current report)**	**σ_e [mS/cm] (Parant et al., 2017)**
4.2*	15.4	0.04
6.4	47.5	0.1
6.5*	30.0	0.1
8.7	93.0	50
8.9*	34.1	60
9.2	70.8	70
11.5	77.6	110

There are some interesting findings when considering these results. For example, take note of the fact that $R_{0\text{-}high}$ can almost be considered to be equal to R_{ion}, even after addition of the 8 wt% KB and 4.4 wt% FeOOH (=10 mmol). This shows that in the prepared SSE suspensions the ionic resistance is significantly less sensitive to SSE composition than the electronic resistance. Second, note further how the negative influence of the addition of kb, active materials and emulsifiers with respect to ionic resistance is insensitive with respect to measurement errors. The results in Table 2 show that R_{ion} is actually lower for a 5M KOH solution in combination with KB particles, emulsifier and active material than a solution merely consisting of a 5M KOH solution. This cannot be justified other than following from measurement errors. The measurement errors most likely follow from inconsistencies in the distances between the electrodes (± 10%), volume of samples, weighing of chemicals and temperature (± 1°C). Third, note how up to $t > 500$ s a significant variability in potential can be seen during the galvanostatic conductivity measurement. Seeing as the tested SSE suspensions were one of the best electronically conductive SSE suspensions tested, this explains why no second touchdown with the Z_{real} axis was ever seen during EIS measurements. At the lowest applied EIS frequency (100 mHz) the DC time-interval is 5 s (half of the period), for which the results in Figure 38 show that the potential at that time was near from constant. For a second touchdown to become possible, the EIS measurement should have continued up to at least 1 mHz and possibly even lower (1 mHz ~ DC interval of 500 s). Finally, using EIS, two important trends were found with respect to ionic conductivity. It was found that R_{ion} progressively increased with an increasing molarity KOH, showing a 650% increase between 0.1M and 1M KOH solution and only a 68% increase between 1M and 5M KOH solution. This behaviour is in line with literature showing a parabolic relationship between the specific conductivity and the molarity of KOH solutions, peaking at a concentration of 6M KOH (Gilliam et al., 2007). It was further found that the addition of solid particles in suspension had no significant effect on the ionic conductivity of the suspension.

When broadening the galvanostatic conductivity experiments to more sample configurations it is found that use of PAA leads to a significantly lower electronic resistance than ALG in a setup with a similar amount of KB in 5M KOH solution (Table 4). Even more, 10 times less wt% PAA was used, substantiating its effectivity even further. This is suspected to be the consequence of PAA having a higher colloidal stability than ALG in a highly alkaline environment. These results follow from galvanostatic conductivity measurements at 1 mA, capped at 1.4 V to avoid electrolysis of water. Experiments using similar compositions, but higher amounts of PAA showed that it was impossible for a suspension holding >1 wt% PAA be executed at this current as it reached the cut-off voltage within a minute and never got to a stable potential. This proofs that those suspensions were less electronically conductive. It is therefore believed that jamming soft particles can improve electronic conductivity via the creation of more stable pathways, but that the same jamming mechanism that helps creating the extra stability and extra pathways also can block pathways of the KB network.

Table 4: Comparison of effectivity of PAA and ALG.

Suspension	**wt_{kb} / $wt_{solution}$ [%]**	**R_{kb} [Ω]**
6/0.2-PAA/-/93.8-5M	6.4	474
8/0.2-PAA/-/91.8-5M	8.7	242
6/2-ALG/-/92-5M	6.5	750
8/2-ALG/-/90-5M	9.2	660

The results from the previous two chapters show that the creation of effective and optimized SSE suspensions is one of complex balance between colloidal stability, viscosity, ionic conductivity and electronic conductivity. Moreover, it has been shown that the current balance of the best made SSE suspensions provide a suitable environment for electrochemical testing of the iron-manganese SSRFB. However, discussion of the results of the membrane analysis is necessary before moving on to the electrochemical behaviour of the SSE suspensions.

4.3. Membrane Analysis

The results of the executed membrane conductivity experiments show that all three analysed membranes are ionically conductive with respect to Cu^{2+}, of which filter paper shows the best results. Moreover, all membranes effectively prevented problematic solid particle cross-over and showed porous behaviour with respect to (blue) Cu^{2+} ions (Appendix H).

Table 5 shows that a galvanostatic current of +1mA for 30 minutes consistently resulted in 0.5 mg of copper deposition/dissolution for each test in the symmetrical Cu/Cu^{2+} system separated by a membrane (setup 3), proving ionic conductivity of the membranes. It is assumed that when the membrane was capable of conducting Cu^{2+} ions with an ionic radius of 0.73 Å, it would also be capable of doing so for OH^- with an effective radius of 1.10 Å.

Table 5: Deposition-dissolution results for the membrane conductivity tests in the symmetrical Cu/Cu^{2+} system (Chapter 3.6.3).

	(+) Weight before [g]	**(+) Weight after [g]**	**(-) Weight before [g]**	**(-) Weight after [g]**	**Delta weight [mg]**
Whatman GFA	0.1078	0.1073	0.0840	0.0845	0.5
Cellgard 2400	0.1073	0.1068	0.0845	0.0850	0.5
No membrane	0.1068	0.1063	0.0850	0.0855	0.5
Filter paper	0.1063	0.1058	0.0855	0.0860	0.5

Figure 39 shows that indeed filter paper requires the smallest overpotential compared to the Cellgard and Whatman membrane. The results show that the filter paper, Cellgard and Whatman membrane respectively increased the required potential with 14.4%, 21.6% and 32.5%, compared to the reference measurement without a membrane. Interestingly, the nano-porous Cellgard membrane is more energy efficient than the microporous Whatman membrane. It is possible that the smaller pore size of the extremely thin Cellgard membrane had a smaller negative effect than the large thickness and woven layered structure of the microporous Whatman membrane.

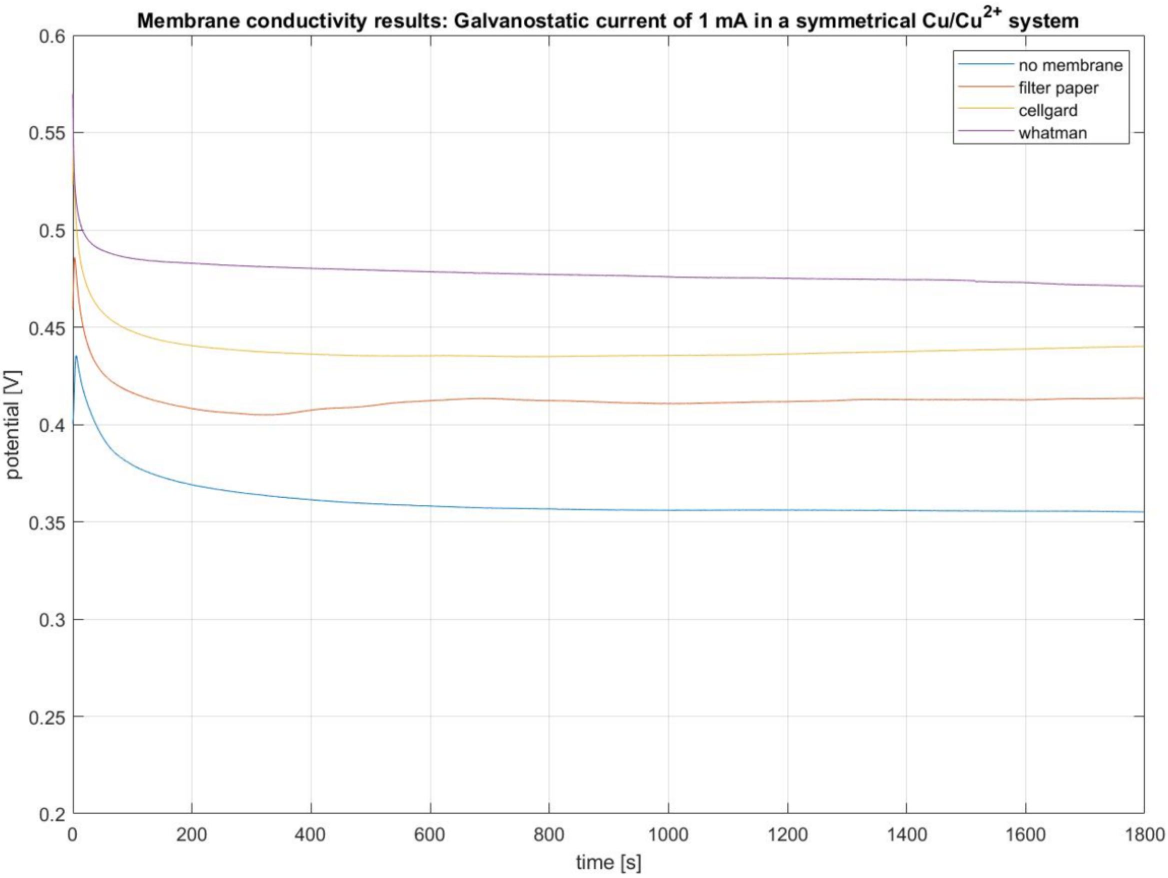

Figure 39: Membrane conductivity measurement results for filter paper, Whatman GPA and Cellgard 2400 membranes with respect to no membrane in a symmetrical Cu/Cu^{2+} system (setup 3).

When considering the membrane porosity with respect to cross-over of solid material from the SSE suspensions (KB, ALG, FeOOH and $Mn(OH)_2$), it is observed that Cellgard is the most attractive choice. Whereas Cellgard did not show any solid particle cross-over at all, both Whatman and filter paper showed a minimal amount of small black particles had penetrated through the membranes after 48 hours (barely visible with the naked eye). This was extra motivation for experimental setup 1 for tests concerning electrochemical testing of the full system, where use was made of a third middle compartment with KOH solution and an extra membrane to simply exclude the risk of a short-circuit. In practise such a buffer layer would not need to be thick, as only a minimal amount of solid particles has shown to pass through.

All-in-all, the solid particle cross-over was so small with respect to the slurry sizes, that the cheapest membrane with the lowest overpotential was decisive as membrane choice in the full system setup – the filter paper membrane.

4.4. Electrochemical Behaviour

The results from Chapters 4.1 and 4.2 show that ionic and electronic conductive SSE suspensions can effectively be created while being colloidally stable and not too viscous. In Chapter 4.3 it was shown that the filter paper membrane showed best overall results with respect to price, efficiency and solid particle cross-over prevention. With the proper environment created, this chapter presents and discusses the results of electrochemically testing the iron and manganese SSE suspensions in a SSRFB configuration, as well as separately versus a zinc or copper electrode while separated by a salt bridge.

4.4.1. $Mn(OH)_2$ – FeOOH SSRFB

Two charge-discharge procedures of a (+) $Mn(OH)_2$ SSE suspension versus (-) FeOOH SSE suspension, while using a SSRFB setup, confirm that the system does not electrochemically store energy with respect to the proposed electrochemical reaction in Eq. 1. It is shown that the setup itself is functional, but that the problem lays with combination of active material in the high alkalinity.

Two conductive $Mn(OH)_2$ and FeOOH SSE suspensions have been tested using experimental setup 1, while being separated by two filter paper membranes and a 5M KOH solution in the middle compartment. Recall the theoretical electrochemical reactions (Eq. 1), on which these active materials have been chosen. Theoretically speaking a cell voltage of 0.63 V was expected between the (+) $Mn(OH)_2$ SSE suspension and the (-) FeOOH SSE suspension in a 5M KOH environment (Chapter 2.2.2) and the systems starting point should be $SoC_0 = 0\%$ (Eqs. 2 and 3).

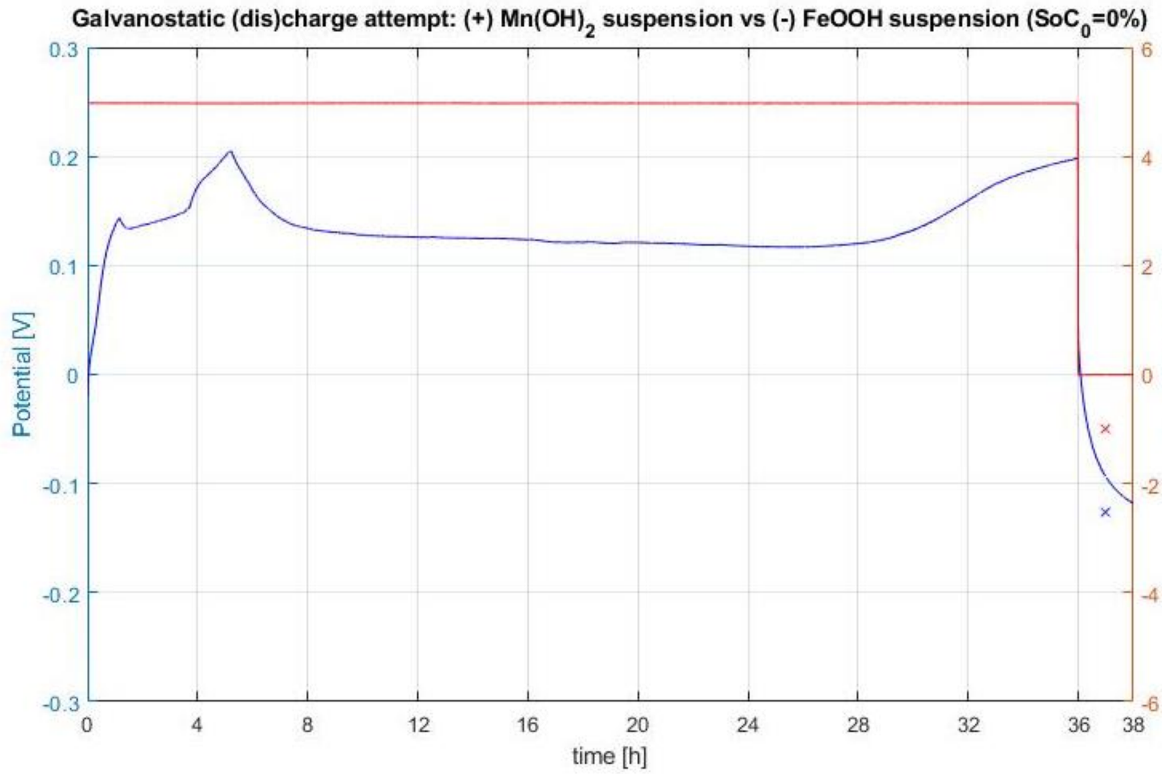

Figure 40: Galvanostatic (dis)charge attempt of SSE suspensions: (+) 6/2-ALG/22.2-Mn/69.8-5M versus (-) 8/2-ALG/22.2-Fe/67.8-5M (SoC$_0$=0%). First 36 hours charging at 4 mC, then 1 hour relaxation (I = 0 A), then a discharge command at ~1 mC (the "x" represent the instant cut-off due to potential < 0 V), followed by another hour relaxation (I = 0 A).

Figure 40 shows the results of the first attempt to electrochemically charge and discharge the battery. It was measured that prior to this measurement the OCV was -0.2 V and 72 hours after the start of the measurement the OCV was -0.12 V. The figure shows how by conducting a positive current of 5 mA a positive potential of around +0.14 V on average was obtained (indicating charging of a system). Based on the C-rating of 4 mC and the 36 hour duration this should have charged the system to at least 15% SoC, if electrochemical reactions would have been happening. However, during the relaxation period of an hour a fast potential drop can be seen from 0.2 V to -0.09 V, interrupted by a discharge command at -1 mA which was immediately cancelled due a negative potential (as a negative current and negative potential would not mean discharging of the system). The second relaxation period then brings the potential gradually further down to -0.12 V.

From these results it is concluded that no electrochemical transfer of electrons has taken place, but instead polarization of OH^- and K^+ ions resulted in the shown potential during the charge period. Moreover, if the system would be electrochemically charged conform Eq. 1, one would expect a required potential above 0.63 V instead of the shown 0.14 V, as well as an OCV in that order of magnitude. More specifically, the intermixture of adsorption of OH^- ions to KB particles in the $Mn(OH)_2$ SSE suspension and the adsorption of K^+ ions to KB particles in the FeOOH SSE suspension is an explanation for the observed behaviour. This is in line with the behaviour during the relaxation period: As soon as the current was released the system decided to go to the most stable state and since the active material did not change in oxidation state or composition, the most stable state is realised by the release of the weak adsorbed bonds of the OH^- and K^+ ions. The speed of this release degressively takes place as the driving force (the potential difference with respect to the stable state) decreases.

A final attempt for electrochemically charging and discharging the system was done using identical newly prepared suspensions which showed the same open circuit voltage of -0.2 V at the starting state (SoC_0=0%). However, instead of applying a galvanostatic charge at 5mA, resulting in a potential of +0.14V, a potentiostatic charge of +1.2V was applied for 24 hours (Figure 41). This value is well above the theoretically required 0.63 V needed to charge the system, and just below the theoretical value at which electrolysis of water occurs. In other words, íf the proposed system works, the chance of electrochemical conversion would now have been maximized within the theoretical boundaries of electrolysis. The results in Figure 41 show that the applied potential of 1.2 V results in charging a system with a decreasing current from 25 mA to ~0 mA over the duration of 8 hours. After this, although 1.2V is applied over the remaining 16 hours, no current is apparent, indicating a steady-state condition. During the subsequent hour of relaxation an immediate potential drop is observed followed by a more gradual one that moves towards -0.1 V (similar as previous measurement). This indicates once more, that no electron transfer occurred from the $Mn(OH)_2$ into the FeOOH, but that polarisation of the electrodes occurred due to ion adsorption. The following discharge command of -1 mA is thus practically a charge command in the other direction, since the potential is also negative over the entire duration (the Autolab cut-off mechanism < 0 V was in this case excluded). The final hour of relaxation again shows an instant potential drop and shows that the system potential remains negative, but instead of moving towards -0.12 V, the system stabilises at -0.06 V.

The results thus show a full functioning circuit of the SSRFB, but not the proposed electrochemical activity. Furthermore, a large discrepancy between the expected OCV and experimental OCV was found (0.8 V difference and opposite polarity). However, the results don’t provide information on where the discrepancy comes from. Also, these results do not provide information on the quality of the SSE suspensions and the electroactive material individually. It merely shows that the combination of the proposed manganese and iron hydroxide SSE suspensions results in a starting OCV of |0.2 V| that decreased to an OCV between |0.12 V| and |0.06 V| over the duration of 72 hours (considered inadequate for proper battery operation). The following two sections therefore discuss the results of the further analysis of the FeOOH and $Mn(OH)_2$ SSE suspensions, while individually tested versus a zinc or copper electrode and separated by a salt bridge.

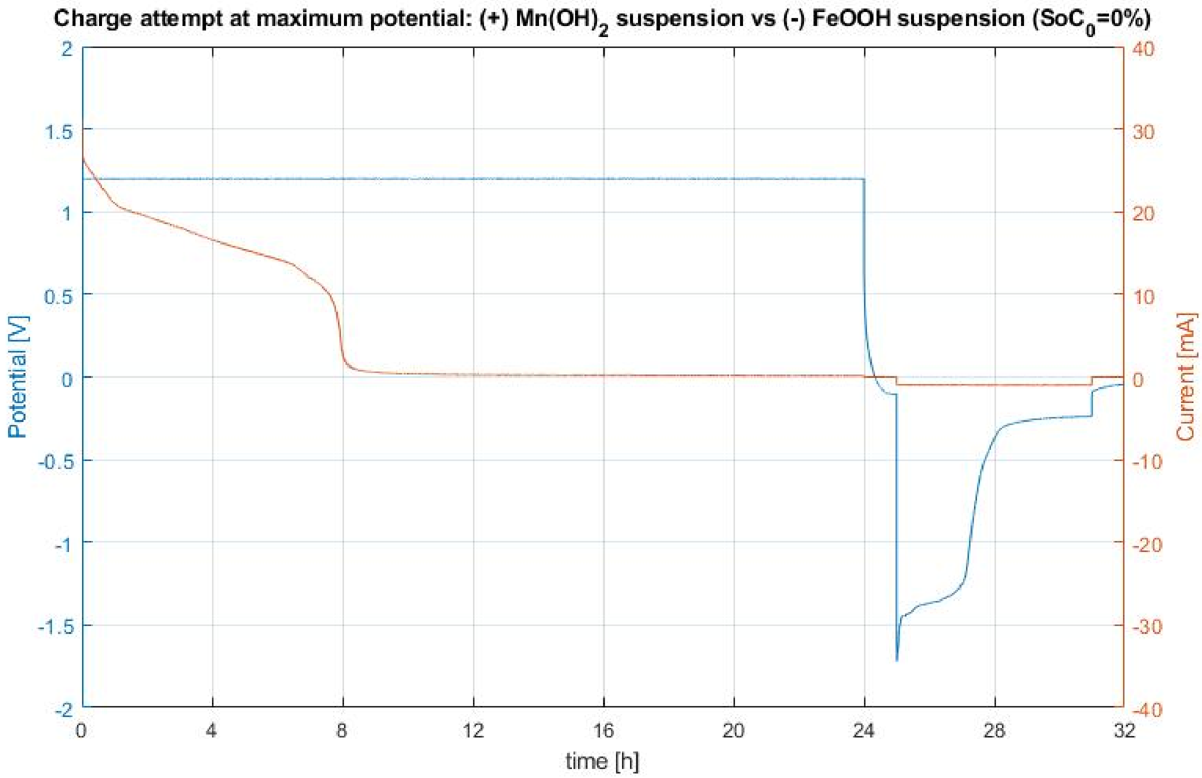

Figure 41: Charge attempt at maximum charge potential: (+) 6/2-ALG/22.2-Mn/69.8-5M versus (-) 8/2-ALG/22.2-Fe/67.8-5M (SoC_0=0%). First 24 hours potentiostatic charging at 1.2V, then 1 hour relaxation (I = 0 A), then 6 hours galvanostatic discharge at -1 mA (no cut-offs applied), finalised by another hour of relaxation (I = 0 A).

4.4.2. FeOOH – Zn System

Multiple (+) FeOOH SSE suspensions were tested versus a (-) solid Zn electrode in 1M Zn^{2+} electrolyte, separated by a salt bridge. Galvanostatic cycling results show that the FeOOH SSE suspension can be electrochemically discharged and charged, which is further substantiated by brown mass transfer through the salt bridge (Figure 42). From the results also follows that optimization of the effectivity of the FeOOH SSE suspensions involves a balance between colloidal stability, viscosity, ionic conductivity, electronic conductivity and the electrical double layer. The results further suggest that a significantly more complicated equilibrium system of iron in water is apparent than initially expected, indicated by a half-cell potential difference of 0.55 V between the expected value (according to Eq. 3 in a 5M KOH environment) and the measured value using an Ag/AgCl reference electrode.

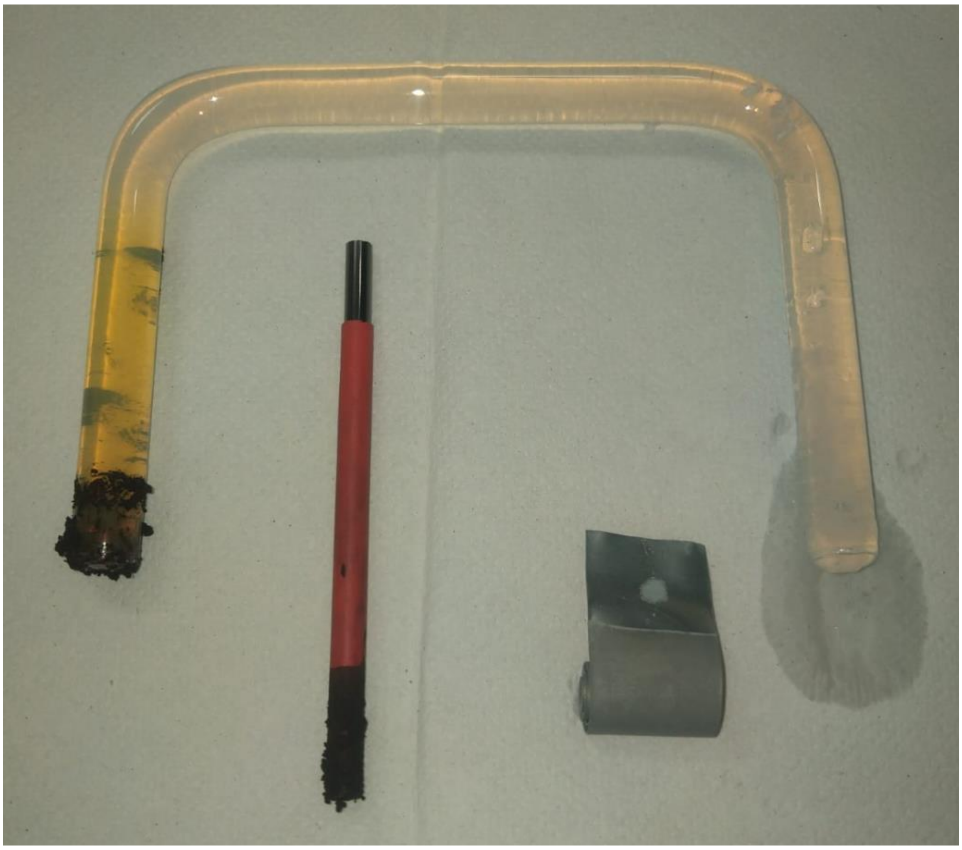

Figure 42: Salt bridge and current collectors after cycling procedure: light brown mass transfer (SSE sample) into salt bridge and oxidation of Zn electrode observed.

When considering the performance of different FeOOH SSE suspensions, the best results were found for the 8/0.2-PAA/4.4-Fe/87.4-5M SSE suspension, which showed an average system efficiency of 62.9% when cycling at 1 mC over a DoD of 1%. The amount of zinc and Zn^{2+} was over-dimensioned greatly so that the amount of FeOOH was decisive in DoD and C-rate determination (the same was done for $Mn(OH)_2$ versus with copper and Cu^{2+} in the next chapter). In absolute sense 1 mC corresponded to a current of 0.268 mA for the SSE suspension holding 10 mmol FeOOH (4.4 wt%). Cycling at 4 mC was demonstrated to be possible for SSE suspensions holding 10 mmol FeOOH, but not for the one holding 50 mmol FeOOH (22.2 wt%). A summary of the efficiencies at different C-rates are given in Table 6. An overview of cycling procedure results can be found in Appendix J, of which an overview of the most interesting ones are depicted in Figure 43. Additionally, it was found that the charge overpotentials were significantly higher than the discharge potential losses at all C-rates (Table 7).

Table 6: Overview of FeOOH SSE Suspensions tested over 1% DoD for various C-rates.

SSE Suspension	**DoD [%]**	**C-rate**	**Efficiency [%]**	**C-rate**	**Efficiency [%]**
8/0.2-PAA/4.4-Fe/87.4-5M	1	1 mC	62.9	4 mC	18.2
8/2-ALG/4.4-Fe/85.6-5M	1	1 mC	53.0	4 mC	24.9
8/2-ALG/22.2-Fe/67.8-5M	1	1 mC	22.4	4 mC	-

Table 7: Overview of average overpotentials for FeOOH SSE Suspensions.

SSE Suspension	**V_{ref} [V]**	**C-rate**	**Overpotential Charge [V]**	**Potential Loss Discharge [V]**
8/0.2-PAA/4.4-Fe/87.4-5M	0.65	1 mC	+0.22	-0.10
8/0.2-PAA/4.4-Fe/87.4-5M	0.65	4 mC	+0.57	-0.43
8/2-ALG/4.4-Fe/85.6-5M	0.62	1 mC	0.33	-0.12
8/2-ALG/4.4-Fe/85.6-5M	0.62	4 mC	0.54	-0.33
8/2-ALG/22.2-Fe/67.8-5M	0.67	1 mC	+0.58	-0.39

By comparing the results from Figure 43, Table 6 and Table 7, it is found that PAA is a better choice for emulsifier as illustrated by the higher energy efficiency of 62.9% compared to 53.0% for ALG for similar SSE suspensions. Through this, an overall connection becomes apparent that optimization of the colloidal stability and the conductive network also results in better electrochemical activity. This is believed to be attributed to higher reaction kinetics as a result of (a combination of) a higher electric conductivity, a better reachability between the KB network and active FeOOH particles and a more homogeneous preparation of SSE suspensions. However, when additionally comparing the amount of active material in a suspension it follows that 50 mmol FeOOH in the SSE suspension (22.2 wt%), shows worse performance than 10 mmol FeOOH (4.4 wt%), illustrated by the higher energy efficiency of 10 mmol FeOOH at a C-rate of 1 mC and the fact that cycling at 4 mC was not possible for the 50 mmol FeOOH SSE suspension while this was possible for the 10 mmol suspension. This is striking, since the SSE suspension holding 50 mmol FeOOH has a higher kb% $w_{kb}/w_{solution}$ (11.5% vs 9.2%), a lower electric resistance (290 Ω vs 318 Ω) and a larger amount of active material (22.2 wt% vs 4.4 wt%). A possible explanation for this is that the structure of the electric double layer changes due to a significantly increased ratio of solid particles versus 5M KOH solution (the ratio solid wt% particles over wt% 5M KOH solution increased from 1:6 to 1:2). With an increased amount of solid materials in the SSE suspensions the overall surface area exposed to the ionic environment increases too. This difference in exposure to leads to a difference in electrical double layer structure between the two SSE suspensions. Earlier research shows a significant correlation between the kinetics of a reaction and the structure of the electrical double layer (Timmer & Sluyters, 1969). More specifically, the same research shows a relationship of the structure of the electrical double layer to adsorption of supporting electrolyte, adsorption of electroactive species and adsorption of electro inactive species to solid particles in the suspension.

At the high SoC at which the cycling experiments were done the dominant source for overpotential are kinetic activation losses (Aaron, Tang, Papandrew, & Zawodzinski, 2011). The low achievable C-rates (i.e. low reaction kinetics) are thus suspected to be either a result of slow transfer of electrons from KB into/out of the active material or slow ion (de)-intercalation in the active material (Ciobanu et al., 2007). In the end this all comes down once more to the structure of the electrical double layer. To this regard the battolyser offers a great reference to this system, as it is based on Fe/$Fe(OH)_2$ and $Ni(OH)_2$/NiOOH active materials in a 5M KOH environment, however they are possible to apply a C-rates orders of magnitudes higher (Mulder, Weninger, Middelkoop, Ooms, & Schreuders, 2017). The biggest difference with respect to reaction kinetics comes the structure of the electrodes (solid versus suspension electrodes). Now, consider two electrodes of an equal mass, one being a standard solid electrode and one being a suspension electrode. The consequence of using suspension electrodes is that the electrode/electrolyte interface area significantly increases (similar as in the previous paragraph concerning 10 mmol and 50 mmol active material). As a result, the overall negative influence of the electrical double layer in this system is larger and unwishful adsorption mechanisms are present at a larger scale, leading to more kinetic activation losses (Aaron et al., 2011). This is in accordance with the significantly higher achievable C-rate of the battolyser as well as the discussion in the previous paragraph.

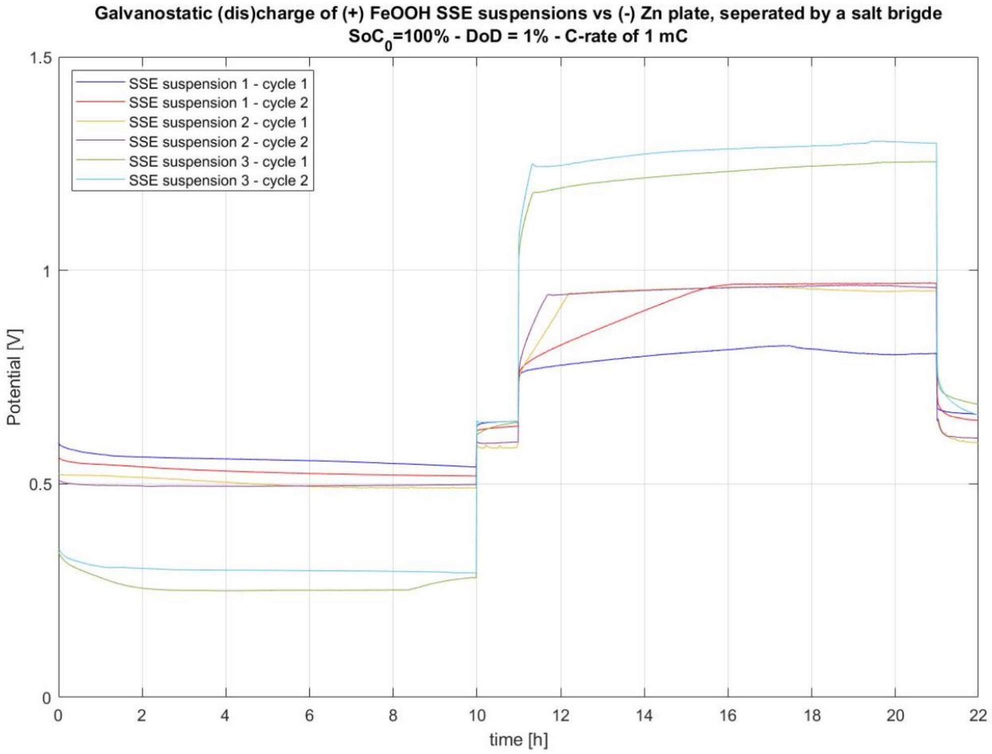

Figure 43: Comparing galvanostatic (dis)charging of FeOOH SSE suspensions. at a C-rate of 1 mC: (i) 8/0.2-PAA/4.4-Fe/87.4-5M, (ii) 8/2-ALG/4.4-Fe/85.6-5M, (iii) 8/2-ALG/22.2-Fe/67.8-5M. The average cycling efficiencies are (i) 62.9%, (ii) 53.0% and (iii) 22.4%.

Although the applicable C-rate of the system is low, high currents can be obtained by simply scaling the system. If one would obtain a cell voltage of 1.0 V using a different counter electrode versus the FeOOH SSE suspension, a 1 MW system could be acquired when cycling at 1 mC by scaling the 8/0.2-PAA/4.4-Fe/87.4-5M SSE suspension by a factor 3.73×10^9. Considering the current sample had a weight of 20 grams, a 1 MW version would have a weight of around 74.6×10^6 kg. The volume of the sample was around 25 ml (density of ~800 kg/m^3), so the volume of such a half-cell would be around 93.3×10^3 m^3. This roughly equals the volume of 37 Olympic swimming pools or 5 football fields having a depth of 4 meters. The charge this amount of active material holds is 1 GAh, purely based on the FeOOH SSE suspension and assuming 100% utilization of active material. Assuming a 1.0 V cell potential the half-cell FeOOH SSE suspension then has an energy density of 13.4 Wh/kg. This moderately low energy density can easily be overcome by adding more active material. However, as the results have shown, a fivefold higher amount of FeOOH (22.2 wt% vs 4.4 wt%) comes significantly at the expense of energy efficiency at similar C-rates.

Following from the large difference in measured and theoretical OCV of the $Mn(OH)_2$-FeOOH SSRFB (Chapter 4.4.1), the half-cell potential of the FeOOH SSE suspension was investigated by using an Ag/AgCl reference electrode in the setup of this section. It was found that the OCV of the FeOOH SSE suspension versus the Ag/AgCl electrode was -0.18 V. Taking into consideration that the half-cell potential of the Ag/AgCl electrode is 0.21 V vs SHE (“Reference Electrode Potentials,” 2016), the half-cell potential for the FeOOH SSE suspension results to be +0.03 V, which is much higher than the theoretically expected -0.52 V. Similar OCV values were found after the comparing the OCV between a) FeOOH SSE suspension versus the zinc electrode to b) a solid pressed FeOOH electrode in a 5M KOH environment versus the zinc electrode (Appendix E). The similarity in OCV when comparing a configuration using a FeOOH solid electrode to a configuration using a FeOOH SSE suspension further reinforces that the FeOOH SSE suspension in itself is functional.

This difference between the proposed and measured FeOOH half-cell potential is believed to be the result of a considerably more complex thermodynamic equilibrium system of iron in water at highly alkaline conditions ($14 < pH < 15$) than assumed in Eq. 3. Literature on this matter mentions, for example, the existence of solid species such as Fe_2O_3, $Fe(OH)_3$, $Fe(OH)_2$, Fe_3O_4 and at the same time ionic species such as $HFeO_2^-$, $Fe(OH)_4^-$ and FeO_4^{2-} (“Interview with B. Weninger,” 2020; Pourbaix et al., 1997; J. Zhang et al., 2018)(Appendix D for Pourbaix diagrams). This increases the amount of possible (local) equilibria substantially. Although it is concluded that a different equilibrium mechanism is most likely dominant in the environment during this thesis, leading to a different half-cell potential, further specification of which equilibrium is active lies outside the scope of this research. Additional research specifically dedicated to the stability of FeOOH in water at high alkalinity is required in order to be able to comment on the exact electrochemical reactions that are apparent in this system. The possible existence of Fe-ion species further indicates that the use of simple microfiltration membranes may not be sufficient using this specific SSE suspension, as cross-over of these ion species will not be prevented, leading to the degradation of the SSRFB.

4.4.3. Mn(OH)2 – Cu System

The (+) Cu electrode in 1.25M Cu^{2+} electrolyte was tested versus various (-) $Mn(OH)_2$ SSE suspensions, separated by a salt bridge. The results show that the $Mn(OH)_2$ SSE suspension can also be electrochemically discharged and charged. This is additionally qualitatively substantiated by mass transfer of coloured brown and blue ions through the salt bridge (Figure 44). However, the results also show that the $Mn(OH)_2$ system is instable in aerobic environments, following by a significant drop in OCV and overwhelming qualitative evidence. Additionally, very similar to that of the iron system, the chemical equilibrium of $Mn(OH)_2$ in highly alkaline environments seems to be dependent of more equilibria than assumed in Eq. 2, leading to a discrepancy between the proposed and measured half-cell potential.

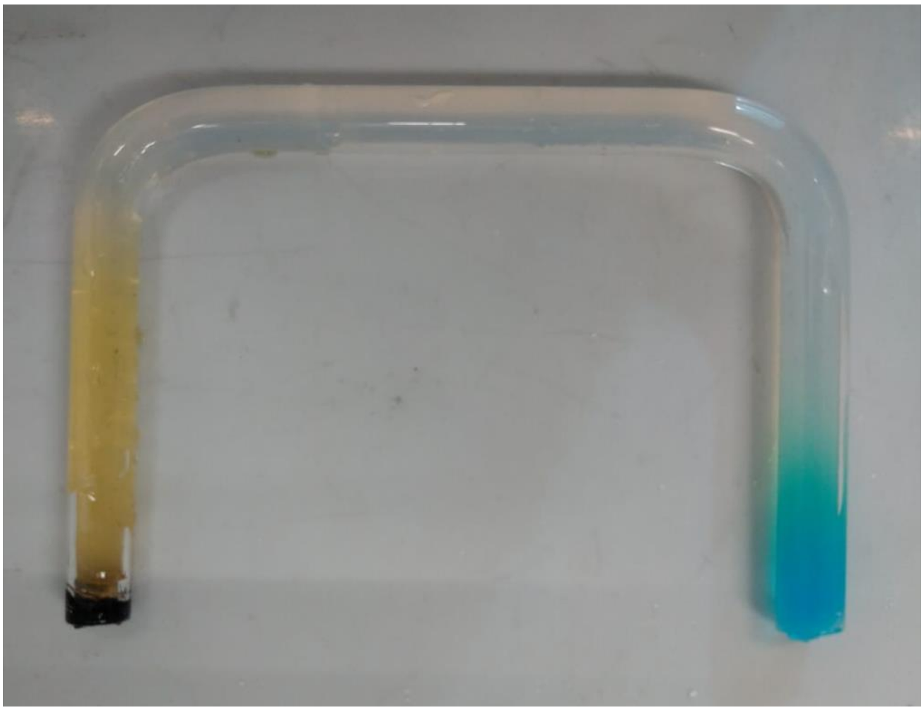

Figure 44: Salt bridge after cycling procedure: light brown mass transfer (SSE sample) and light blue mass transfer (Cu^{2+}) into salt bridge observed.

When considering Figure 45, it can be observed that quick degradation of the SSE samples occurred. Within 72 hours an OCV drop was observed from 0.53 V to 0.32 V for the $Mn(OH)_2$ suspension holding ALG and a drop from 0.55 V to 0.30 V for the $Mn(OH)_2$ SSE holding PAA. This drop is believed to be accounted to the instability of the $Mn(OH)_2$ species in an aerobic environment (reinforced by the fact that both the weight of the copper electrode and the dissolved Cu^{2+} were over-dimensioned heavily with respect to the DoD on which was cycled and the influence of change in Cu^{2+} ions can therefore be neglected). Above all, quick degradation of $Mn(OH)_2$ in aerobic environments is in line with literature (Anandan et al., 2013) and in line with observations of quick darkening of samples during this thesis. For this reason synthesis normally happens in an oxygen free environment and the same can expected for proper the use the material.

Nonetheless, the results in Table 8 and Figure 45 show that the $Mn(OH)_2$ SSE suspensions could be discharged and charged. Very comparable results were found for the suspension using ALG and the suspension using PAA. They showed very similar energy efficiencies and could both only be discharged at 1 mC (an overview of cycling procedures can be found in Appendix J). The most important mechanisms, which concern SSE suspensions in general, have been dealt with in previous chapter with respect to the iron active material and are considered to be comparable for this SSE suspension. Discussion on the difference in composition of $Mn(OH)_2$ SSE samples and the effect on the SSE performance is excluded due to the high instability and inconsistent character of the $Mn(OH)_2$ SSE suspension samples (Figure 45).

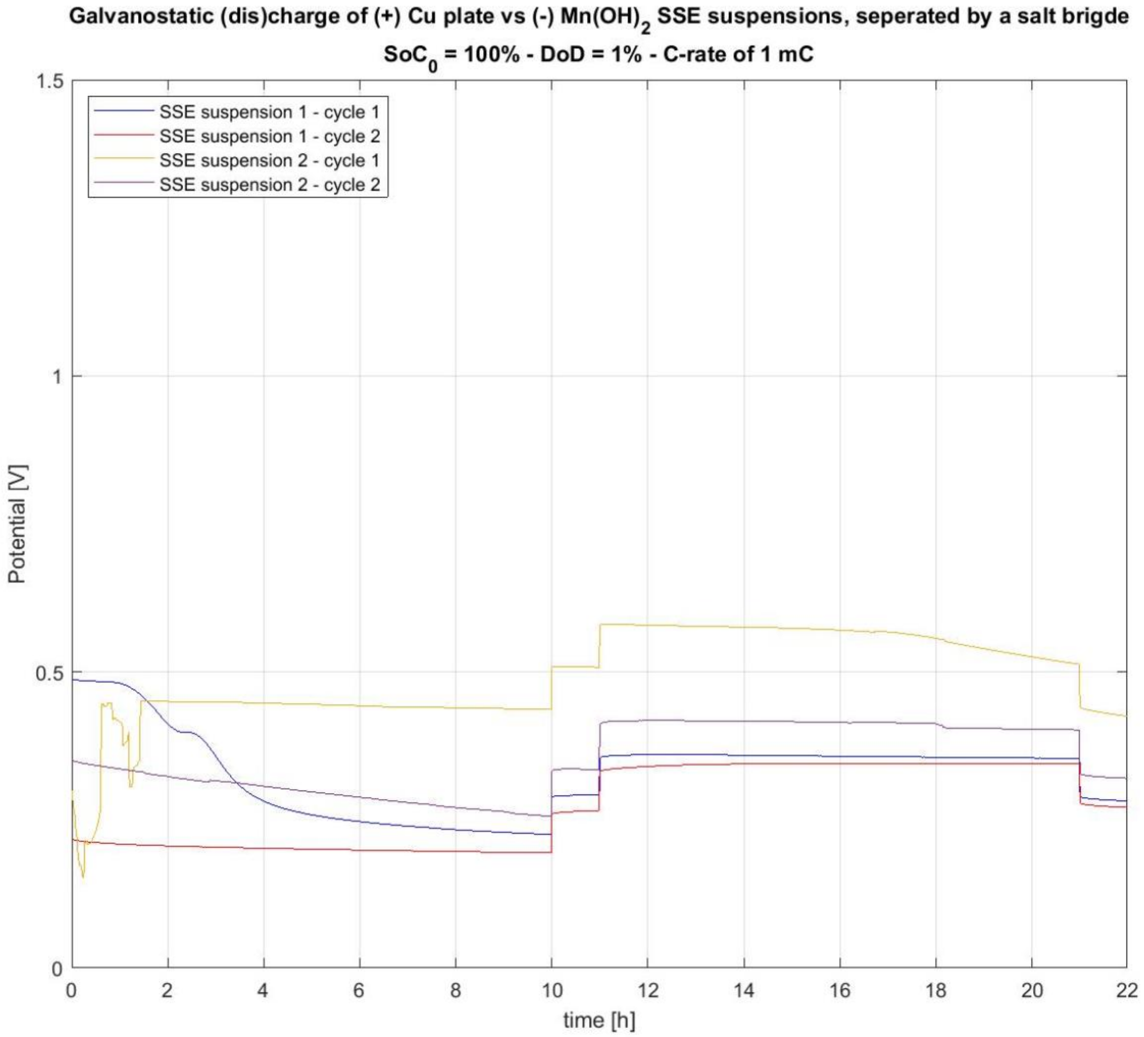

Figure 45: Comparing $Mn(OH)_2$ SSE suspensions: (i) 6/0.2-PAA/4.4-Mn/89.4-5M, (ii) 6/2-ALG/4.4-Mn/87.6-5M.

Table 8: Overview of $Mn(OH)_2$ SSE Suspensions tested over 1% DoD for various C-rates.

SSE Suspension	**DoD [%]**	**C-rate**	**Efficiency [%]**	**C-rate**	**Efficiency [%]**
6/0.2-PAA/4.4-Mn/89.4-5M	1	1 mC	73.0	4 mC	-
6/2-ALG/4.4-Mn/87.6-5M	1	1 mC	74.4	4 mC	-

Regarding the E_{cell} of the $Mn(OH)_2$ SSE suspensions, it was found via the use of the Ag/AgCl reference electrode that this equalled -0.16 V vs SHE instead of the theoretically expected +0.11 V vs SHE. The significant difference of 0.27 V originates, very similar as for the FeOOH species, from the much more complex equilibrium system of manganese in a highly alkaline environment. To this regard, solid species like $Mn(OH)_3$, $Mn(OH)_2$, MnO_2, Mn_2O_3 and Mn_3O_4 and ionic species such as $HMnO_2^-$ and MnO_4^- are mentioned and their equilibria should be taken into consideration (Hem, 1963; Pourbaix et al., 1997) (Appendix D for Pourbaix diagrams). Note how possible ionic active species such as $HMnO_2^-$ in the highly alkaline environment would have to be ruled out in order to properly justify using a microfiltration membrane in a SSRFB setup together with this SSE suspension.

To finalise this chapter, observe how the difference for the found values for E_{cell} between the FeOOH SSE suspension and the $Mn(OH)_2$ SSE suspension using the Ag/AgCl reference electrode, only differ by 10 mV from the measured OCV value for the SSRFB configuration directly using the FeOOH SSE suspension versus $Mn(OH)_2$ SSE suspension (Figure 46). This furthermore confirms that the SSRFB system in general works, but that the choice of iron and manganese hydroxide materials in the highly alkaline environment is not adequate as these consistently result in the dominance of other electrochemical equilibria reactions than the ones on which this design has been founded (Eqs. 2 and 3).

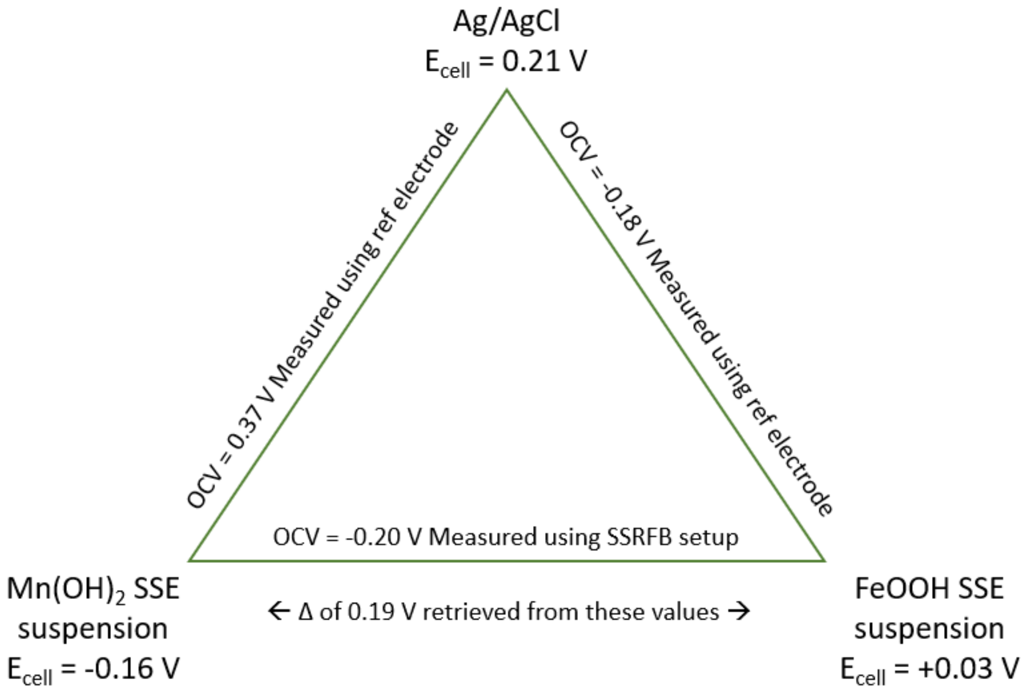

Figure 46: Comparison between the measured OCV using the full SSRFB system setup and the retrieved cell potentials by using an Ag/AgCl reference electrode (all E_{cell} values vs SHE).

5. Conclusion and Recommendations

To conclude, this chapter relates the initial research questions back to the key-findings of this thesis and shares recommendations for future research.

Main research question:

- Can a SSRFB be created using iron hydroxide versus manganese hydroxide using aqueous SSE suspensions?

Sub-research questions:

- Can both of the proposed SSE suspensions be separately charged and discharged, versus a known solid electrode?
- What is the influence of SSE composition on its electronic conductivity?
- What is the influence of SSE composition on its ionic conductivity?
- How are colloidally stable SSE suspensions created?
- How does the choice of type of membrane affect the system performance?
- What is the effectivity of the chosen active materials?

5.1. Key-Findings

This research concludes that it was not possible to effectively make a SSRFB based on FeOOH and $Mn(OH)_2$ SSE suspensions. It provides systematic proof that this can be attributed to the specific combination of the active materials in a highly alkaline environment, but that in itself, both the SSRFB configuration and SSE suspensions are functional. On the one hand, a complex chemical system of the active species consisting of multiple thermodynamic equilibria had the consequence that the open circuit cell voltage was 0.2 V instead of the expected 0.63 V, which was considered too low for proper cycling of a battery (especially as this OCV degraded to between 0.12 V and 0.06 V over a period of 72 hours). On the other hand, it was shown that both the FeOOH and the $Mn(OH)_2$ SSE suspension could be separately cycled versus respectively a solid zinc and copper electrode and that a cheap microfiltration membrane suffices in the design for a SSRFB. This shows that in general, cheap, safe and functioning SSE suspensions separated by a cheap microfiltration membrane in a SSRFB configuration are feasible, but not this specific combination in the highly alkaline environment.

Preparation and investigation of dozens of suspensions have shown that it is possible to create colloidally stable SSE suspensions with viscosities that are in the range of pasty to liquid. Using the correct amount of a suitable emulsifier is shown to be highly significant, both in respect to a) the balance between colloidal stability and viscosity, and b) optimization of electronic conductivity of the suspensions. Out of ALG, PVP and PAA, the latter appears to be the best choice of emulsifier in a highly alkaline environment.

It is further concluded, that within the boundaries of colloidal stability and viscosity, it is possible to create SSE suspensions that are both electronically and ionically conductive. However, within the highly alkaline environment (5M KOH), the ionic resistance of the SSE suspensions proves to be less of a challenge than the electrical resistance. The ionic resistance appeared to be insensitive towards the addition of solid particles (such as the emulsifier, KB and active materials) within the boundaries of viscosity. At the same time the electronic resistance was two orders of magnitude higher than the ionic resistance, even with KB addition significantly above percolation threshold.

A large advantage of the system in general is the flexibility with which membranes can be chosen (presuming ionic active species are not apparent in the system). Overall, this thesis demonstrates that all three considered membranes can be used in a SSRFB configuration and the best overall results were obtained using a simple filter paper membrane. In the SSRFB setup a minimal amount of solid particle crossover was observed through this membrane, while abiding to ionic conductivity of the membrane.

However, this thesis also establishes that in the tested system it cannot be ruled out that ionic active species do not exist. It was found that both the FeOOH and the $Mn(OH)_2$ active materials exist in many forms at high alkalinity and many other equilibria exist besides the one on which this thesis was founded. This is concluded from the electrochemical behaviour of FeOOH versus $Mn(OH)_2$ SSE suspensions in a SSRFB system, as well as by separately obtaining their cell potentials using an Ag/AgCl reference electrode. The latter was executed by testing a) the FeOOH SSE suspension versus a zinc electrode and b) the $Mn(OH)_2$ SSE suspension versus a copper electrode. For these experiments the electrodes were separated by a salt bridge to prevent electrode poisoning, instead of using the SSRFB setup. The cell potentials versus SHE were found to be 0.03 V for the FeOOH SSE suspension and -0.16 V for the $Mn(OH)_2$ SSE suspension.

From the experiments in which the FeOOH and $Mn(OH)_2$ SSE suspensions were tested in the SSRFB setup, it is concluded that the SSRFB setup itself works, but no electrochemical reactions occur within the SSE suspensions. This is evidenced by the adsorption of ions when applying a current in both directions, and the quick release of these when the current ceased. This proves that the problem does not lie within the ionic and electronic conductance of the SSE suspensions and that the filter paper membrane is ion conductive in the SSRFB setup.

It is then further concluded that the SSE suspensions themselves are functional too, because both the cheap FeOOH and the cheap $Mn(OH)_2$ SSE suspension can be electrochemically discharged and charged versus respectively a solid zinc and a solid copper electrode, while separated by a salt bridge. It was shown that cycling over a DoD of 1% and a C-rate of 1 mC resulted in energy efficiencies of 62.9% for the system holding the FeOOH SSE suspension and 74.4% for the system holding the $Mn(OH)_2$ SSE suspension. The maximum C-rate at which cycling was possible was 4 mC. The low C-rates are believed to be the result of slow reaction kinetics due to ion adsorption caused by an unfavourable structure of the electrical double layer in the highly alkaline environment of the SSE suspensions. These low C-rates do not pose a significant threat to the SSRFB technology, as higher absolute currents are easily achieved, simply by scaling of the SSE suspensions.

In sum, it is demonstrated that the aqueous SSRFB by its very nature is a suitable RFB technology in which cheap and safe materials can be used for large-scale energy storage. However, that the combination and optimization of the right active materials in the right environment proves to be fundamental for proper operation and is in fact a complex balance between electric and ionic conductivity, colloidal stability, viscosity and (electro)chemical stability.

5.2 Recommendations

Considering the selection of active species and pH environment, future research should focus on the stability region of active species in which less equilibria are apparent. This may very well still contain iron and manganese, but not the proposed iron and manganese hydroxides which were used during this research in such high alkaline environments.

Additionally, it is highly recommended that future research focuses on active species that can be confirmed to stay insoluble throughout the operation of the SSRFB. It is only then that one can truly justify the use of cheap microfiltration membranes. Future research should then also investigate whether cross-over of these insoluble particles through microporous membranes occurs, by using for example X-ray microscopy. In this research this was analysed by the naked eye, which leaves room for not identifying cross-over of particles smaller than visible with the naked eye. Moreover, this does not distinguish whether KB or active material crossed-over (the latter being a bigger problem). Note however, that the use of an extra buffer compartment between the SSE suspensions was already very effective in this thesis for preventing cross-over contamination, as cross-over through two membranes would have had to occur. Since already a minimal amount of (visible) solid particles crossed the first membrane, it is fair to assume that virtually no particles travelled to the other side of the middle compartment and crossed over through the second membrane.

As an optimization concerning the active materials in this thesis it is recommended to study the electrochemical behaviour of the SSE suspensions with significantly lower KOH concentrations, as this would a) lower the alkalinity and possibly provide better stability regions for the active material, b) possibly mitigate the formation of ions of active material and c) decrease the thickness of the electrical double layer thus improving the kinetics of the system (due to a decrease of the Debye-Hückel parameter). However, it has to be remembered that as a consequence the ionic conductivity and the zeta potential decrease too (the latter indicating lower colloidal stability). Decreasing these too much would impose new problems.

With respect to optimization of SSE suspension compositions in general, future research should additionally incorporate quantitative measurements of zeta potential, shear rate and shear stress in the design considerations. The next logical step would be to also incorporate the effects of flow operation of the system and investigate its relationship to both the composition and effectivity of the SSE suspensions.

The low applicable C-rates during this research did not allow for the SSE suspensions to be cycled deeply due to time constraints. However, execution of deep cycles is important and recommended as it gives information on active material utilisation. In the end, justifying the use of cheap materials goes hand in hand with the amount of active material that can be utilised during a full cycle. It is evident that using a 10 times cheaper material of which only 10% can be utilised has zero net result from a cost per kWh perspective of the active material.

It is heavily suspected that the low C-rates are primarily the result of the specific composition of the SSE suspensions in the highly alkaline environment, but future research should additionally test the influence of the area of the current collectors with respect to volume of SSE sample on the applicable C-rate. If a predominantly insensitive relationship can be found, this is further confirmation that the SSE suspension composition is leading in the kinetics and would additionally provide useful knowledge on how to design a next SSRFB (if one wants to implement flow application, a new design has to be made anyway, since the current design using the glass elbows tubes can only be used for stationary measurements).

Regarding the measurement techniques, it would have been more time efficient to use potentiostatic instead of galvanostatic measurements to retrieve the electronic conductivity of the SSE suspensions. An occurring problem was that the potential during the galvanostatic measurement went out of bounds (higher than 1.2 V). The measurement then had to be redone on a lower current to remain within the potential limits of the aqueous SSE suspension. A potentiostatic measurement at for example 1 V would have always worked for retrieving the electronic conductivity (as long as a constant current is achieved so that Ohm’s law can be applied). It is further recommended (for these SSE suspensions) to execute EIS measurements over a larger frequency range with lower frequencies than the 100 mHz as done during this thesis. Low enough frequencies would have allowed for the SSE suspensions to show Ohmic behaviour, allowing for a second touchdown with the real impedance axis. The complete EIS measurements can then additionally be used to gain more information on for example electronic conductivity, the charge-transfer resistance and ion transfer limitations.

Finally, it is advised to work in a more controlled measurement environment. More specifically, for this research it would have been especially helpful to work in anaerobic conditions, as it was found that $Mn(OH)_2$ oxidizes very quickly when brought in contact with air. In addition, a more explicitly geometrically defined measurement setup would make the investigation of the effects of SSE composition with respect to electronic and ionic conductivity more robust. The same holds for the investigation of the effects of cycling at different C-rates using the full SSRFB system setup (setup 1).

Bibliography

Aaron, D., Tang, Z., Papandrew, A. B., & Zawodzinski, T. A. (2011). Polarization curve analysis of all-vanadium redox flow batteries. *Journal of Applied Electrochemistry*, *41*(10), 1175–1182. https://doi.org/10.1007/s10800-011-0335-7

Adamczyk, Z. (2013). *Encyclopedia of Colloid and Interface Science*. *Encyclopedia of Colloid and Interface Science*. https://doi.org/10.1007/978-3-642-20665-8

Anandan, S., Gnana Sundara Raj, B., Lee, G. J., & Wu, J. J. (2013). Sonochemical synthesis of manganese (II) hydroxide for supercapacitor applications. *Materials Research Bulletin*, *48*(9), 3357–3361. https://doi.org/10.1016/j.materresbull.2013.05.021

Basics of electrochemical impedance spectroscopy. (2020). Retrieved from https://www.gamry.com/application-notes/EIS/basics-of-electrochemical-impedance-spectroscopy/

Beverskog, B. (1996). Revised Diagrams for Iron At 25-300 ° C. *Science*, *38*(12), 2121–2135. https://doi.org/10.1038/NMETH.1311

Biendicho, J. J., Flox, C., Sanz, L., & Morante, J. R. (2016). Static and dynamic studies on LiNi1/3Co1/3Mn1/3O2-based suspensions for semi-solid flow batteries. *ChemSusChem*, *9*(15), 1938–1944. https://doi.org/10.1002/cssc.201600285

Chen, R., Kim, S., & Chang, Z. (2017). Redox Flow Batteries: Fundamentals and Applications. *Redox - Principles and Advanced Applications*. https://doi.org/10.5772/intechopen.68752

Cheng, J., Zhang, L., Yang, Y. S., Wen, Y. H., Cao, G. P., & Wang, X. D. (2007). Preliminary study of single flow zinc-nickel battery. *Electrochemistry Communications*, *9*(11), 2639–2642. https://doi.org/10.1016/j.elecom.2007.08.016

Cheng, Y., Zhang, H., Lai, Q., Li, X., Shi, D., & Zhang, L. (2013). A high power density single flow zinc-nickel battery with three-dimensional porous negative electrode. *Journal of Power Sources*, *241*, 196–202. https://doi.org/10.1016/j.jpowsour.2013.04.121

Cho, K. T., Ridgway, P., Weber, A. Z., Haussener, S., Battaglia, V., & Srinivasan, V. (2012). High Performance Hydrogen/Bromine Redox Flow Battery for Grid-Scale Energy Storage. *Journal of The Electrochemical Society*, *159*(11), A1806–A1815. https://doi.org/10.1149/2.018211jes

Ciobanu, M., Wilburn, J. P., Krim, M. L., & Cliffel, D. E. (2007). Fundamentals. In *Handbook of Electrochemistry*. https://doi.org/10.1016/B978-0-444-51958-0.50002-1

Cunha, Á., Martins, J., Rodrigues, N., & Brito, F. P. (2014). Vanadium redox flow batteries: a technology review. *International Journal of Energy Research*, *39*, 889–918. https://doi.org/10.1002/er.3260

Dai, H., Jiang, B., & Wei, X. (2018). Impedance characterization and modeling of lithium-ion batteries considering the internal temperature gradient. *Energies*, *11*(1). https://doi.org/10.3390/en11010220

Dinkgreve, M. (2019). *The Rheology of Jamming*.

Duduta, M., Ho, B., Wood, V. C., Limthongkul, P., Brunini, V. E., Carter, W. C., & Chiang, Y. M. (2011). Semi-solid lithium rechargeable flow battery. *Advanced Energy Materials*, *1*(4), 511–516. https://doi.org/10.1002/aenm.201100152

Enexis Netbeheer. (2020). Transportschaarste Enexis. Retrieved from https://www.enexis.nl/zakelijk/duurzaam/beperkte-capaciteit/gebieden-met-schaarste

Gilliam, R. J., Graydon, J. W., Kirk, D. W., & Thorpe, S. J. (2007). A review of specific conductivities of potassium hydroxide solutions for various concentrations and temperatures. *International Journal of Hydrogen Energy*, *32*(3), 359–364. https://doi.org/10.1016/j.ijhydene.2006.10.062

Greenwood, R., & Kendall, K. (1999). Selection of Suitable Dispersants for Aqueous Suspensions of Zirconia and Titania Powders using Acoustophoresis. *Journal of the European Ceramic Society*, *19*(4), 479–488. https://doi.org/10.1016/s0955-2219(98)00208-8

Greenwood, R., & Kendall, K. (2000). Acoustophoretic studies of aqueous suspensions of alumina and 8 mol% yttria stabilised zirconia powders. *Journal of the European Ceramic Society*, *20*(1), 77–84. https://doi.org/10.1016/s0955-2219(99)00091-6

Hem, J. D. (1963). Chemical equilibria affecting the behavior of manganese in natural water. *International Association of Scientific Hydrology. Bulletin*, *8*(3), 30–37. https://doi.org/10.1080/02626666309493334

Hurd, A. J., Kelley, R. L., Eggert, R. G., & Lee, M. H. (2012). Energy-critical elements for sustainable development. *MRS Bulletin*, *37*(4), 405–410. https://doi.org/10.1557/mrs.2012.54

Interview with B. Weninger. (2020).

Kong, L., Li, C., Jiang, J., & Pecht, M. G. (2018). Li-ion battery fire hazards and safety strategies. *Energies*, *11*(9), 1–11. https://doi.org/10.3390/en11092191

Kumar, S., & Jayanti, S. (2016). Effect of flow field on the performance of an all-vanadium redox flow battery. *Journal of Power Sources*, *307*, 782–787. https://doi.org/10.1016/j.jpowsour.2016.01.048

Lead, F. (2008). Development of semi-solid alkaline flow battery-support.

Léonard, A. F., & Job, N. (2019). Safe and green Li-ion batteries based on LiFePO 4 and Li 4 Ti 5 O 12 sprayed as aqueous slurries with xanthan gum as common binder. *Materials Today Energy*, *12*, 168–178. https://doi.org/10.1016/j.mtener.2019.01.008

Leslie, J. (1989). *Physicochemical Principles of Pharmacy*. *American Journal of Health-System Pharmacy* (Vol. 46). https://doi.org/10.1093/ajhp/46.8.1678

Leung, P., Li, X., Ponce De León, C., Berlouis, L., Low, C. T. J., & Walsh, F. C. (2012). Progress in redox flow batteries, remaining challenges and their applications in energy storage. *RSC Advances*, *2*(27), 10125–10156. https://doi.org/10.1039/c2ra21342g

Li, Z., Smith, K. C., Dong, Y., Baram, N., Fan, F. Y., Xie, J., … Chiang, Y. M. (2013). Aqueous semi-solid flow cell: Demonstration and analysis. *Physical Chemistry Chemical Physics*, *15*(38), 15833–15839. https://doi.org/10.1039/c3cp53428f

Li, Z., Weng, G., Zou, Q., Cong, G., & Lu, Y. C. (2016). A high-energy and low-cost polysulfide/iodide redox flow battery. *Nano Energy*, *30*(August), 283–292. https://doi.org/10.1016/j.nanoen.2016.09.043

Lide, D. R. (2010). *CRC Handbook of Chemistry and Physics 90th edition*. Retrieved from http://www.ncbi.nlm.nih.gov/pubmed/3841419

Linnenbom, V. J. (1958). The Reaction Between Iron and Water in the Absence of Oxygen. *Journal of The Electrochemical Society*, *105*(6).

Ma, D., Hu, B., Wu, W., Liu, X., Zai, J., Shu, C., … Liu, T. L. (2019). Highly active nanostructured CoS2/CoS heterojunction electrocatalysts for aqueous polysulfide/iodide redox flow batteries. *Nature Communications*, *10*(1). https://doi.org/10.1038/s41467-019-11176-y

MacDonald, D. D. (2006). Reflections on the history of electrochemical impedance spectroscopy. *Electrochimica Acta*. https://doi.org/10.1016/j.electacta.2005.02.107

Mei, B. A., Munteshari, O., Lau, J., Dunn, B., & Pilon, L. (2018). Physical Interpretations of Nyquist Plots for EDLC Electrodes and Devices. *Journal of Physical Chemistry C*, *122*(1), 194–206. https://doi.org/10.1021/acs.jpcc.7b10582

Metal Prices. (2018). Retrieved from https://www.metalary.com/

Mohammadzadeh Kakhki, R. (2019). A review to recent developments in modification of carbon fiber electrodes. *Arabian Journal of Chemistry*, *12*(7), 1783–1794. https://doi.org/10.1016/j.arabjc.2014.11.058

Mongird, K., Fotedar, V., Viswanathan, V., Koritarov, V., Balducci, P., Hadjerioua, B., & Alam, J. (2019). Energy storage technology and cost characterization report. *Pacific Northwest National Laboratory*, (July), 1–120. Retrieved from https://www.energy.gov/sites/prod/files/2019/07/f65/Storage Cost and Performance Characterization Report_Final.pdf

Mulder, F. M., Weninger, B. M. H., Middelkoop, J., Ooms, F. G. B., & Schreuders, H. (2017). Efficient electricity storage with a battolyser, an integrated Ni-Fe battery and electrolyser. *Energy and Environmental Science*, *10*(3), 756–764. https://doi.org/10.1039/c6ee02923j

Narayanan, A. (2020). *Towards Semi-Solid Flow Batteries*. University of Twente, Enschede, The Netherlands. https://doi.org/10.3990/1.9789036549639

Ohshima, H. (2013). Encyclopedia of Colloid and Interface Science. *Encyclopedia of Colloid and Interface Science*. https://doi.org/10.1007/978-3-642-20665-8

Oldenburg, F. J., Ouarga, A., Schmidt, T. J., & Gubler, L. (2019). Accelerated Stress Test Method for the Assessment of Membrane Lifetime in Vanadium Redox Flow Batteries. *ACS Applied Materials and Interfaces*, *11*(51), 47917–47928. https://doi.org/10.1021/acsami.9b15736

Ozoemena, K. I., & Kebede, M. (2016). *Next-Generation Nanostructured Lithium-Ion Cathode Materials: Critical Challenges for New Directions in R&D*. https://doi.org/10.1007/978-3-319-26082-2_1

Pan, J., Sun, Y., Cheng, J., Wen, Y., Yang, Y., & Wan, P. (2008). Study on a new single flow acid Cu-PbO2 battery. *Electrochemistry Communications*, *10*(9), 1226–1229. https://doi.org/10.1016/j.elecom.2008.06.008

Parant, H., Muller, G., Le Mercier, T., Tarascon, J. M., Poulin, P., & Colin, A. (2017). Flowing suspensions of carbon black with high electronic conductivity for flow applications: Comparison between carbons black and exhibition of specific aggregation of carbon particles. *Carbon*, *119*, 10–20. https://doi.org/10.1016/j.carbon.2017.04.014

Parekh, M. N., Rahn, C. D., & Archer, L. A. (2020). Controlling dendrite growth in lithium metal batteries through forced advection. *Journal of Power Sources*, *452*(October 2019), 227760. https://doi.org/10.1016/j.jpowsour.2020.227760

Pate, K., & Safier, P. (2016). Chemical metrology methods for CMP quality. In *Advances in Chemical Mechanical Planarization (CMP)* (pp. 1–325). https://doi.org/10.1016/B978-0-08-100165-3.00012-7

Pourbaix, M., Zhang, H., & Pourbaix, A. (1997). Presentation of an Atlas of chemical and electrochemical equilibria in the presence of a gaseous phase. *Materials Science Forum*, *251–254*, 143–148. https://doi.org/10.4028/www.scientific.net/msf.251-254.143

Qi, Z., & Koenig, G. M. (2017). Review Article: Flow battery systems with solid electroactive materials. *Journal of Vacuum Science & Technology B, Nanotechnology and Microelectronics: Materials, Processing, Measurement, and Phenomena*, *35*(4), 040801. https://doi.org/10.1116/1.4983210

Qin, Y. (2018). Seaweed Hydrocolloids as Thickening, Gelling, and Emulsifying Agents in Functional Food Products. In Y. Qin (Ed.), *Bioactive Seaweeds for Food Applications* (1st ed., pp. 136–151).

Reference Electrode Potentials. (2016). Retrieved from https://www.edaq.com/wiki/Reference_Electrode_Potentials

Rubio-Garcia, J., Kucernak, A., Zhao, D., Li, D. I., Fahy, K. F., Yufit, V., … Gomez-Gonzalez, M. (2018). Hydrogen / manganese hybrid redox flow battery (in press). *J. Phys. Energy*.

Rus, E. D., Moon, G. D., Bai, J., Steingart, D. A., & Erdonmez, C. K. (2016). Electrochemical Behavior of Electrolytic Manganese Dioxide in Aqueous KOH and LiOH Solutions: A Comparative Study. *Journal of The Electrochemical Society*, *163*(3), A356–A363. https://doi.org/10.1149/2.1011602jes

Saadi, K., Nanikashvili, P., Tatus-Portnoy, Z., Hardisty, S., Shokhen, V., Zysler, M., & Zitoun, D. (2019). Crossover-tolerant coated platinum catalysts in hydrogen/bromine redox flow battery. *Journal of Power Sources*, *422*(March), 84–91. https://doi.org/10.1016/j.jpowsour.2019.03.043

Schalenbach, M., Zeradjanin, A. R., Kasian, O., Cherevko, S., & Mayrhofer, K. J. J. (2018). A perspective on low-temperature water electrolysis - Challenges in alkaline and acidic technology. *International Journal of Electrochemical Science*, *13*(2), 1173–1226. https://doi.org/10.20964/2018.02.26

Skyllas-Kazacos, M., Kazacos, G., Poon, G., & Verseema, H. (2010). Recent advances with UNSW vanadium-based redox flow batteries. *INTERNATIONAL JOURNAL OF ENERGY RESEARCH*, *34*, 182–189. https://doi.org/10.1002/er.1658

Soloveichik, G. L. (2015). Flow Batteries: Current Status and Trends. *Chemical Reviews*, *115*(20), 11533–11558. https://doi.org/10.1021/cr500720t

Tadros, T. (2014). *Colloid and interface aspects of pharmaceutical science*. *Colloid and Interface Science in Pharmaceutical Research and Development*. Elsevier B.V. https://doi.org/10.1016/B978-0-444-62614-1.00002-8

Tennet. (2020). Ontwerpinvesteringsplan Net op land 2020 - 2029. *TenneT*. Retrieved from https://www.tennet.eu/fileadmin/user_upload/Company/Publications/Investeringsplannen/IP2020_NOL_201001.pdf

Tian, H., Gao, T., Li, X., Wang, X., Luo, C., Fan, X., … Wang, C. (2017). High power rechargeable magnesium/iodine battery chemistry. *Nature Communications*, *8*, 1–8. https://doi.org/10.1038/ncomms14083

Timmer, B., & Sluyters, J. H. (1969). B. timmer, *18*, 44–61.

van Loon, Gary; Duffy, S. (2011). (2011). *Environmental Chemistry - a global perspective* (3rd ed.). Oxford University Press.

Weber, A. Z., Mench, M. M., Meyers, J. P., Ross, P. N., Gostick, J. T., & Liu, Q. (2011). Redox flow batteries: A review. *Journal of Applied Electrochemistry*, *41*(10), 1137–1164. https://doi.org/10.1007/s10800-011-0348-2

Wei, T. S., Fan, F. Y., Helal, A., Smith, K. C., McKinley, G. H., Chiang, Y. M., & Lewis, J. A. (2015). Biphasic Electrode Suspensions for Li-Ion Semi-solid Flow Cells with High Energy Density, Fast Charge Transport, and Low-Dissipation Flow. *Advanced Energy Materials*, *5*(15), 1–7.

https://doi.org/10.1002/aenm.201500535

Xu, B., Oudalov, A., Ulbig, A., Andersson, G., & Kirschen, D. S. (2018). Modeling of lithium-ion battery degradation for cell life assessment. *IEEE Transactions on Smart Grid*, *9*(2), 1131–1140. https://doi.org/10.1109/TSG.2016.2578950

Yaroshevsky, A. A. (2006). Abundances of chemical elements in the Earth’s crust. *Geochemistry International*, *44*(1), 48–55. https://doi.org/10.1134/S001670290601006X

Zeng, Y. K., Zhao, T. S., An, L., Zhou, X. L., & Wei, L. (2015). A comparative study of all-vanadium and iron-chromium redox flow batteries for large-scale energy storage. *Journal of Power Sources*, *300*, 438–443. https://doi.org/10.1016/j.jpowsour.2015.09.100

Zeng, Y. K., Zhao, T. S., Zhou, X. L., Zou, J., & Ren, Y. X. (2017). A hydrogen-ferric ion rebalance cell operating at low hydrogen concentrations for capacity restoration of iron-chromium redox flow batteries. *Journal of Power Sources*, *352*, 77–82. https://doi.org/10.1016/j.jpowsour.2017.03.125

Zeng, Y. K., Zhou, X. L., An, L., Wei, L., & Zhao, T. S. (2016). A high-performance flow-field structured iron-chromium redox flow battery. *Journal of Power Sources*, *324*, 738–744. https://doi.org/10.1016/j.jpowsour.2016.05.138

Zhang, J., Sun, W., Niu, F., Wang, L., Zhao, Y., & Han, M. (2018). Atmospheric sulfuric acid leaching thermodynamics from metallurgical zinc-bearing dust sludge. *International Journal of Heat and Technology*, *36*(1), 229–236. https://doi.org/10.18280/ijht.360131

Zhang, S., Guo, W., Yang, F., Zheng, P., Qiao, R., & Li, Z. (2019). Recent Progress in Polysulfide Redox-Flow Batteries. *Batteries & Supercaps*, *2*(7), 627–637. https://doi.org/10.1002/batt.201900056

Appendices

Appendix A – Price per kWh of Idealised System

One mol of the reaction from Eq. 1 results in 96500 C by using Eq. 12:

$$Q = nFN = 1 * 96500 * 1 = 96500\ C \tag{29}$$

This equals 26.8 Ah per mol of reaction. By assuming a perfect reaction without losses this translates to 19.0 Wh, when using E^0_{cell} = 0.71 V. The MW of $Mn(OH)_3$ is 106.0 g/mol and the MW of $Fe(OH)_2$ is 89.9 g/mol. So for 1 kWh of storage one would need 5.6 kg of $Mn(OH)_3$ and 4.7 kg of $Fe(OH)_2$. Taking into consideration that 51.8 wt% of $Mn(OH)_3$ is the weight of Mn, this means that 2.9 kg of active Mn is apparent. Similarly, taking into consideration that 62.1 wt% of $Fe(OH)_2$ is weight the weight of Fe, this translates into 2.9 kg of active Fe. Now, for prices of $2060 per metric ton for manganese and $120 per metric ton for iron ("Metal Prices," 2018), it is fair to say that as a rough estimate $6,32 or €5.33 is required to store 1 kWh of energy (less than €6 per kWh).

Appendix B – Reported SSRFB Systems

Table 9: Reported SSRFB systems including electrical conductivity, active material, electrolytes and additives (Ozoemena & Kebede, 2016)

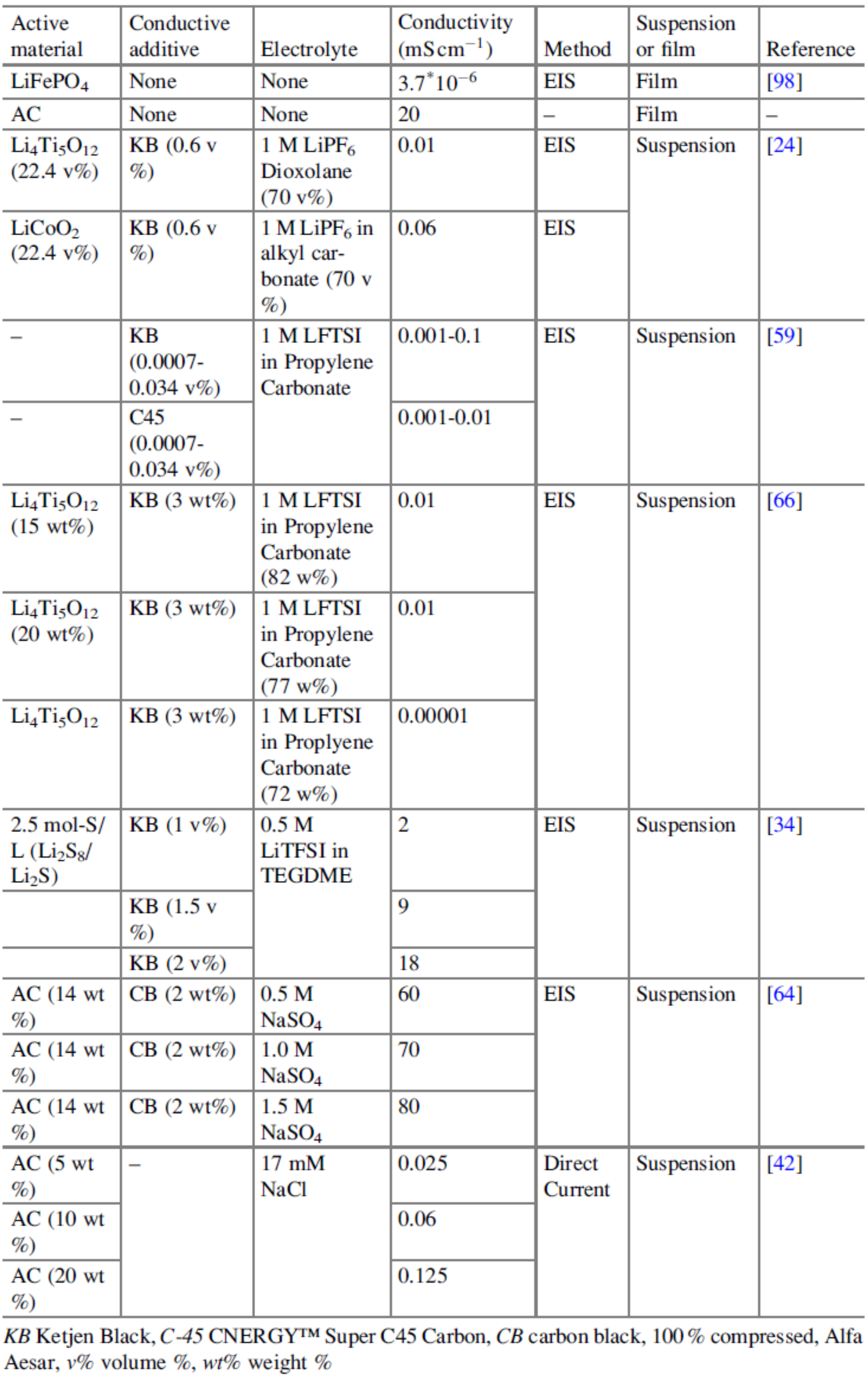

Active material	Conductive additive	Electrolyte	Conductivity (mS cm^{-1})	Method	Suspension or film	Reference
$LiFePO_4$	None	None	$3.7^{*}10^{-6}$	EIS	Film	[98]
AC	None	None	20	–	Film	–
$Li_4Ti_5O_{12}$ (22.4 v%)	KB (0.6 v%)	1 M $LiPF_6$ Dioxolane (70 v%)	0.01	EIS	Suspension	[24]
$LiCoO_2$ (22.4 v%)	KB (0.6 v%)	1 M $LiPF_6$ in alkyl carbonate (70 v%)	0.06	EIS		
–	KB (0.0007-0.034 v%)	1 M LFTSI in Propylene Carbonate	0.001-0.1	EIS	Suspension	[59]
–	C45 (0.0007-0.034 v%)		0.001-0.01			
$Li_4Ti_5O_{12}$ (15 wt%)	KB (3 wt%)	1 M LFTSI in Propylene Carbonate (82 w%)	0.01	EIS	Suspension	[66]
$Li_4Ti_5O_{12}$ (20 wt%)	KB (3 wt%)	1 M LFTSI in Propylene Carbonate (77 w%)	0.01			
$Li_4Ti_5O_{12}$	KB (3 wt%)	1 M LFTSI in Proplyene Carbonate (72 w%)	0.00001			
2.5 mol-S/L (Li_2S_8/Li_2S)	KB (1 v%)	0.5 M LiTFSI in TEGDME	2	EIS	Suspension	[34]
	KB (1.5 v%)		9			
	KB (2 v%)		18			
AC (14 wt%)	CB (2 wt%)	0.5 M $NaSO_4$	60	EIS	Suspension	[64]
AC (14 wt%)	CB (2 wt%)	1.0 M $NaSO_4$	70			
AC (14 wt%)	CB (2 wt%)	1.5 M $NaSO_4$	80			
AC (5 wt%)	–	17 mM NaCl	0.025	Direct Current	Suspension	[42]
AC (10 wt%)			0.06			
AC (20 wt%)			0.125			

KB Ketjen Black, *C-45* CNERGY™ Super C45 Carbon, *CB* carbon black, 100 % compressed, Alfa Aesar, *v%* volume %, *wt%* weight %

Appendix C – Nernst Equation Applied on the Fe- and Manganese Hydroxide System in 5M KOH Solution

By applying the Nernst equation (Eq. 4) on the two proposed half-cell energy potentials at standard conditions (Eqs. 11 and 12), while assuming SoC 100% and in a 5M KOH solution, the respective half-cell potentials in operational conditions become as follows:

$$E_{cat} = 0.15 - \frac{8.314 \text{ x } 293}{1 * 96500} \ln\left(\frac{\mathbf{1}^1 \text{ x } 5^1}{1^1}\right) = 0.11 \text{ V} \tag{30}$$

$$E_{an} = -0.56 - \frac{8.314 \text{ x } 293}{1 * 96500} \ln\left(\frac{\mathbf{1}^1}{1^1 \text{ x } 5^1}\right) = -0.52 \text{ V} \tag{31}$$

Then by respectively using equation Eq. 7, the cell potential in a 5M KOH environment becomes:

$$\mathrm{E_{cell}} = 0.11 - (-0.52) = 0.63 \text{ V} \tag{32}$$

Appendix D – Pourbaix Diagrams of Iron and Manganese in Water

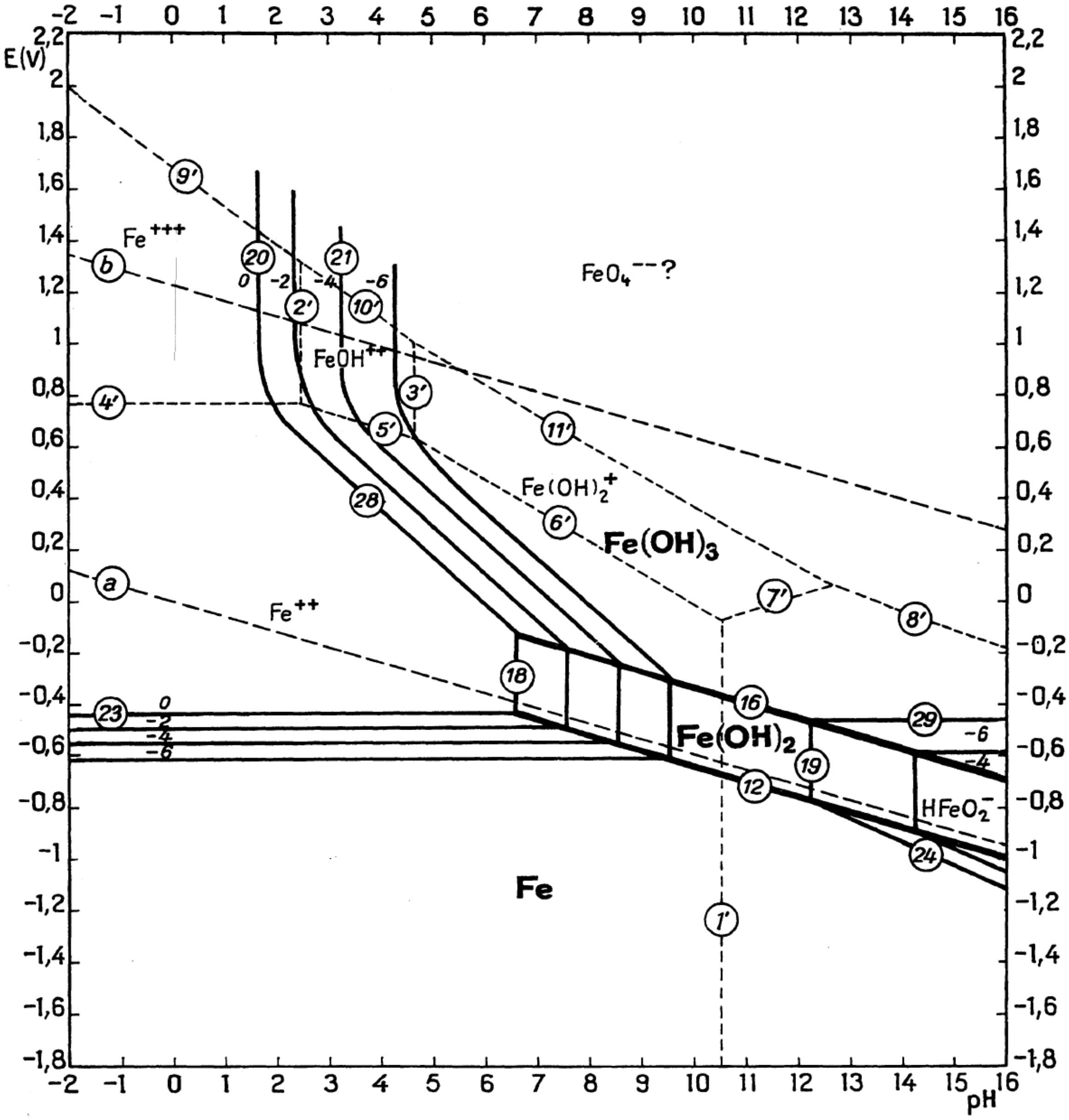

Figure 47: Potential-pH equilibrium diagram for the system iron-water, at 25°C (considering as solid substances only Fe, $Fe(OH)_2$ and $Fe(OH)_3$) (Pourbaix et al., 1997).

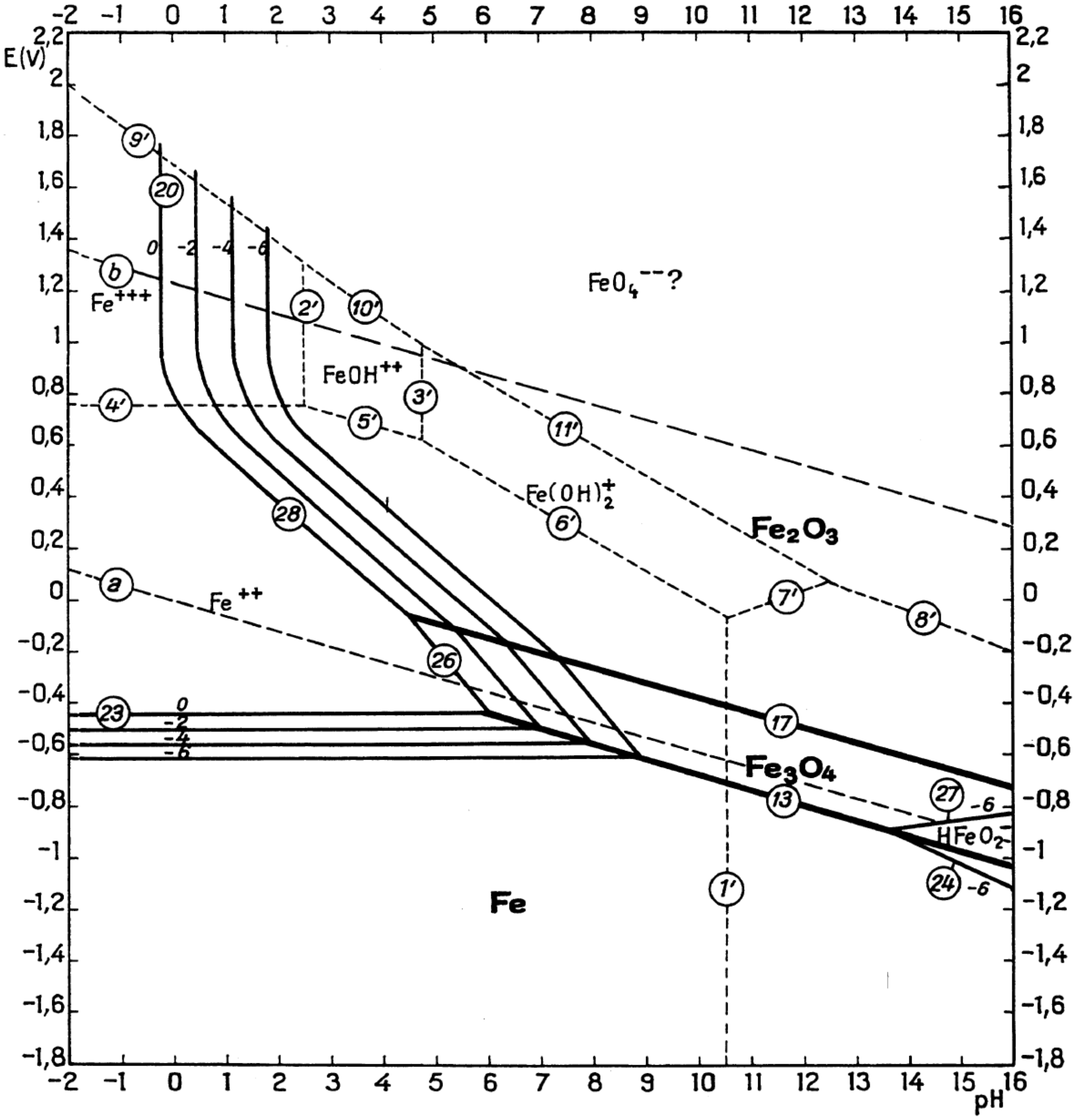

Figure 48: Potential-pH equilibrium diagram for the system iron-water, at 25°C (considering as solid substances only Fe, Fe_3O_4 and Fe_2O_3) (Pourbaix et al., 1997).

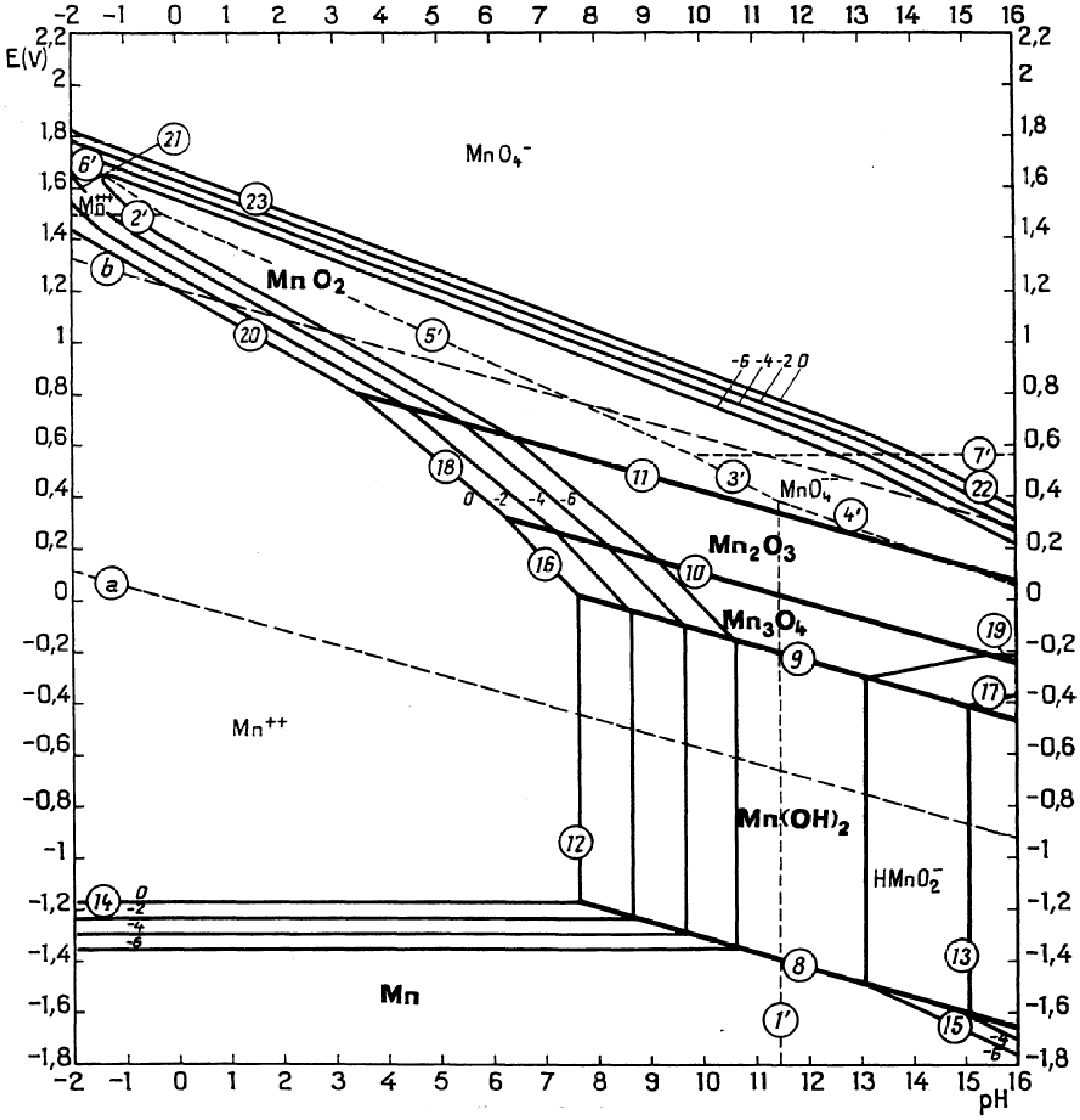

Figure 49: Potential-pH equilibrium diagram for the system iron-water, at 25°C (Pourbaix et al., 1997).

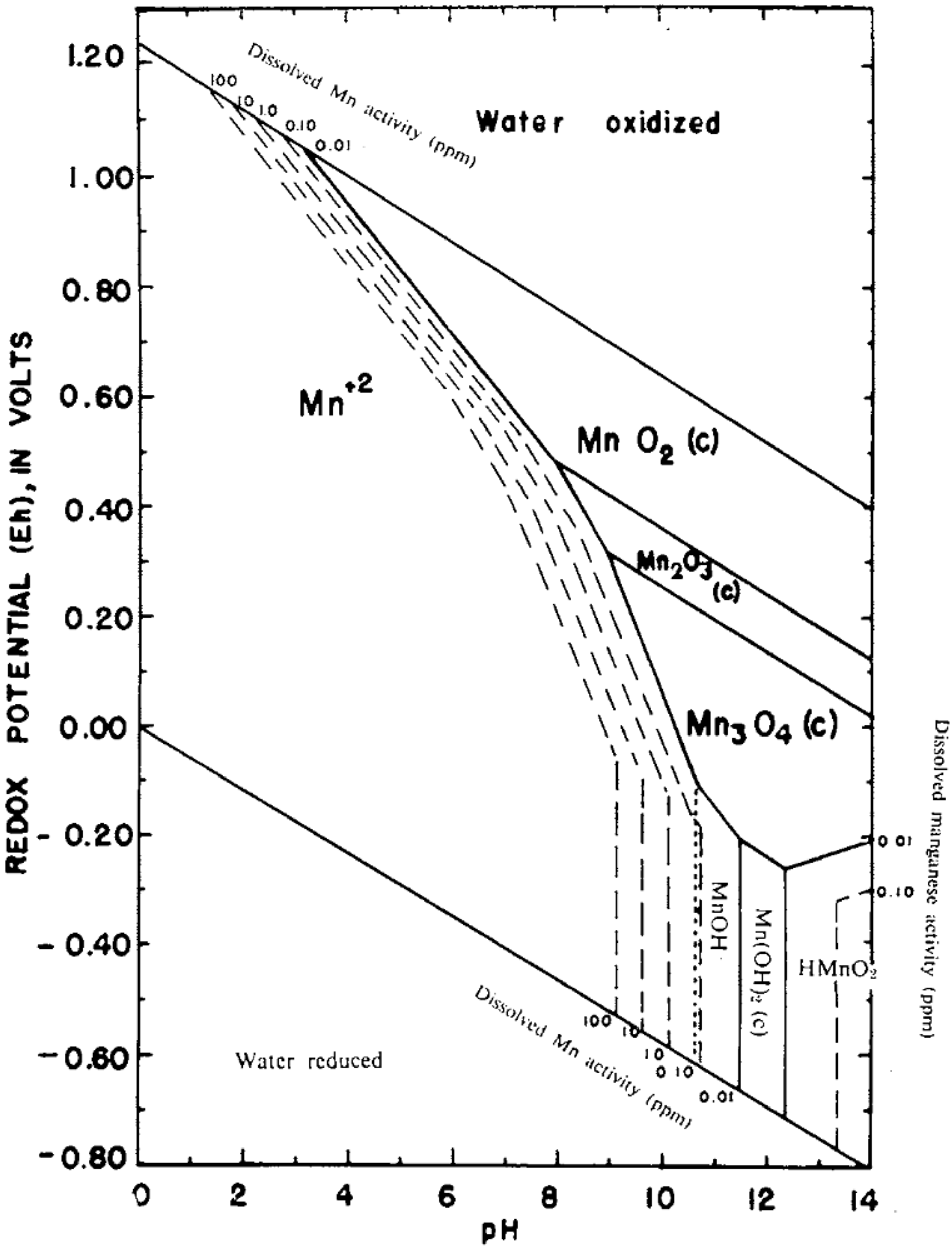

Figure 50: Potential-pH equilibrium diagram for the system manganese in natural water, at 25°C (Hem, 1963).

Appendix E – Preparation of and active material on FeOOH solid electrode

This Appendix reports the method for the preparation of a solid FeOOH electrode. The solid FeOOH electrodes were tested using a salt bridge in order to compare results with respect to the FeOOH SSE suspension. This procedure was not done for $Mn(OH)_2$ as dry $Mn(OH)_2$ would have been required in order to effectively use pvdf (pvdf hardens as soon as is makes contact with water). The solid electrodes holding FeOOH as active material were prepared in a similar method as is done for traditional Li-ion solid electrodes.

The recipe for the paste included a combination of Super C45 carbon black and KS4 graphite for electrical conductivity, both produced by Imerys. polyvinylidene fluoride (“pvdf”) acquired from Solvey was used as a binder and was dissolved in N-Methyl-2-pyrrolidone (“NMP”), acquired from Sigma Aldrich. Next to this, for the construction of the solid FeOOH electrodes, a 1 mm thin carbon paper substrate was used as current collector.

First, an electroactive and conductive slurry was created. This was done by making a 10 gram batch of powder containing 80 wt% FeOOH powder, 10 wt% pvdf, 7 wt% KS4 graphite and 3 wt% Super C45 carbon black. The powder mixture was then stirred for 10 minutes at 400 rpm using the Ultra Turrax mixer to homogeneously divide all the particles. Next, 14 grams of NMP was added to the mixture while stirring at 400 rpm. Pvdf is a binder that dissolves in NMP and the carbon black and graphite mixture enhance electronic conductivity. After addition of the NMP, the mixture becomes a honey-like slurry, which is stirred for one hour at 1000 rpm using the Ultra Turrax mixer. Next, a 10 cm by 15 cm piece of carbon paper is placed on a glass plate as a substrate on which a 150 µm layer of slurry is homogeneously deposited using a 150 µm doctor blade. The carbon paper substrate with the wet layer of slurry is then placed in an oven for half an hour at 120°C until the slurry has properly dried. After this, 3.5 cm by 1 cm samples were carved out using a scalpel, such that 2 cm contained the dried active material slurry and 1.5 cm was untouched carbon paper. The amount of active material on such a cell is 44 µmol (calculation at the end of this Appendix). Half of the samples were then pressed with a weight of 1 ton using the lab press and half of the samples remained unpressed. After addition of small sheets of zinc for rigidity, these samples now represent the solid FeOOH electrodes that were tested. using a salt bridge in order to compare results with respect to the FeOOH suspension electrode.

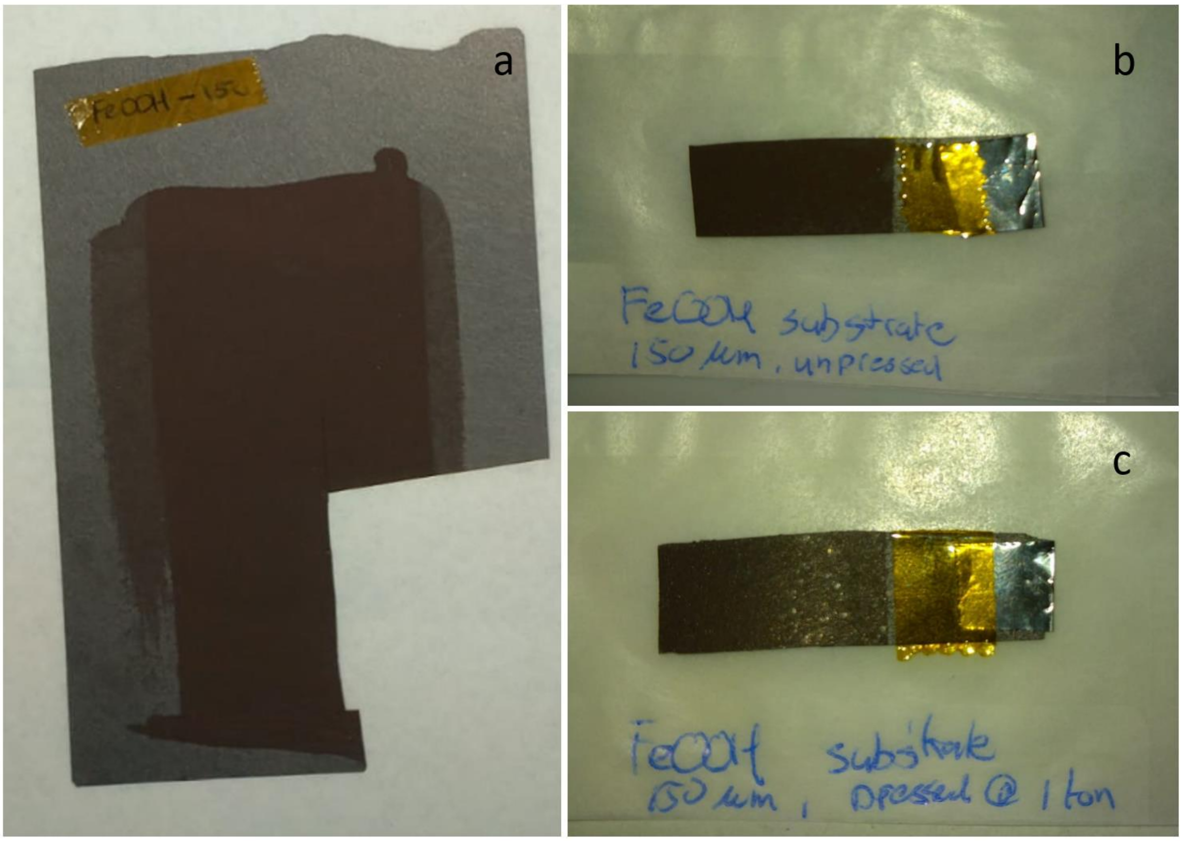

Figure 51: a) carbon paper substrate with 150 µm FeOOH slurry, b) unpressed FeOOH solid electrode and c) FeOOH solid electrode pressed at 1 ton.

Calculation of active material on cell

One electrode had a dimension of 3.5cm x 1cm, of which 2cm x 1cm was covered with active material slurry. The weight of an uncovered piece of 3.5cm x 1cm carbon paper was 0.03298 grams. The weight after coverage with the FeOOH slurry was 0.04479 grams. The weight of slurry on one solid electrode sample was thus 0.01181 grams.

The total slurry weight was 24 grams and the composition of the slurry was as follows:

- 14 grams NMP
- 8 grams FeOOH
- 1 gram pvdf
- 0.7 grams KS4 graphite
- 0.3 grams super C45 carbon black

From the above follows that 33.3 wt% of the slurry is FeOOH. Thus, the weight of FeOOH on one solid electrode sample is 0.00394 grams. This corresponds to 0.00004434 mol FeOOH, or respectively 44 µmol FeOOH.

Appendix F – Secondary experiments

Using these experiments the most important trends of design choices were found through short and often qualitative experiments. The purpose of this these was to provide a framework for the convergence phase in which more time-consuming measurements were used.

First, the effect of different type of emulsifiers on colloidal stability was tested by bringing 2 wt% KB into suspension with 5M KOH, while keeping a sample without emulsifier as reference. Initially ALG and PVP were tested and at a later stage additionally PAA was tested. The samples were examined on the colloidal stability both directly after as well as 36 hours after the preparation.

Second, different wt% KB were added to a solution of demi water and 2 wt% ALG to find the percolation threshold of KB in water as well as to investigate the effect of addition of KB on the colloidal stability and viscosity. This was done from 0 wt% to 9 wt% KB with 1 wt% increments. It was done in demi-water, so that the conductivity meter could be used for fast measurements regarding electric conductivity of the suspension, as > 1M KOH solution the conductivity meter went out of bounds based on the ionic conductivity of KOH (Gilliam et al., 2007) and the parallel configuration of KB and ionic conductivity.

Third, the same experiment was repeated, except that the KB was now kept constant at 8 wt% and ALG was varied from 0 wt% to 2.5 wt% with 0.5 wt% increments. During the Ultra Turrax mixing a close eye was held on the viscosity of the samples. After these measurements were done, they were examined with respect to their colloidal stability.

Fourth, as an indicator for conductivity the membranes were tested on their porosity by using setup 3 in Chapter 3.6.3 and filling one side of the elbow with copper nitrate which turned blue, Cu^{2+} is blue from colour, and one side with demi- water. The sides were separated by a membrane. The side with copper nitrate was filled slightly higher after which was investigated whether any Cu^{2+} ions passed through the membrane, which would be indicated by the demi-water turning blue on the side that was initially without Cu^{2+} ions.

Fifth, the porosity and hydrophobicity of the membranes was investigated with respect to KB in 5 M KOH solution to investigate the significance of cross-over. For this experiment a drop of KB in 5M KOH solution was deposited on a membrane on a beaker which was also filled with 5M KOH solution. The shape of the drop was investigated in order to comment on hydrophobicity and with respect to porosity this was then rested then rested for 36 hours and afterwards examined on cross-over of kb.

Appendix G – Ionic resistance at high frequencies and extremely high electric resistance

Below the proof is shown that if the electronic resistance in a SSE suspension becomes extremely high, it may be assumed that the high frequency intercept of the Z_{real} intersection is equal to the ionic resistance.

Rewrite Eq. 13 as:

$$R_{ion} = -\frac{R_{0-high}R_{kb}}{R_{0-high} - R_{kb}} \tag{33}$$

Multiply the right side by $1/R_{kb}$ in both the numerator and the denominator to retrieve:

$$R_{ion} = -\frac{R_{0-high}}{\frac{R_{0-high}}{R_{kb}} - 1} \tag{34}$$

Fill in the limit for R_{kb} towards infinity:

$$\lim_{R_{kb}\to\infty} R_{ion} = -\frac{R_{0-high}}{\frac{R_{0-high}}{\infty} - 1} \rightarrow R_{ion} = R_{0-high} \tag{35}$$

Appendix H – Membrane analysis additional results

It was observed that all membranes were porous with respect to Cu^{2+} ions. Whatman paper showed highest porosity, then filter paper followed by Cellgard, which only showed minimal ion cross-over after waiting 10 minutes. This is indicated by the cross-over of the blue colour from the right into the left compartment (Figure 52).

Figure 52: Ionic porosity of: (left) filter paper, (middle) Whatman and (right) Cellgard membrane (wetted by ethanol).

With respect to solid material cross-over, Figure 53 shows how glass cups were filled untill the edge with 5M KOH solution on which the respective membranes were deposited which were all properly wetted. Next, a couple droplets of a 5/1.5-ALG/-/93.5-5M suspension were deposited on the membranes. On the hydrophobic Cellgard membrane an additional droplet of ethanol was added to reduce surface tension so that the porosity of the membrane could be adequately tested. After the first hour none of the samples showed visible evidence that KB was going through the pores of the membranes. After leaving this setup for 36 hours in an air sealed environment, still no visible evidence was found for crossover of the KB (Figure 53).

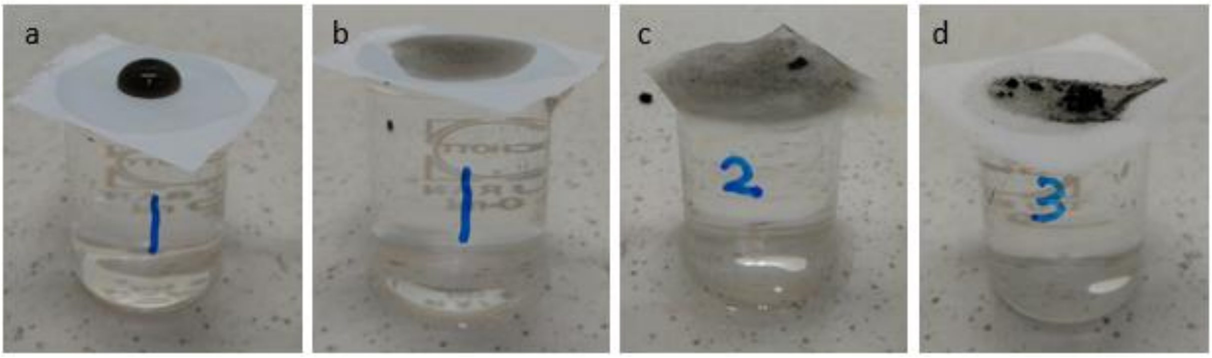

Figure 53: Porosity test setup of membranes using the 5 wt% KB / 1.5 wt% Alginate suspension sample. a) Hydrophobic Cellgard 2400 membrane, b) Cellgard 2400 after addition of a droplet of ethanol, c) filter paper membrane and d) Whatman GFA membrane.

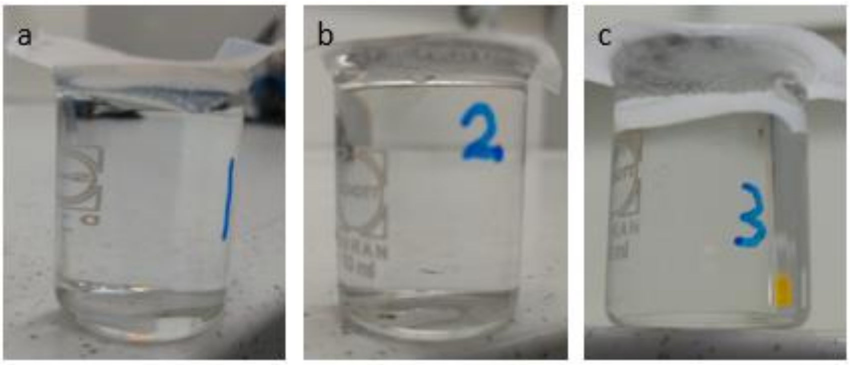

Figure 54: Porosity test result of membranes after 36 hours exposure to the 5 wt% KB / 1.5 wt% Alginate suspension sample. a) Hydrophobic Cellgard 2400 membrane, b) filter paper membrane and c) Whatman GFA membrane.

Appendix I – Additional EIS results

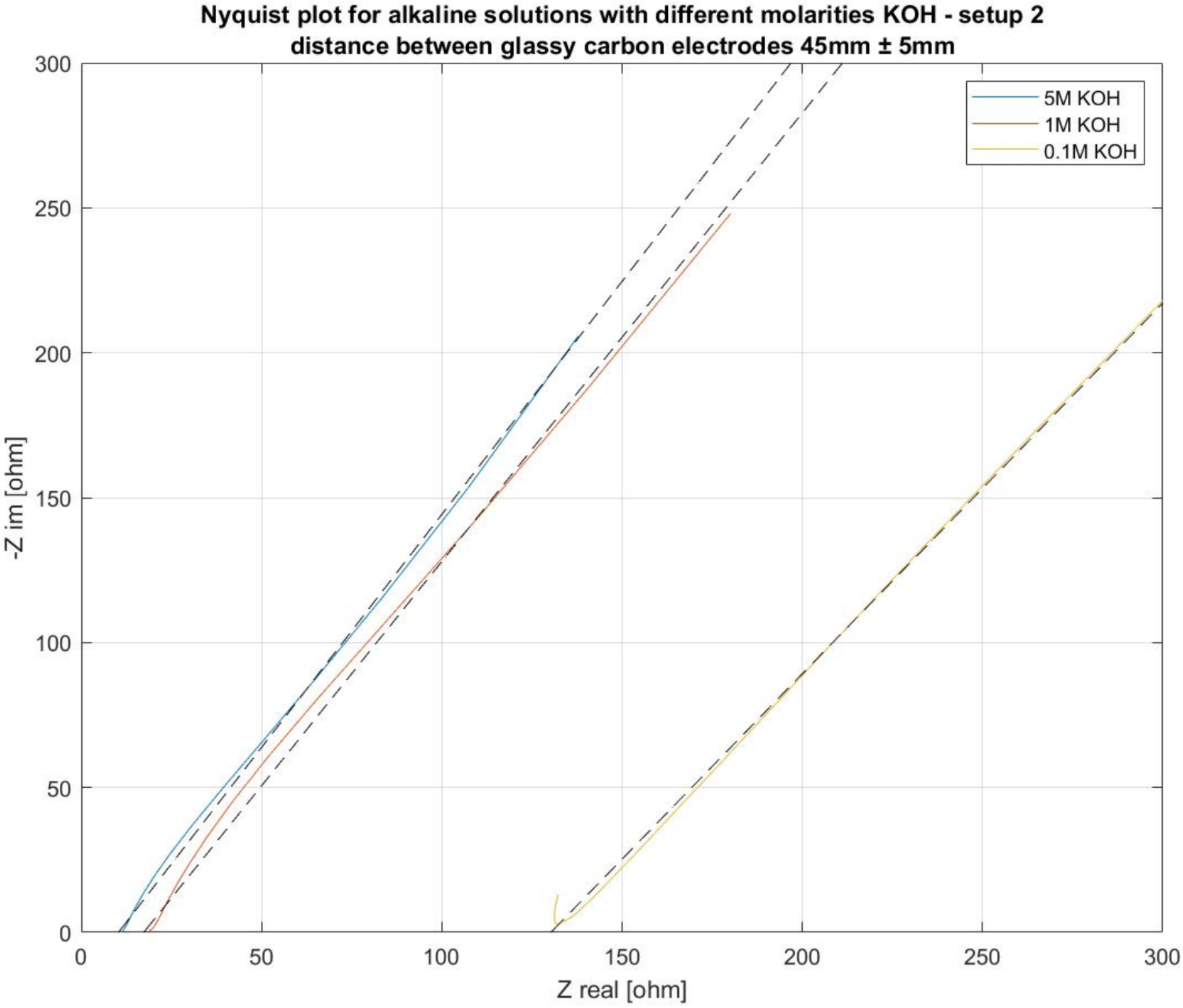

Figure 55: EIS results for a pure 5M, 1M and 0.1M KOH solution in experimental setup 2.

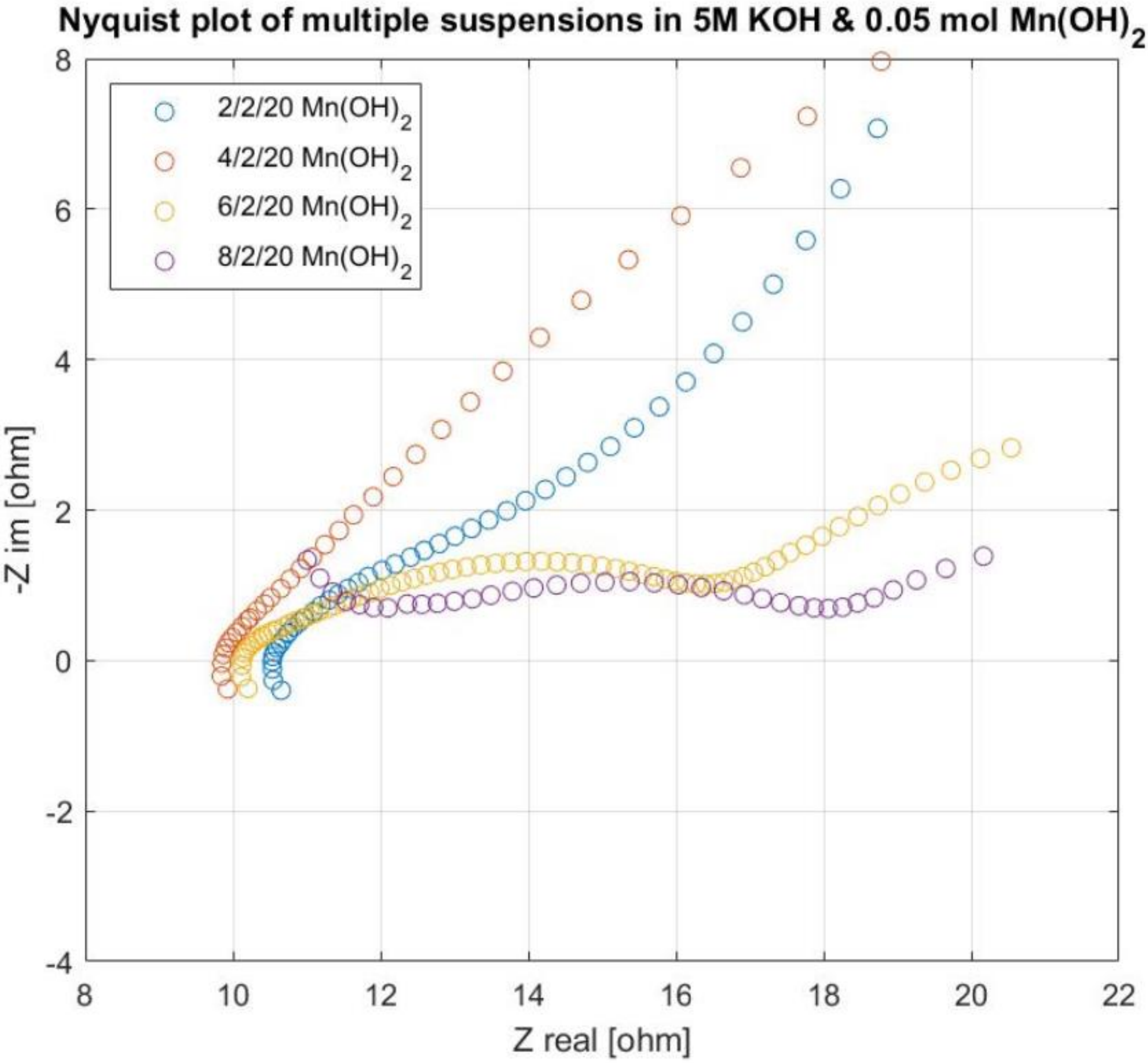

Figure 56: EIS results for the suspensions: 2/2-ALG/22.2-Mn/73.8-5M, 4/2-ALG/22.2-Mn/71.8-5M, 6/2-ALG/22.2-Mn/69.8-5M and 2/2-ALG/22.2-Mn/67.8-5M – executed in experimental setup 2.

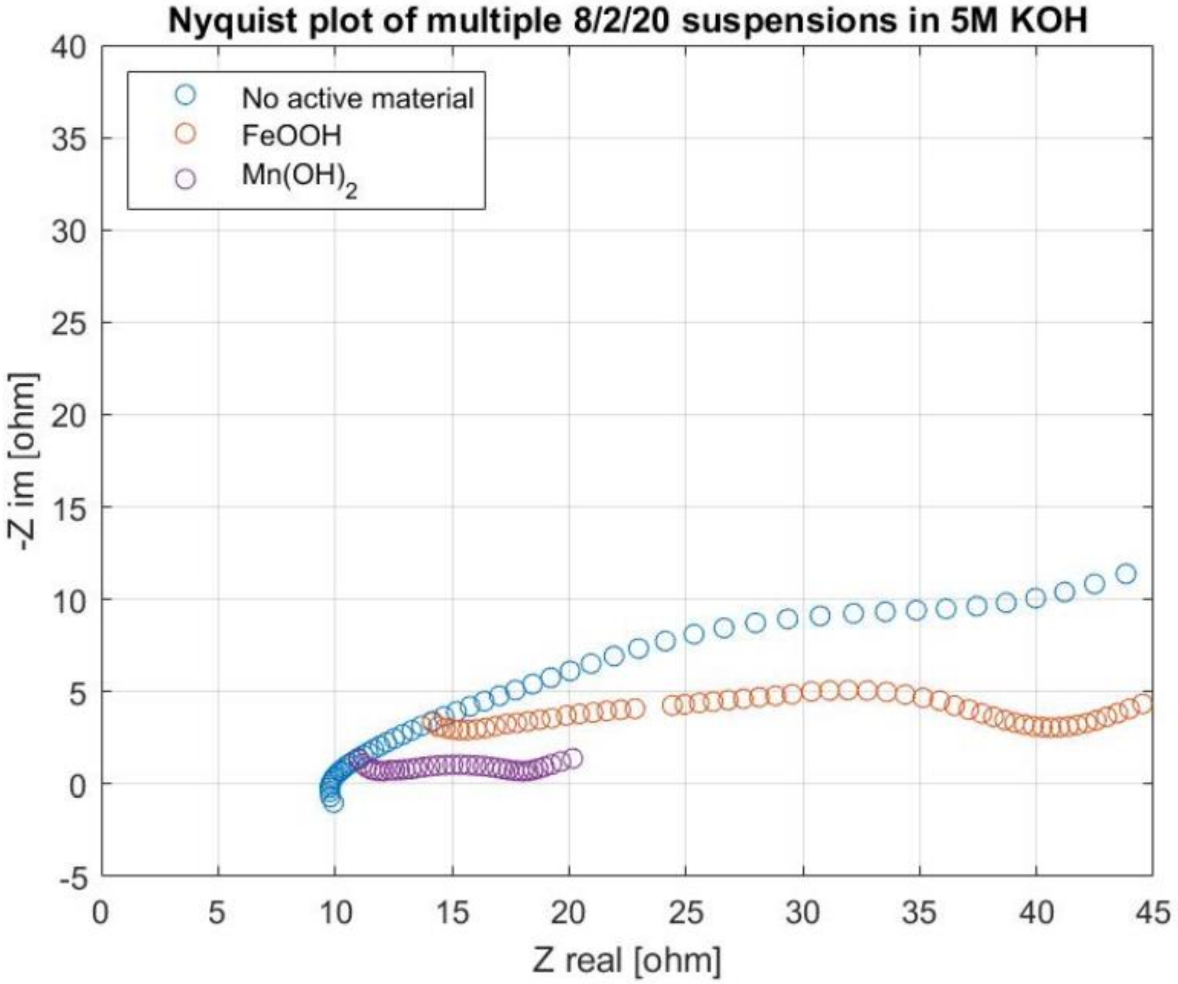

Figure 57: EIS results for the suspensions: 8/2-ALG/-/90-5M, 8/2-ALG/22.2-Fe/67.8-5M and 8/2-ALG/22.2-Mn/67.8-5M – executed in experimental setup 2.

Appendix J – Additional results of cycling procedures

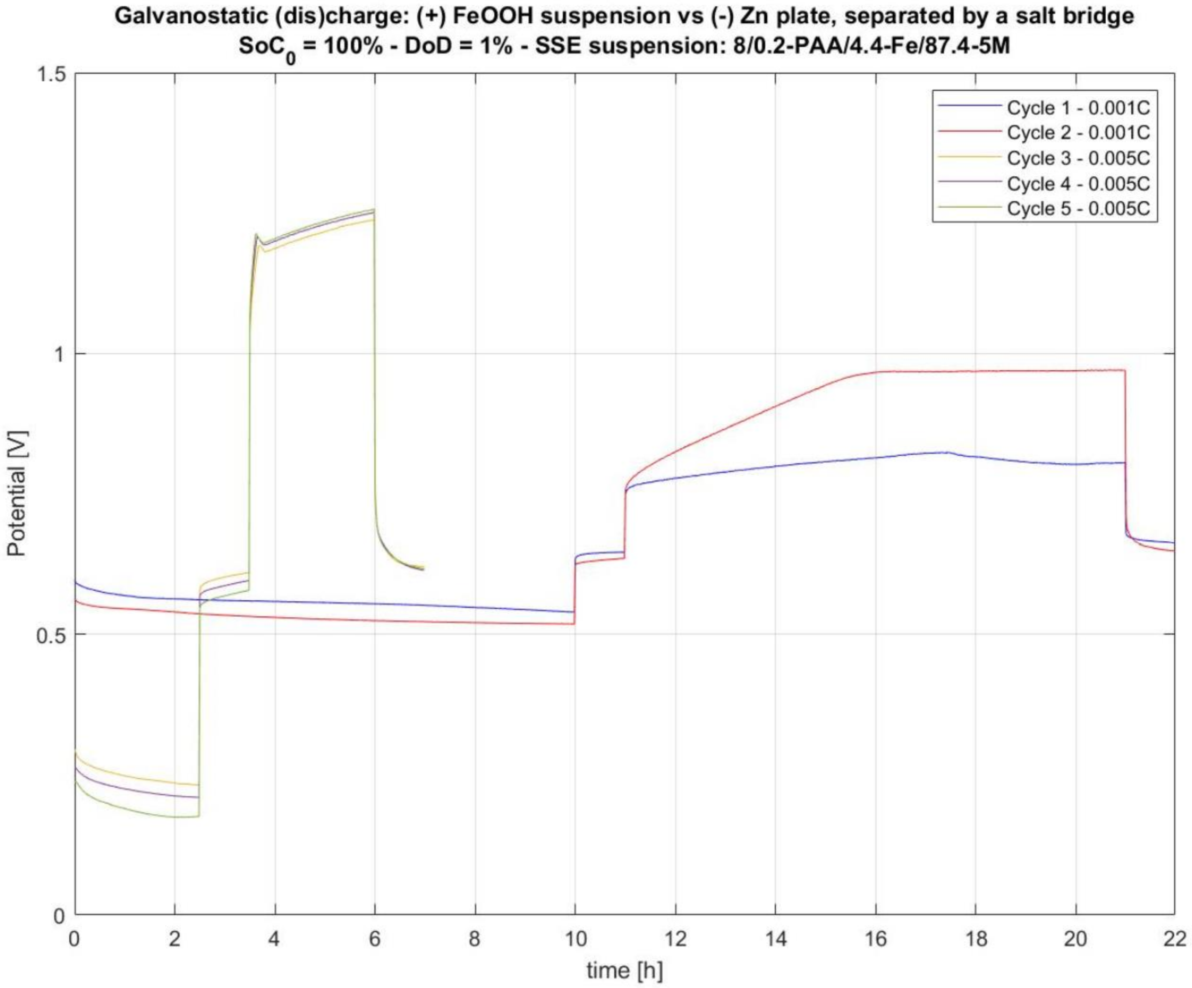

Figure 58: Short cycling of the 8/0.2-PAA/4.4-Fe/87.4-5M SSE suspension, using the system with salt bridge setup. Average cycling efficiency at C-rate of 5 mC = 62.9% and at 20 mC = 18.2%.

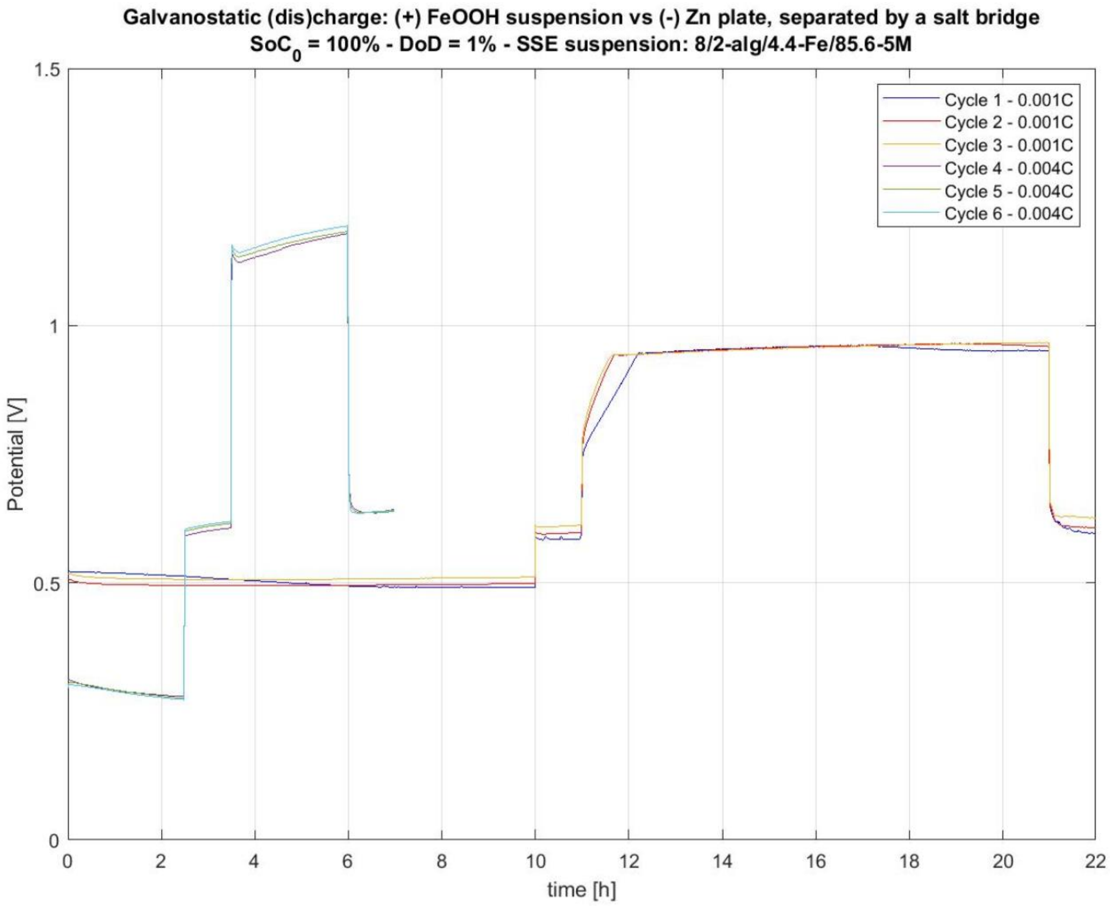

Figure 59: Short cycling of the 8/2-ALG/4.4-Fe/85.6-5M SSE suspension, using the system with salt bridge setup. Average cycling efficiency at C-rate of 1 mC = 53.0% and at 4mC = 24.9%.

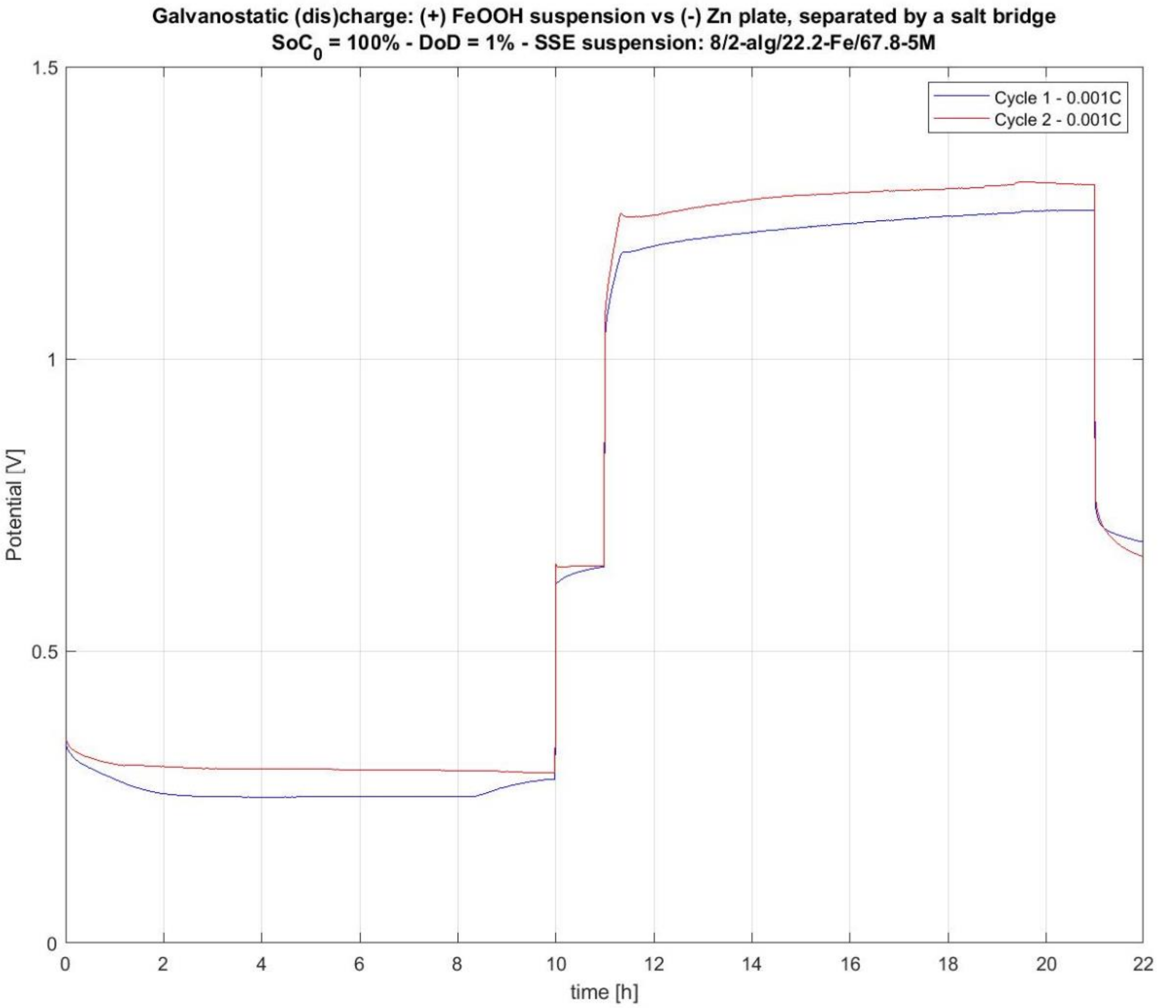

Figure 60: Short cycling of the 8/2-ALG/22.2-Fe/67.8-5M SSE suspension, using the system with salt bridge setup. Average cycling efficiency at C-rate of 1 mC = 22.4%.

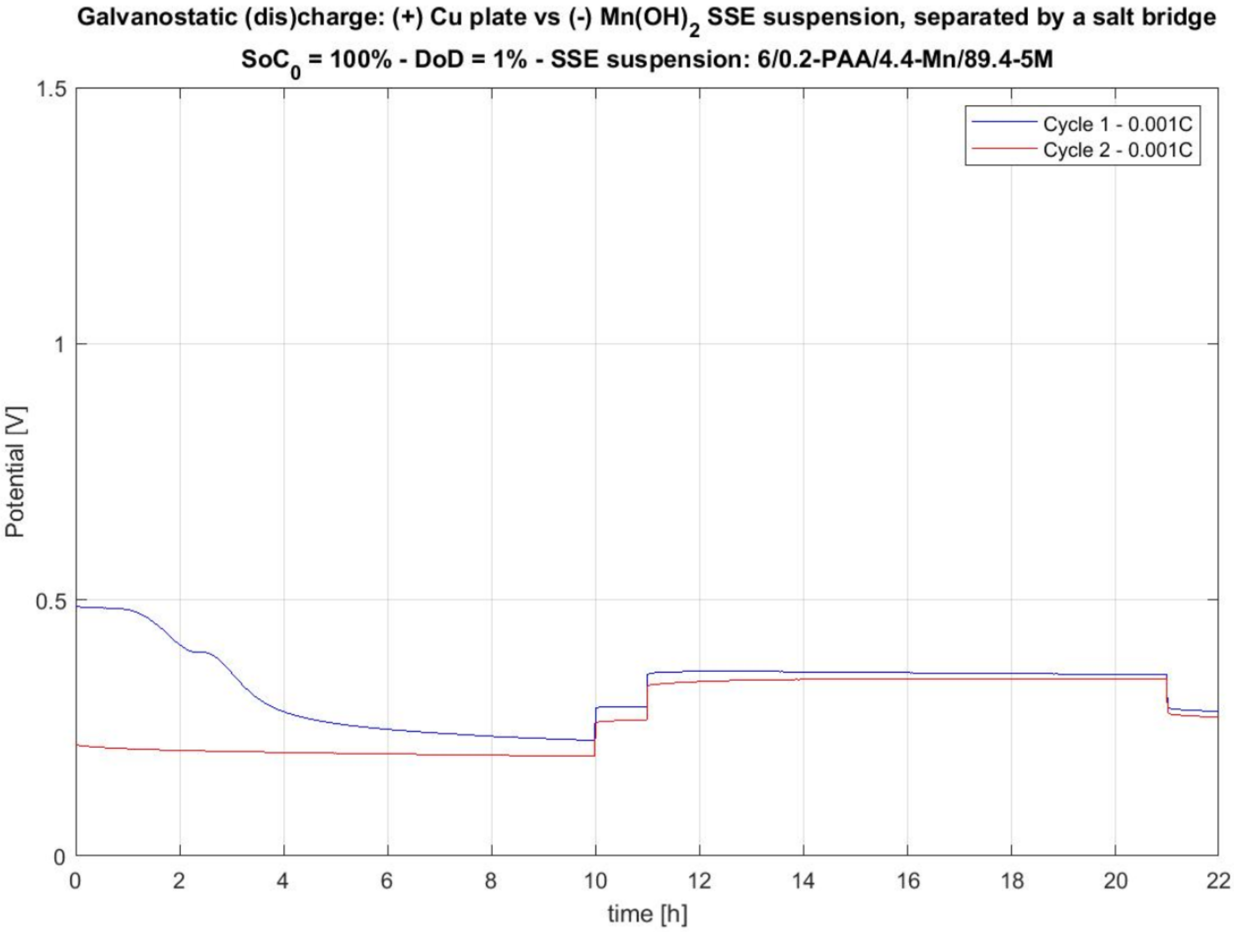

Figure 61: Short cycling of the 6/0.2-PAA/4.4-Mn/89.4-5M SSE suspension, using the system with salt bridge setup. Average cycling efficiency at C-rate of 1 mC = 73.0%.

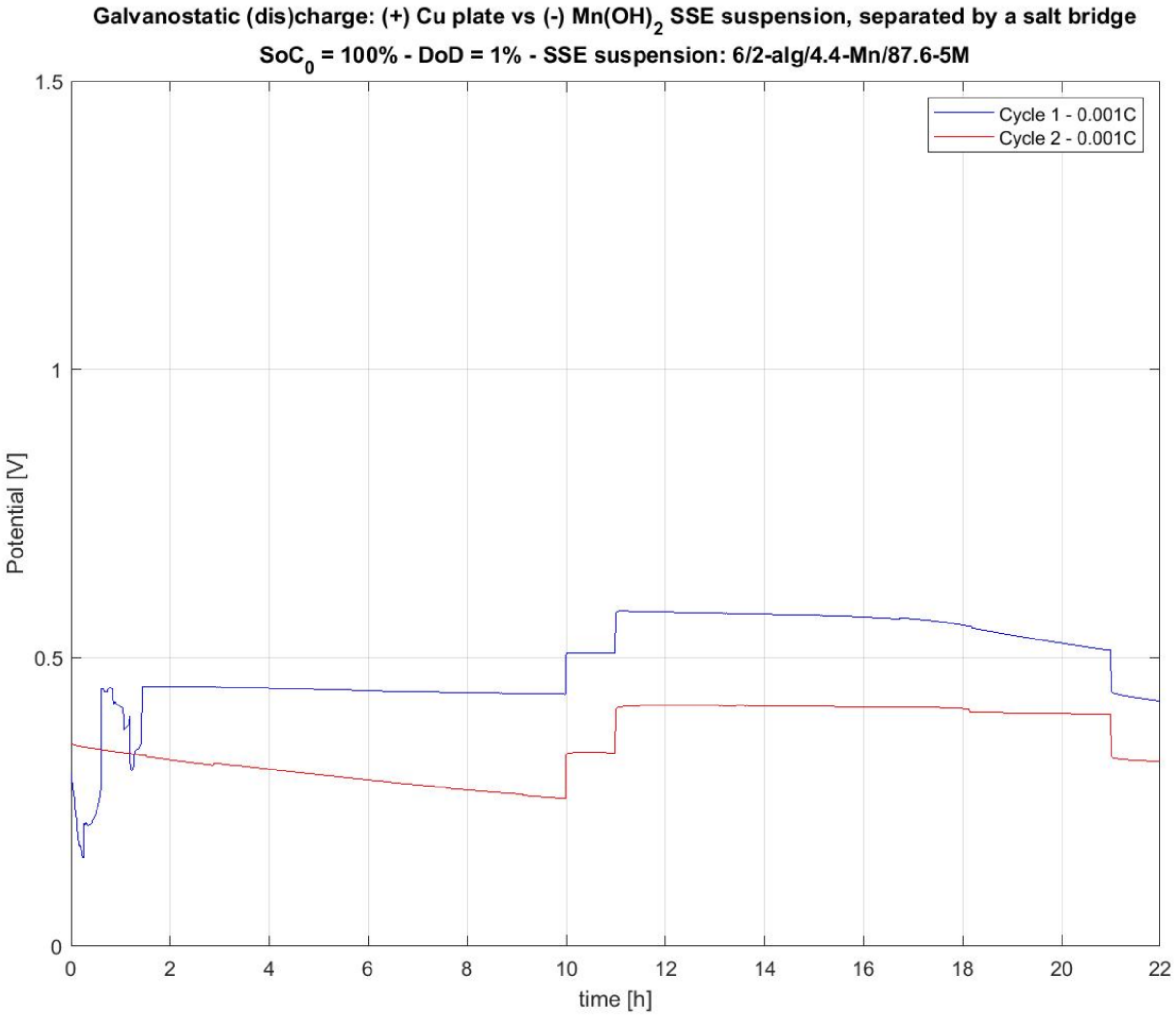

Figure 62: Short cycling of the 6/2-ALG/4.4-Mn/87.6-5M SSE suspension, using the system with salt bridge setup. Average cycling efficiency at C-rate of 1 mC = 74.4%.